STATE OF OREGON
DEPARTMENT OF GEOLOGY AND MINERAL INDUSTRIES
Suite 965, 800 NE Oregon St., #28
Portland, Oregon 97232

OPEN-FILE REPORT O-97-34

CASCADIA SUBDUCTION ZONE TSUNAMIS: HAZARD MAPPING AT YAQUINA BAY, OREGON

FINAL TECHNICAL REPORT TO THE NATIONAL EARTHQUAKE HAZARD REDUCTION PROGRAM

by

George R. Priest
Oregon Department of Geology and Mineral Industries

Edward Myers and António M. Baptista
Oregon Graduate Institute of Science & Technology

Paul Fleuck and Kelin Wang
Geological Survey of Canada

Robert A. Kamphaus
Pacific Marine Environmental Laboratory,
National Oceanic and Atmospheric Administration

Curt D. Peterson
Portland State University

December 1997

NOTICE

The Oregon Department of Geology and Mineral Industries is publishing this paper because the information furthers the mission of the Department. To facilitate timely distribution of the information, this report is published as received by the authors and has not been edited to our usual standards.

CONTENTS

FIGURES

TABLE

CASCADIA SUBDUCTION ZONE TSUNAMIS: HAZARD MAPPING AT YAQUINA BAY, OREGON

NON-TECHNICAL ABSTRACT

Potential tsunami flooding from Cascadia subduction zone earthquakes at Yaquina Bay in Newport, Oregon was explored by simulating fault ruptures and resulting tsunamis. Flooding from most scenario tsunamis is modest, because of protection by large jetties and sand dunes. However, a worst case tsunami reaches elevations of 35 feet at the open coast and floods all lowlands 1.5 miles inland. Flooding from scenario tsunamis reaching elevations of 12 and 27 feet at the open coast was also mapped to illustrate the range of uncertainty in the mapping technique. Current velocities in the main shipping channel were up to 16 knots.

EXECUTIVE SUMMARY

Sea floor deformation from great (M8-9) earthquakes on the Cascadia subduction zone will cause tsunamis to strike the North American coast. Numerical simulations were used to explore possible tsunami hazard scenarios for subduction zone earthquakes. Fully three dimensional fault rupture models simulate vertical sea floor deformation during a subduction zone earthquake. Two-dimensional finite element (unstructured grid) hydrodynamic simulations propagate tsunamis utilizing the modeled vertical sea floor deformation as an initial condition.

Segmented ruptures 450 km in length with 7-10 m slip are most consistent with coupling and aspect (length:width) ratios of world wide analogues to Cascadia. Coseismic ruptures with slip on the order of 15-20 m, and wide (140 km) rupture widths extending well onshore in Oregon provide a best fit to paleoseismic data. Paleoseismic data are also permissive of maximum rupture lengths on the order of 1,050. Narrower ruptures (70-80 km) that occur mostly offshore provide a best fit to thermal and geodetic data.

Other factors such as submarine landslides, local faults, and asperities can also amplify tsunamis. Asperity effects were simulated utilizing a 4.5 m Gaussian uplift, added to 1.5 m of uplift on a 1,050 km-long narrow (70-80 km) rupture. This roughly simulates a doubling of the uplift associated with 15-20 m of slip on a fault dipping 10°, the approximate dip of the megathrust. The other amplifying factors were not simulated.

Onshore geodetic and paleoseismic data do not sufficiently constrain coseismic deformation offshore to predict coseismic or interseismic bottom deformation in accretionary wedge sediments of the seaward transition zone (STZ) updip of the locked zone (LZ). Three STZ cases were simulated: Scenario A, coseismic slip in STZ essentially equals slip in the LZ; Scenario B, coseismic slip in STZ linearly decreases from the LZ to the deformation front; and Scenario C, essentially no coseismic slip occurs in the

STZ. The STZ models do not simulate inelastic deformation or deformation from local faults. Inelastic deformation near the deformation front will tend to decrease coseismic uplift relative to the models, because the elastic models produce "spikes" of uplift near the seaward ends of the buried ruptures that would not necessarily be present in inelastic deformation. These "spikes" caused the total submarine uplift to be similar for Scenarios A, B, and C, producing, similar tsunamis, other factors being equal.

Open coastal run-up increased with increased total slip, and, for a given total slip, narrower ruptures produced higher tsunamis at the open coast than wider ruptures. The asperity simulation produced a 40 percent larger open coastal run-up and dramatically larger inundation compared to the largest tsunami generated without the asperity (tsunami from the narrow (70-80 km) 1,050 km rupture). The dramatic increase in inundation was caused by the large volume of water and by breaching of all jetties and foredunes.

Owing to the extensive coastal barriers and relatively high topographic relief at Yaquina Bay, only three inundation scenarios were depicted on the final tsunami hazard map: High Run-up (1,050 km long, 70-80 km wide rupture with 15-20 m of slip plus a 4.5 m Gaussian asperity), Moderately High Run-up (same rupture without the asperity), and Moderately Low Run-up (450 km long, 140 km wide rupture with 7-10 m of slip). Corresponding open coastal run-up elevations are approximately 11 m, 8 m, and 4 m, assuming a mean higher high water tide and including the coseismic subsidence. In areas like Seaside, Oregon that have lower relief and no protection from jetties or high foredunes additional planning scenarios can be valuable. In these areas a third Cascadia scenario termed "Moderate Run-up" can be mapped that utilizes the wide (140 km rupture) 1,050-km-long rupture with about 15-20 m of slip. A fourth scenario representing a worst case teletsunami can be approximated by mapping the inundation from the 1964 Alaska tsunami. Had these two scenarios been mapped at Yaquina Bay, the inundation lines would have been difficult to distinguish among the other three scenarios.

INTRODUCTION

Scientific findings of the last several years have shown that the Oregon coast is vulnerable to great (M 8-9) earthquakes that can occur on the offshore Cascadia subduction zone fault system (Figure 1; see Madin, 1992, Atwater and others, 1995, and Nelson and others, 1995, for summaries). Such earthquakes can generate tsunamis that will be very dangerous to populated areas of the Pacific Northwest coast. This study explores possible tsunami hazard scenarios for these great earthquakes as they pertain to a tsunami hazard map of the Yaquina Bay area of Newport, Oregon (Figure 1). Available data on the geometry of the Cascadia subduction zone and paleoseismic history of earthquakes and tsunamis is used to constrain possible scenarios. These scenarios will be used for a similar study of tsunami hazards at Seaside and Gearhart on the northern Oregon coast.

The impetus for the study is the need for the Oregon Department of Geology and Mineral Industries (DOGAMI) to produce tsunami inundation maps for the Oregon coast.

Various map products are primarily used by evacuation planners. Building codes officials in charge of implementation of Oregon Senate Bill 379 (SB 379) also make use of the maps, if a scenario inundation limit is adopted by governmental action. SB 379 limits construction of certain critical and essential facilities in potential tsunami inundation zones. Oregon Department of Geology and Mineral Industries maps IMS–2 and IMS-3 illustrate the expected inundation at Newport and Seaside, respectively (Priest and others, 1997; Priest and others, in preparation).

PREVIOUS WORK

Whitmore (1993; 1994) produced estimates of expected tsunami amplitudes from a M_w 8.8 earthquake extending 650 km along the Cascadia subduction zone. This fault rupture model was based on a segment rupture postulated by Weaver and Shedlock (1989) to extend from southern Washington to northern California (41.5° N lat.).

Priest (1995), in cooperative work with Oregon Graduate Institute of Science and Technology, utilized this same rupture length to explore tsunami hazard scenarios for use in production of inundation maps for implementation of SB 379. He tried to make the scenarios consistent with prehistoric coseismic deformation at estuarine marsh sites, the dip of the subduction zone, as imaged by seismic reflection and refraction data, and the thermal regime. Fault dislocation modeling was based on either (1) a three-dimensional (3-D) dislocation model derived from Okada (1985) that simulates vertical deformation of rectangular fault planes after coseismic slip on fully locked faults, or (2) linear extrapolation of 2-D profiles of coseismic deformation derived by reversing interseismic uplift and subsidence rates of Hyndman and Wang (1993).

Priest (1995) found that when 2-D and 3-D models were constrained by the same paleoseismic estimates of coseismic subsidence, the 2-D model produced tsunami run-up large enough to explain known paleotsunami deposits, whereas the 3-D model produced tsunamis that were too small. The reason the 2-D method produced higher run-up was its ability to simulate partial locking on the subduction zone. Partial locking in the landward transition from stick slip to stable sliding behavior (Figure 2) spreads the vertical deformation over a larger area, effectively lowering the subsidence for a given amount of slip. Incorporating the transition zone demanded larger slips (and associated sea floor uplift) to produce the maximum of 1.5-2 m subsidence demanded by the paleoseismic data.

This paper summarizes the results of simulating tsunami inundation at Newport, Oregon from coseismic deformation on the Cascadia subduction zone. The coseismic deformation is simulated by software developed by Fleuck and others (in press) that allows fully three dimensional (3-D) simulation of locked and partially locked zones. The fault rupture models are used to excite tsunamis simulated with finite element software developed by the Oregon Graduate Institute of Science and Technology (see Appendix A).

ANALYTICAL METHOD

Fault Dislocation Model

The fault dislocation model used here is the method of Fleuck and others (in press). They developed a 3-D fault rupture model based on point source solutions of the Okada (1985) equations for surface deformation and strain due to shear faults in an elastic half space. Details of the model and its use are summarized in Appendix C.

Paleoseismic Data

Paleoseismic estimates of coastal coseismic deformation, especially subsidence, are useful checks on fault rupture models. Evidence for episodic subsidence has been found in estuarine marshes throughout the Cascadia margin (e.g. see Atwater and others, 1995). This data is summarized in Appendix C and in Peterson and others (1997). The data are consistent with Cascadia subduction zone earthquakes that produce a trough of coseismic subsidence on the order of 2 m depth inland from the Oregon coast. This inland subsidence is in turn consistent with ruptures on the order of 140 km or more width that penetrate well inland of the Oregon coast.

Fault Parameters

The fault rupture slip, width, and length on potential Cascadia subduction zone ruptures are an active source of scientific debate and inquiry. This investigation treats only a few highly simplified cases to illustrate some of the possibilities.

Figure 2 illustrates the various zones of slip on the subduction zone. Coseismic ruptures will penetrate through the locked and landward transition zones, but may or may not cut entirely through the water saturated sediment and sedimentary rocks of the seaward transition.

Cascadia subduction zone megathrust is assumed to lie at the top of the subducted oceanic slab. The strike and dip of the slab was taken from Fleuck and others (in press), which is a slight modification of the model of Hyndman and Wang (1995). Near the deformation front the megathrust is assumed to propagate on a smooth curve from the top of the slab through overlying sediments to the sea floor (Figures C9 and C10, Appendix C).

Two rupture lengths will be explored. A maximum rupture length on the order of 1000 km has been postulated (e.g. Nelson and others, 1995; Atwater, 1996; Satake and others, 1996). This rupture will be assumed to extend 1,050 km from the Nootka Fault to the Mendocino Fault (Figure 1). A most probable rupture length of 450 km is supported by studies of aspect ratios of subduction zone ruptures analogous to Cascadia (Geomatrix, Consultants, 1995). Ruptures extending 450 km north and south of a midpoint at 44.8° N latitude (north central Oregon) were utilized to explore the 450 km scenario; only the

southern rupture was of interest for the present study, since it is offshore of the Newport, Oregon (see Figure C25). There is some paleoseismiic evidence (Darienzo and Peterson, 1995) that a segmented rupture may have terminated in this general part of the coast about 800 years ago. This is also the same general region where Goldfinger (1994), based on the narrow potential locked width of the subduction zone, has postulated that ruptures may terminate.

Two rupture widths were simulated. Geodetic and thermal data of Hyndman and Wang (1995) and Fleuck and others (in press) are consistent with a relatively narrow rupture width in Oregon and northern California (Appendix C, Figures C11 and C12). Priest (1995) found in multiple trials utilizing the rectangular dislocation model of Okada and interseismic deformation profiles of Hyndman and Wang (1993), that coastal paleosubsidence data matched a locked zone on the order of 70 km and a landward transition zone of about the same magnitude in Oregon. This case was explored by adopting the rupture width postulated by Fleuck and others (in press) for Washington and British Columbia, but utilizing the wider 70 + 70 km scenario to the south (Appendix C, Figure C13).

Fault slip may theoretically be calculated by multiplying the convergence rate times the recurrence interval times the coupling ratio (ratio of seismic slip to total interseismic convergence) and subtracting any lateral component of convergence taken up by lateral faults. Slip is assumed to be a maximum of 15-20 m for a worst case earthquake. Arguments based on comparisons of world wide aspect ratios and aseismic slip on subduction zone ruptures are consistent with slips of about half this amount. A complete discussion is given in Appendix C.

Three different slip distributions were explored for the seaward transition zone (STZ) of Figure 2, but, following the method of Hyndman and Wang (1993; 1995) only a linear decrease in slip will be assumed across the landward transition zone (LTZ). This leads to three different scenarios (Figure 3). Scenario A assumes that the STZ rides passively on the subducting plate until the locked portion of the fault "pushes from behind" during coseismic failure, propagating a rupture nearly completely through the STZ (Figure 4). Scenario B assumes that the coseismic rupture will have decreasing displacement linearly across the STZ (Figures 3 and 4). Scenario C assumes little penetration of the STZ by the coseismic rupture (Figures 3 and 4). Appendix C summarizes the possible fault dislocation models derived from the various combinations of total slip and slip distribution for subduction zone slip without complications from asperities

Appendix B explains how a worst case earthquake source is developed based on the assumption that an asperity could increase coseismic deformation immediately offshore from Yaquina Bay. This scenario asperity chosen is assumed to be analogous to the doubling of average slip in asperities approximately 100 km wide and 150 km long inferred for the 1960 Chilean (Barrientos and Ward, 1990) and 1946 Nankai earthquakes (Yabuki and Matsu'ura, 1992). A Gaussian uplift was added to the fault dislocation model with a 1,050 km rupture and relatively narrow (70 km) width at the latitude of

Yaquina Bay. The maximum uplift was designed to equal about 6 m, approximately twice the expected uplift from 15-20 m of slip on a fault dipping about 10 degrees. The asperity was placed at 865 m depth near the continental slope-shelf break at Stonewall Bank (Appendix C). Since the asperity uplift was superimposed on a regional fault rupture to achieve a local doubling of uplift, no compensating decrease in slip and uplift occurs in adjacent areas. The sea floor deformation is thus only valid in the immediate area of the asperity. For this reason, only simulations of the initially arriving tsunami are utilized for hazard mapping, since that wave is controlled by the near field deformation, whereas later arriving waves would be influenced by far field deformation. Future simulations of asperities should utilize the fault rupture model to produce sea floor deformation by redistributing slip, rather than superimposing an arbitrary uplift. This procedure was beyond the scope of the present investigation.

Table 1 summarizes the main features of the fault rupture models. Only three of the models are utilized for tsunami hazard mapping at Yaquina Bay.

Table 1. Fault rupture parameters for each model. Rupture widths are at the latitude of Yaquina Bay except Model 2Cn, which does not reach Yaquina Bay. The width for Model 2Cn is at the latitude of Siletz Bay, 30 km north of Yaquina Bay. Model 1A Asperity slip is only an estimate, since no fault rupture model was run to generate this Gaussian asperity. See Appendix C for further details (STZ = seaward transition zone; LTZ = landward transition zone; LZ = locked zone).

Model	Used for Yaquina Bay map?	Rupture Length (km)	Rupture Width (km)	Slip Distribution STZ	Slip Distribution LTZ	Slip (m)	M_w
1A + Asperity (1ArunD)	Yes	1,050	70	100% of LZ slip	Down-dip linear decrease from 100 to 0 % of LZ slip	~35 at asperity	9.1
1A	Yes	1,050	70	100% of LZ slip	Down-dip linear decrease from 100 to 0 % of LZ slip	17.5	9.1
1B	No	1,050	70	Up-dip linear decrease from 100 to 0 % of LZ slip	Down-dip linear decrease from 100 to 0 % of LZ slip	17.5	9.0
1C	No	1,050	50	0 % of LZ slip	Down-dip linear decrease from 100 to 0 % of LZ slip	17.5	9.0
2A	No	1,050	140	100% of LZ slip	Down-dip linear decrease from 100 to 0 % of LZ slip	17.5	9.2
2B	No	1,050	140	Up-dip linear decrease from 100 to 0 % of LZ slip	Down-dip linear decrease from 100 to 0 % of LZ slip	17.5	9.2
2C	No	1,050	90	0 % of LZ slip	Down-dip linear decrease from 100 to 0 % of LZ slip	17.5	9.1
1An	No	450	70	100% of LZ slip	Down-dip linear decrease from 100 to 0 % of LZ slip	7-10	8.7
1As	No	450	70	100% of LZ slip	Down-dip linear decrease from 100 to 0 % of LZ slip	7	8.5
2Cn	No	450	65	0 % of LZ slip	Down-dip linear decrease from 100 to 0 % of LZ slip	7-10	8.7
2Cs	Yes	450	90	0 % of LZ slip	Down-dip linear decrease from 100 to 0 % of LZ slip	7	8.6

Tsunami Simulations

Appendix A explains the finite element method used to propagate tsunamis from sea floor excitation produced by the scenario earthquakes. The power of the method lies in its ability to use unstructured numerical grids that can capture the influence of small features such as shipping channels and jetties. These features are critical components of Yaquina Bay (Figure 5). This refined simulation comes at some computational cost, since the small grid spacing needed to capture these details demands small time steps on the order of 0.1 seconds and very large numbers (80,000 to 100,000)of grid nodes. The computational grid is illustrated in Appendix A, Figures A5 and A6.

The large time needed to run the simulations required that some rupture models be discarded in order to meet the project schedule. Model 1B was discarded, owing to the likely similarity of the results to Models 1A and 1C, based on the results from Models 2A, 2B, and 2C (Figure 6). Since the objective of the 450 km-long rupture models was to establish a moderately low hazard scenario, the two that seemed likely to have the least run-up were simulated, models 2Cn and 2Cs.

RESULTS

Table 2 summarizes the open coastal run-up elevation (with the effect of coseismic deformation and tide) for all fault rupture scenarios relevant to the study area. Figure 6 summarizes the relationship between total sea floor displacement (both positive and negative) versus open coastal run-up elevation (without the effect of coseismic deformation or tide) at the latitude of Yaquina Bay. It is apparent that run-up clusters into four closely similar groups in the following order (highest run-up at the top):

1. 1A Asperity
2. 1A, 1C, (and probably 1B, were it run)
3. 2A, 2B, 2C
4. 2Cn, 2Cs

Table 2. Open coastal run-up elevations and elevations corrected for a tide at mean higher high water (1.3 m above geodetic mean sea level) and for coseismic subsidence. The coseismic subsidence is that which is caused by the fault rupture model. See Table 1 for a summary of the rupture models and Appendix C for a detailed discussion.

Fault Rupture Model	1A Asperity	1A	1C	2A	2B	2C	2Cn	2Cs
Run-up (m)	8.5	5.9	6.0	4.1	4.2	4.4	2.1	2.9
Run-up (m) (Corrected)	10.7	8.1	8.2	6.5	6.6	6.8	3.4	4.8
Max. Current Velocity in m/sec and (knots)	8.3 (16)	6.5 (13)	6.8 (13)	5.5 (11)	5.3 (10)	5.3 (10)	2.5 (5)	3.8 (7)

Figure 7 illustrates why the total displacement for the three STZ scenarios (Figure 3) are so similar. Large "spikes" of uplift occur at the updip ends of each rupture, compensating for decreased slip in the STZ.

Figure 8 illustrates the additional deformation from the asperity added to Scenario1A. Scenario 1A was chosen as the background deformation for this "worst case," because it generated the largest tsunami run-up relative to the other fault rupture models.

Figure 9 illustrates examples of tsunami current velocity and wave elevation time histories at representative sites in the study area for the "moderately high" run-up case, scenario 1A. These illustrations are reproduced in the legend of the tsunami hazard map to guide local emergency and port planners regarding expected wave arrival times and hazardous currents.

The largest differences in run-up and inundation occurred between the 1,050 km ruptures, the 450 km ruptures, and the asperity scenario. All other variations were relatively minor, producing inundation that was difficult to map separately in the Yaquina Bay area, owing to its relatively high relief and shoreline protection from jetties and foredunes. The chosen scenarios were given qualitative names to make them more understandable to the public. Table 3 lists inundation scenarios that can be shown on tsunami hazard maps where relief is low and few shoreline barriers limit inundation. Only three of these scenarios could be distinguished in the Newport area, given local topographic conditions and the base map scale. These three were approved by a local government advisory committee. Figure 5 illustrates the large differences in inundation among the three.

Table 3. Tsunami inundation scenarios that can be mapped separately in areas of low relief. Because of the high relief, only three of these scenarios were mapped at Newport. All five will be used for a tsunami hazard map of Seaside, Oregon, where relief is much lower.

Qualitative Map Label	Model	Mapped for Newport?
High	1A + Asperity	Yes
Moderately High	1A	Yes
Moderate	2A, 2B, or 2C	No
Moderately Low	2Cs or 2Cn	Yes
Low	1964 Alaska Teletsunami	No

DISCUSSION

As illustrated by the tsunami simulations of Priest (1995) and theoretical work of Tadepalli and Synolakis (1994), an offshore trough of coseismic subsidence leads to higher run-up than an onshore trough, other factors being equal. Scenario 1A, the narrow rupture, thus generated higher run-up than Scenario 2A at Yaquina Bay (Table 2).

As the fault slip in the STZ decreases from Scenarios 2A to 2C (Table 1); tsunami run-up should decrease as well for most parts of the subduction zone. However, this observation is complicated by the "spikes" of anomalous uplift in Scenarios B and C which effectively keep the total volume of deformation similar in each case (Figures 6 and 7). This probably accounts for the close similarity of open coastal run-up for models 2A, 2B, and 2C (Table 2). No tsunami simulation was run for model 1B, since it was apparent that it would not differ significantly from models 1A and 1C (Figure 6).

In near-source areas the initially arriving tsunami wave is mostly controlled by the shape of coseismic deformation (Tadepalli and Synolakis, 1994), so the initial wave for the 450 km rupture model (Model 2Cs) resembles the equivalent waves from the 1,050 km ruptures. However the decreased slip in this model causes a nearly proportional decrease in run-up at the coast (Table 2; Figure 6), as expected from earlier work of Geist and Yoshioka, (1996).

The 450 km rupture scenario, compared to the 1,050 km scenario, also affects a much smaller part of the Cascadia margin with near-source tsunamis, although, as noted by Geist and Yoshioka (1996), oblique wave fronts propagate north and south from the ends of the rupture. These features will produce time histories on the margin quite different from the 1,050 km scenarios, as oblique wave fronts refract and reflect up and down the coast. This is not an issue for the Yaquina Bay simulation, since the 450 km rupture (Scenario 2Cs) is located immediately offshore.

The inundation was found to be sensitive to local barriers. When run-up exceeds the height of foredunes and jetties, inundation increased dramatically (Figure 5; Figures A15a-g, Appendix A). Scenario 2Cs has minimal inundation because it does not overcome most barriers in the area. Scenarios 1A, 1C, 2A, 2B, 2C overtop most barriers, but do not have a great deal of volume to inundate. In contrast, the asperity scenario has enough volume to flood essentially all areas below about 3-4 m of elevation, even those 3 km from the open coast (Figure 5).

POTENTIAL ERRORS

Types of Bottom Deformation Not Simulated: The fault dislocation scenarios do a reasonable of job exploring large scale variation in regional flexure of the North American

plate, but all suffer from over simplification. In particular, none of them explicitly simulate submarine landslides or partitioning of the slip into individual faults and folds.

Submarine landslides and turbidity currents associated with a great earthquake can also generate tsunamis. Landslides on the order of tens of kilometers wide have been mapped on the continental slope (e.g. Goldfinger and others, 1992b). None of the scenarios address this type of bottom deformation.

If local faults, asperities, and submarine landslides occur together, then even the asperity model could possibly underestimate the hazard. For example, a major asperity should greatly amplified shaking, which could enhance the chance of a major submarine landslide. Heceta Bank offshore of Florence, a possible location of an asperity (Goldfinger, 1994), is also the locality of one of the largest mapped landslides on the continental slope (see the maps of Goldfinger and others, 1992a; 1992b). Likewise, some of the steepest parts of the continental slope occur in northern California seaward of major thrust faults shown by Clarke and Carver (1992) to partition significant amounts of slip.

"Spikes" of Uplift: All of the rupture models produce sharp "spikes" of uplift at the seaward tip of ruptures (e.g. Figure 7; Figure A3, Appendix A). These "spikes" are artifacts of the assumption of perfect elastic behavior on buried ruptures, so they may be viewed in large part as model errors, since the actual ruptures will not likely terminate abruptly and deform the accretionary wedge elastically. The effect is to amplify simulated ground deformation and tsunamis, the tsunami amplification increasing as the "spikes" get higher and closer to shore (e.g. Priest, 1995; Geist and Yoshioka, 1996). Priest (1995) determined that the amplification of run-up from these "spikes" located near the deformation front is on the order of 3 percent. Scenarios 1C, 2C, 2Cn and 2Cs produce the largest of these "spikes" at the nearest shore positions. Amplification of tsunami run-up is much greater than 3 percent for these models.

Potential Error from Coupling Ratio: The coupling ratio was assumed to be 1.0 for models of the 1,050 km ruptures, but, as explained in Appendix C, the ratio is generally lower than this for subduction zone earthquakes world wide. Reducing the slip would, to a first approximation, produce almost a proportional reduction of tsunami run-up elevation, because the coast is so close to the tsunami source (Geist and Yoshioka, 1996). This source of error is on the order of 80 percent, given the range of possible coupling ratios (0.2-1.0). The error is partially addressed by the 450 km rupture scenarios, which explore an effective coupling ratio of 0.5. Lower coupling ratios, while possible, may not be useful, since derived slip would be less than 7-10 m, which, from trials at Siletz Bay (Priest and others, 1995), Crescent City and Humboldt Bay (Bernard and others, 1994), generate approximately the minimum run-up that can reasonably be expected from paleotsunami data and comparisons with world wide data for local subduction zone events.

The amount of slip chosen for the 1,050 km rupture does produce the >1.5 m of maximum coseismic subsidence estimated from paleoseismic data in southern Washington and the

Columbia River (Appendix C; Peterson and others, 1997). Since the scenario was constrained to match these data, approximately the same seismic slip would have been chosen for this scenario in the northern margin, regardless of assumed coupling ratio. There is no paleoseismic estimate of maximum coseismic subsidence south of the Columbia River, because appropriate tidally controlled marsh sites do not penetrate far enough inland to cover the projected location of the coseismic subsidence trough. A smaller amount of seismic slip (lower coupling ratio) could thus be accommodated at Yaquina Bay without violating the paleoseismic data.

Shorter Segment Ruptures: Arguments have been made by others (e.g. McCaffrey and Goldfinger, 1995; Geomatrix, 1995) for shorter segment ruptures than explored here. Such ruptures could produce much smaller slip and tsunamis, if the slip-length ratio is approximately constant, as postulated by Scholz (1982). While quite possible from a theoretical point of view, as shown by the studies of Bernard and others (1994), these ruptures would probably produce tsunamis so similar in amplitude to maximum teletsunamis that they would not be useful for hazard planning. From a planning perspective, tsunamis of this size are better addressed through modeling teletsunamis that strike far more frequently than potential Cascadia events.

Other Uncertainties in Rupture Models: The amount of vertical deformation, the principal issue for tsunami generation, is most affected by the above factors and the assumed width of the rupture. The range of possibilities for width are well covered by the fault rupture models. Uncertainties in dip on the megathrust are probably no more than a few degrees and, at the low dips of this subduction zone, the effect on vertical deformation is minimal. The effect on the assumed lateral extent on the locked and transition zones could, however, be quite substantial, since simple geometry dictates that slight changes in dip can lead to large changes in the lateral distance needed to reach to critical isotherms governing these zones (Figure Clla, Appendix C).

Error in the Tsunami Simulation: As summarized in Appendix A, simulations of the 1964 Alaskan tsunami produced satisfactory results for the largest tsunamis arriving in near source areas of Alaska. Tidal simulations also produced accurate representations of actual tidal data. These results are encouraging that the numerical simulation technique is not a major source of error, especially when compared to the very large uncertainties in the size of the source earthquake and resulting sea floor deformation; however, the Alaska simulation produced smaller than expected tsunamis in distal areas, so additional work needs to be done on the simulation.

Summary of Error Analysis: The most important source of error for tsunami generation is the sea floor deformation predicted by the rupture models. The largest sources of error in the rupture models are the amount of slip and width of the rupture. Uncertainty in the coupling ratio is the most important error in estimation of slip. A variation from an effective ratio of 1.0 to 0.5 is covered by the scenarios. South of the Columbia River the scenarios simulate locked and landward transition zone widths of 35 to 70 km (total

rupture width 70-140 km), covering most of the uncertainty in this key source of error. The scenarios cover all possibilities for slip in the STZ from near zero slip to slip throughout most of the 15-60 km width, but the elastic rupture models show little difference in tsunamis produced from these variations. This counter intuitive result is the caused by the tendency of simple elastic models to produce "spikes" of anomalous uplift on buried ruptures, the deeper a buried rupture, the larger the "spike.". The models also do not treat sea floor deformation and tsunami inundation that could be caused by landslides and secondary faulting. The numerical technique for tsunami simulation is probably not a major source of error, especially compared to the large uncertainties in the sea floor deformation.

CONCLUSIONS

Based on an analysis of paleoseismic data coupled with empirical studies of great subduction zone earthquakes, the fault ruptures on the Cascadia subduction zone may possibly encompass 45-100 percent of the Juan de Fuca-Gorda Plate interface with the North American plate. If some ruptures are segmented, a likely segment boundary lies in northern Oregon where, because of a wide accretionary wedge and high temperature of the subducted plate, the potential locked zone may be quite narrow. Fault dislocation scenarios explored three rupture lengths: one extending 1,050 km from British Columbia to northern California, one extending 450 km north of 44.8° N to Vancouver Island, and one extending 450 km south of 44.8° N to Eureka, California. Given a constant ratio of length to slip, the segment ruptures have about half the slip of the 1,050 km rupture. Within the uncertainties of the data, width of the locked zone south of the Columbia River can be as little as 35-40 km, according to interpretations of geophysical data, or about 70 km; according to interpretations of paleoseismic data, so two locked zone widths were also simulated.

Coseismic slip was assumed to decrease down dip from the locked zone in an approximately linear fashion, controlled by a similar linear increase in temperature. This landward transition zone was simulated by a zone of decreasing coseismic slip about the same width as the maximum potential width of the locked zone. Total rupture widths, combining the locked and landward transition zones are thus about 70-80 km for the narrow rupture scenario and about 140 km for the wide rupture.

Sediment accreted to the outer 15-60 km of the upper plate forms a seaward transition zone that may rupture with the upper plate nearly to the deformation front, or sustain near zero slip. Dislocation scenarios explored both extremes and an intermediate case where slip varies linearly across this zone. Anomalous "spikes" of uplift inherent in the elastic rupture models essentially eliminated any differences in total deformation between these scenarios, so they did not produce significantly different tsunamis.

Errors in estimated slip scale almost linearly to errors in tsunami run-up in near-source areas. The ratio of seismic to total slip (coupling ratio) is the most important source of

error in the slip estimates. Ratios of 0.2-1.0 are possible. Use here of a coupling ratio of 1.0 probably overestimates the hazard somewhat, particularly in the central and southern part of the margin. The segmentation scenarios with about 7-10 m of slip on 450 km-long ruptures may be viewed as simulating a coupling ratio of 0.5 over the average recurrence of 450 years (15-20 m of plate convergence).

The 7-10 m of slip derived from the segmentation scenarios approximates the minimum needed to produce run-up estimated from Cascadia paleotsunami data at Siletz Bay. Smaller slips, although theoretically possible, would produce run-up approximating teletsunamis, adding little to the Cascadia hazard analysis.

A worst case scenario was developed by assuming that uplift from a local asperity immediately offshore of the study area would produce uplift about twice as high as the regional uplift for the Model 1A (M_w 9.1) earthquake. The worst case scenario is intended to emulate asperities inferred for the 1960 Chilean (Barrientos and Ward, 1990) and 1946 Nankai (Yabuki and Matsu'ura, 1992) earthquakes where asperities on the order of 100 km wide by 150 km long had approximately twice the average slip for the subduction zone rupture as a whole. The model asperity was generated by adding a 150 x 100 km Gaussian uplift to the coseismic deformation for Model 1A. The maximum uplift was designed to equal about 6 m, approximately twice the expected uplift from 15-20 m of slip on a fault dipping about 10 degrees. The resulting tsunami was about 40 percent higher than the same rupture without the asperity. The tsunami had a large enough volume to inundate all areas around Yaquina Bay below about 3-4 m, even 3 km inland of the open coast.

Three scenario earthquakes were chosen in order to provide useful planning scenarios for tsunami hazard mitigation at Yaquina Bay. Inundation for high, moderately high, and moderately low run-up cases were mapped, corresponding, respectively, to a magnitude 9+ earthquake with an asperity immediately offshore, the same earthquake without an asperity, and a magnitude 8.5 earthquake with about half the slip of the magnitude 9+ case. Respective open coastal run-up elevations at Newport were 11, 8, and 5 m. Open coastal run-up of at least two other scenarios could be mapped in other areas with lower relief than Yaquina Bay, but these three are all that can be practically depicted in this area of relatively high relief and extensive shoreline barriers.
Oregon Department of Geology and Mineral Industries maps IMS–2 and IMS–3 illustrate the expected inundation at Newport and Seaside, respectively (Priest and others, 1997; Priest and others, in prep.).

ACKNOWLEDGMENTS

Hiroo Kanamori of the California Institute of Technology, Thomas S. Yelin and Samuel H. Clarke of the U.S. Geological Survey, and Robert S. Crosson of the University of Washington gave generously of their time in discussions of possible fault slip and magnitude for subduction zone earthquakes. Chris Goldfinger of Oregon State University provided the estimated width of the seaward transition zone and provided valuable

criticism of the paper. The project was supported by grants from the Oregon Department of Justice and the U.S. Geological Survey's National Earthquake Hazard Reduction Program award number 1434-HQ096-6R-02712. The base map and digital terrain model were produced by the U.S. Army Corps of Engineers with support from the City of Newport. The base map was produced in part from earlier photography generated with support from the Federal Emergency Management Agency and Oregon Coastal Management Program, Oregon Department of Land Conservation and Development, from funds provided by the Oregon Legislature, U.S. Department of Commerce National Oceanographic and Atmospheric Administration office of Coastal Resource Management under Section 306 Coastal Zone Management grants, and Section 309 Program Enhancement grants. Support was also provided by the Oregon Department of Geology and Mineral Industries.

REFERENCES CITED

Atwater, B. F., 1996, Coastal evidence for great earthquake in western Washington, *in* Rogers, A.M., Kockleman, W.J., Priest, G.R., and Walsh, T.J., eds., Assessing and reducing earthquake hazards in the Pacific Northwest: U.S. Geological Survey Professional Paper 1560, p. 77-90.

Atwater, B.F., Nelson, A.R., Clague, J.J., Carver, G.A., Yamaguchi, D.K., Bobrowsky, P.T., Bourgeois, J., Darienzo, M.E., Grant, W.C., Hemphill-Haley, E., Kelsey, H.M., Jacoby, G.C., Nishenko, S.P., Palmer, S.P., Peterson, C.D., and Reinhart, M.A., 1995, Summary of coastal geologic evidence for past great earthquakes at the Cascadia subduction zone: Earthquake Spectra, v. 11, no. 1, p. 1-18.

Barrientos, S.E., and Ward, S.N., 1990, The 1960 Chile earthquake: inversion for slip distribution from surface deformation: Geophysical Journal International, v. 103, p. 589-598.

Bernard, E., Mader, C., Curtis, G., and Satake, K., 1994, Tsunami inundation model study of Eureaka and Crescent City, California: NOAA Technical Memorandum ERL PMEL-103, 80 p.

Clarke, S.H., Jr., and Carver, G.A., 1992, Late Holocene tectonics and paleoseismicity, southern Cascadia subduction zone: Science, v. 255, p. 188-192.

Darienzo, M.E., and Peterson, C.D., 1995, Magnitude and frequency of subduction zone earthquakes along the northern Oregon coast in the past 3,000 years: Oregon Geology, v. 57, no. 1, p. 3-12.

Flueck, P., Hyndman, R.D., and Wang, K., in press, 3-D dislocation model for great earthquakes of the Cascadia subduction zone, Journal of Geophysical Research.

Geist, E., and Yoshioka, S., 1996, Source parameters controlling the generation and propagation of potential local tsunamis along the Cascadia margin: Natural Hazards, v. 13, p. 151-177.

Geomatrix Consultants, 1995, 2.0, Seismic source characterization, *in* Geomatrix Consultants, Seismic design mapping, State of Oregon: Final Report prepared for Oregon Department of Transportation, Project No. 2442, p. 2-1 to 2-153.

Goldfinger, C., 1994, Active deformation of the Cascadia forearc: implications for great earthquake potential in Oregon and Washington: Corvallis, Oreg., Oregon State University Ph.D. thesis, 202 p.

Goldfinger, C., Kulm, L. D., Yeats, R.S., Applegate, B., MacKay, M.E., and Moore, G.F., 1992a, Transverse structural trends along the Oregon convergent margin: Geology, v. 20, p. 141-144.

Goldfinger, C., Kulm, L. D., Yeats, R.S., Mitchell, C., Weldon, R.E., III, Peterson, C.D., Darienzo, M.E., Grant, W., and Priest, G., 1992b, Neotectonic map of the Oregon continental margin and adjacent abyssal plain: Oregon Department of Geology and Mineral Industries Open-File Report O-92-4, 17 p.

Hyndman, R.D., Wang, K., Yuan, T., and Spence, G.D., 1993, Tectonic sediment thickening, fluid expulsion, and the thermal regime of subduction zone accretionary prisms: The Cascadia margin off Vancouver Island: Journal of Geophysical Research, v. 98, p. 21,865-21,876.

Hyndman, R.D., and Wang, K., 1995, The rupture zone of Cascadia great earthquakes from current deformation and the thermal regime: Journal of Geophysical Research, v. 100, no. B11, p. 22,133-22,154.

McCaffrey, R., and Goldfinger, C., 1995, Forearc deformation and great subduction earthquakes: implications for Cascadia offshore earthquake potential: Science v. 267, p. 856-859.

Nelson, A. R., Atwater, B. F., Bobrowsky, P. T., Bradley, L., Clague, J. J., Carver, G. A., Darienzo, M. E., Grant, W. C., Krueger, H. W., Sparkes, R., Stafford, T. W., Jr., and Stuiver, M., 1995, Radiocarbon evidence for extensive plate-boundary rupture about 300 years ago at the Cascadia subduction zone: Nature, v. 378, no. 23, p. 371-374.

Okada, Y., 1985, Surface deformation due to shear and tensile faults in a half-space: Bulletin of the Seismological Society of America, v. 75, no. 4, p. 1135-1154.

Peterson, C. D., Barnett, E.T., Briggs, G.G., Carver, G.A., Clague, J.J., and Darienzo, M.E., 1997, Estimates of coastal subsidence from great earthquakes in the Cascadia subduction zone, Vancouver, Island, B.C., Washington, Oregon, and northernmost California: Oregon Department of Geology and Mineral Industries Open-File Report O-97-5, 44 p.

Priest, G. R., 1995, Explanation of mapping methods and use of the tsunami hazard maps of the Oregon coast: Oregon Department of Geology and Mineral Industries Open-File Report O-95-67, 95 p.

Priest, G.R., Baptista, A., Qi, M., Peterson, C.D., and Darienzo, M.E., 1995, Simplified explanation of the tsunami hazard map of the Siletz Bay area, Lincoln County, Oregon *in* Priest, G.R., ed., Explanation of mapping methods and use of the

tsunami hazard map of the Siletz Bay area, Lincoln County, Oregon: Oregon Department of Geology and Mineral Industries Open-File Report O-96-5, p. 1-20.

Priest, G.R., Myers, E., Baptista, A., Kamphaus, R., Peterson, C.D., and Darienzo, M.E., 1997, Tsunami hazard map of the Yaquina Bay area, Lincoln County, Oregon: Oregon Department of Geology and Mineral Industries Interpretive Map Series map IMS–2, scale 1;12,000.

Priest, G.R., Myers, E., Baptista, A., Kamphaus, R., Peterson, C.D., and Darienzo, M.E., in preparation, Tsunami hazard map of the Seaside-Gearhart area, Clatsop County, Oregon: Oregon Department of Geology and Mineral Industries Interpretive Map Series map IMS–3, scale 1;12,000.

Satake, K., Shemazaki, K., Yoshinobu, T., and Ueda, K., 1996, Time and size of a giant earthquake in Cascadia inferred from Japanese tsunami records of January 1700, 1996, Nature, v. 379, no. 6562, p. 246-249.

Scholz, C. H., 1982, Scaling laws for large earthquakes: consequences for physical models: Bulletin of the Seismological Society of America, v. 72, no. 1, p. 1-14.

Tadepalli, S., and Synolakis, C.E., 1994, The run-up of N-waves on sloping beaches: Proceedings of the Royale Society of London, v. A445, p. 99-112.

Weaver, C.S., and Shedlock, K. M., 1989, Potential subduction, probable intraplate, and known crustal earthquake source areas in the Cascadia subduction zone, *in* Hays, W.W., ed., Proceedings of the 3rd Annual Workshop on Earthquake Hazards in the Puget Sound, Portland area: U.S. Geological Survey Open-File Report 89-465, p. 11-26.

Whitmore, P. M., 1993, Expected tsunami amplitudes and currents along the North American coast for Cascadia subduction zone earthquakes: Natural Hazards, v. 8, p. 59-73.

Whitmore, P. M., 1994, Expected tsunami amplitudes off the Tillamook County, Oregon, coast following a major Cascadia subduction zone earthquake: Oregon Geology, v. 56, no. 3, p. 62-64.

Yabuki, T., and Matsu'ura, M., 1992, Geodetic data inversion using Bayesian information criterion for spatial distribution of fault slip: Geophysical Journal International, v. 109, p. 363-375.

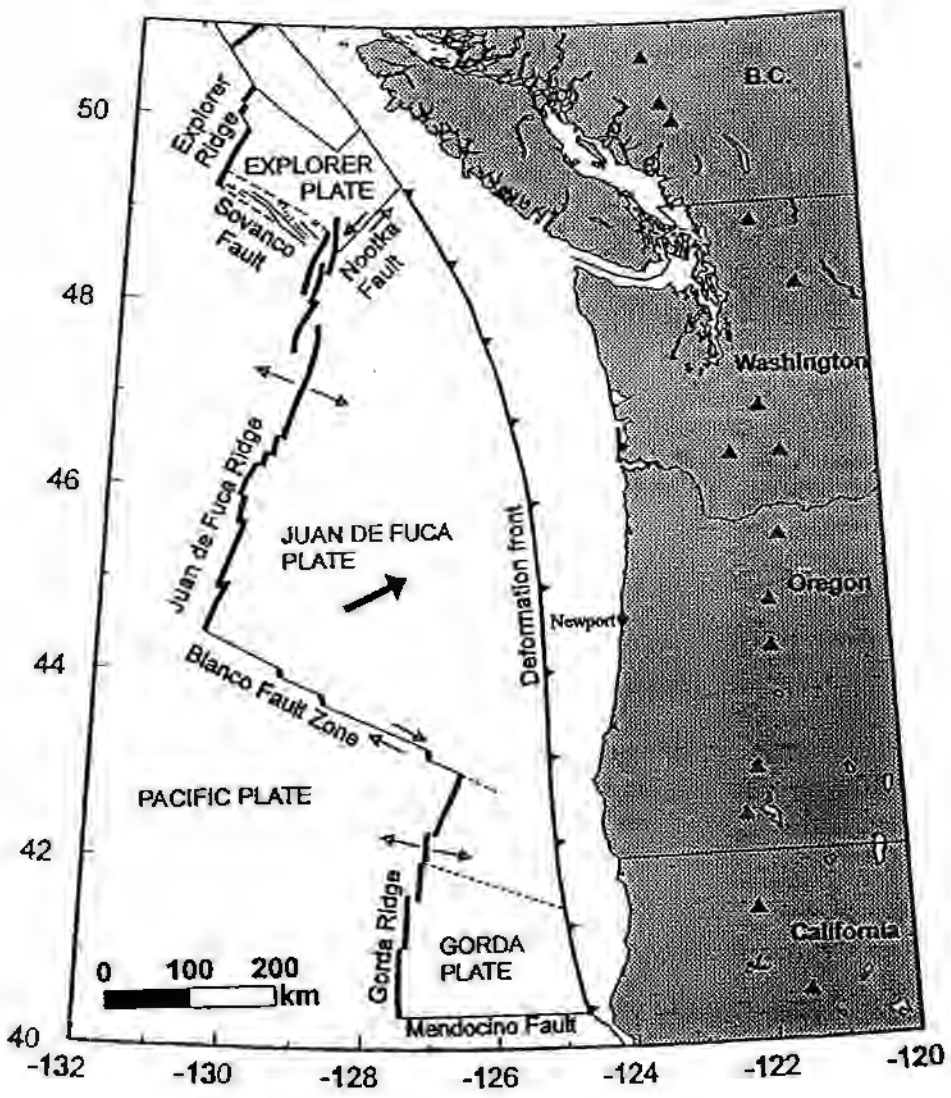

Figure 1. Plate tectonic map of the Cascadia subduction zone fault system illustrating the location of the surface trace of the fault at the deformation front relative to the Newport-Yaquina Bay study area. The subduction zone is bounded by the Nootka and Mendocino transform faults and dips 8-12° toward the east. Figure modified from Fleuck and others (in press).

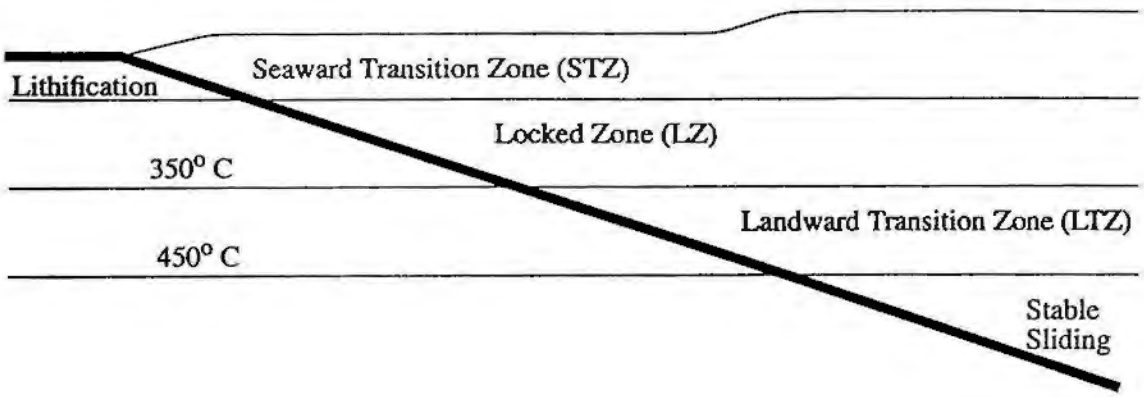

Figure 2. Schematic illustration of the zones of slip in a subduction zone. As water-saturated sediments at the deformation front become progressively lithified, the fault behaves with more and more stick-slip behavior until it is fully locked at the base of the seaward transition zone (STZ). In the landward transition zone (LTZ), the fault movement changes from stick slip to stable sliding behavior as the temperature rises. Coseismic ruptures may penetrate through all or part of the STZ, as illustrated in Figures 3 and 4.

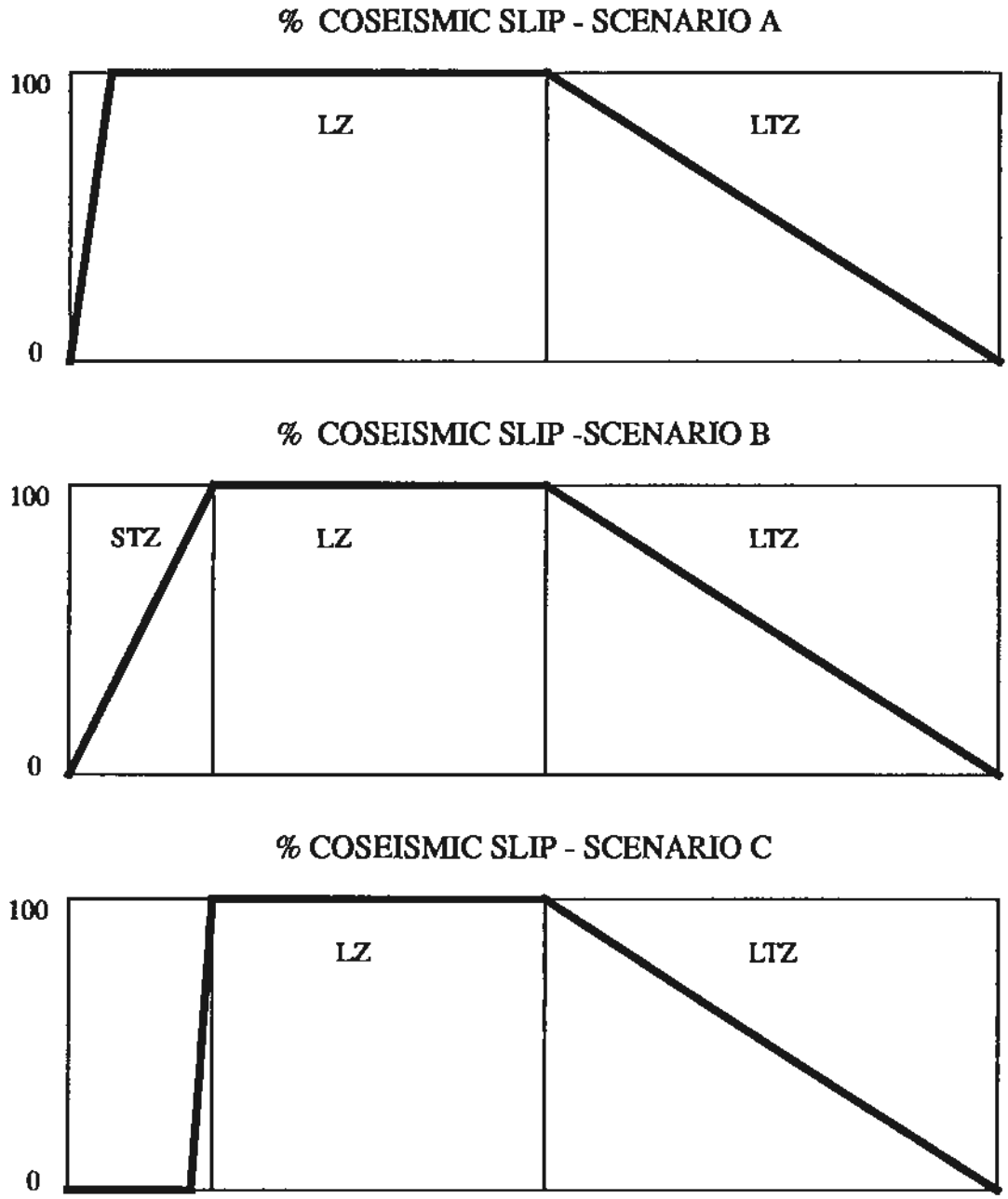

Figure 3. Schematic illustration of the coseismic slip distributions for STZ scenarios considered here. Scenario A assumes a maximum penetration of the coseismic rupture into the STZ, Scenario B a linear transition of slip across the STZ, and Scenario C little penetration of the rupture into the STZ.

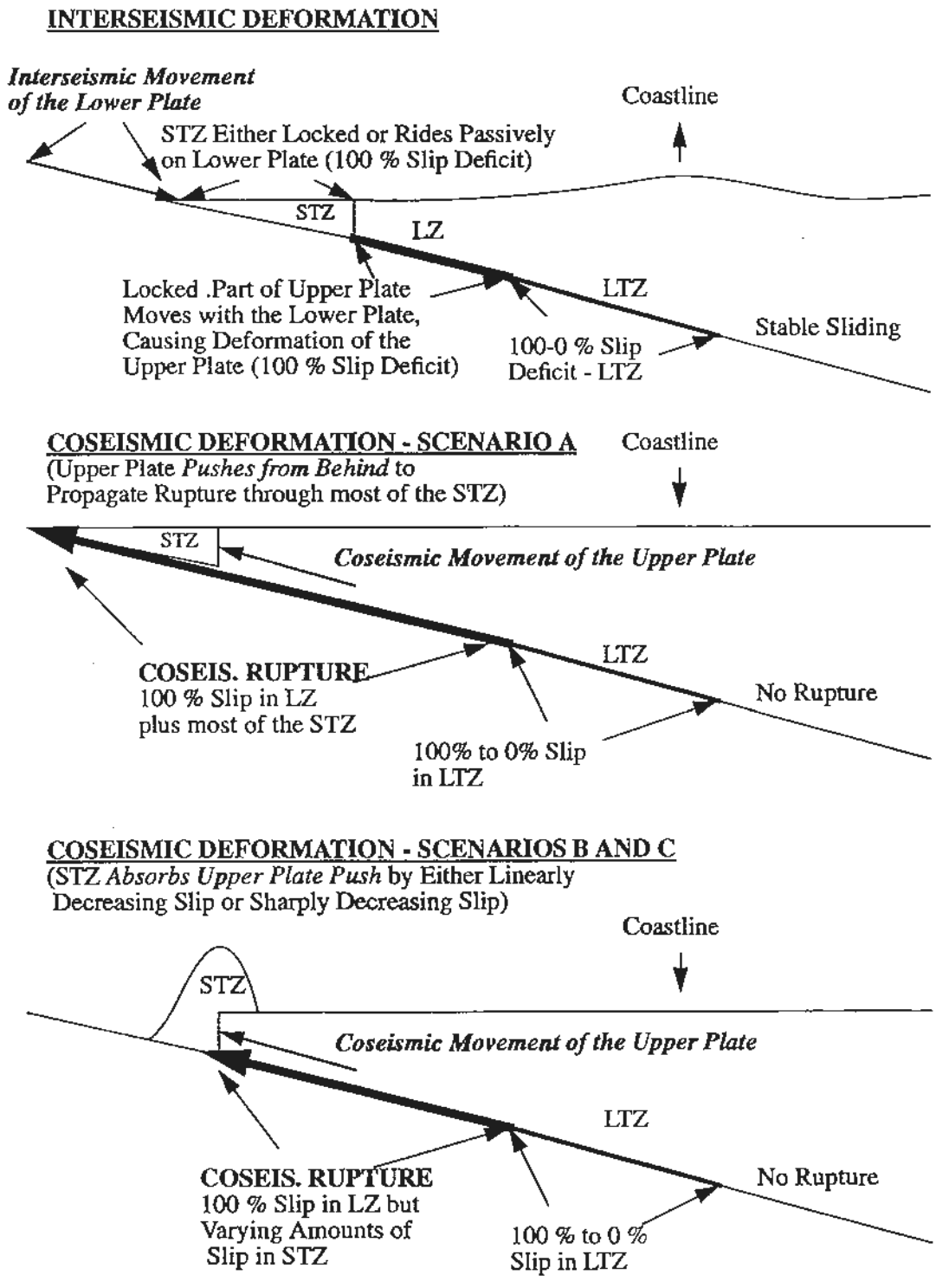

Figure 4. Schematic illustration of interseismic and coseismic deformation for various scenarios considered here. The upper plate "pushes from behind" during the earthquake, propagating a rupture either partially (Scenarios B and C, Figure 3) or completely (Scenario A, Figure 3) through the STZ. Rupture propagation may not be entirely correlated to the degree of interseismic "locking" within the STZ or the coseismic energy released, if the rupture propagates through the very weak, water saturated parts of the STZ.

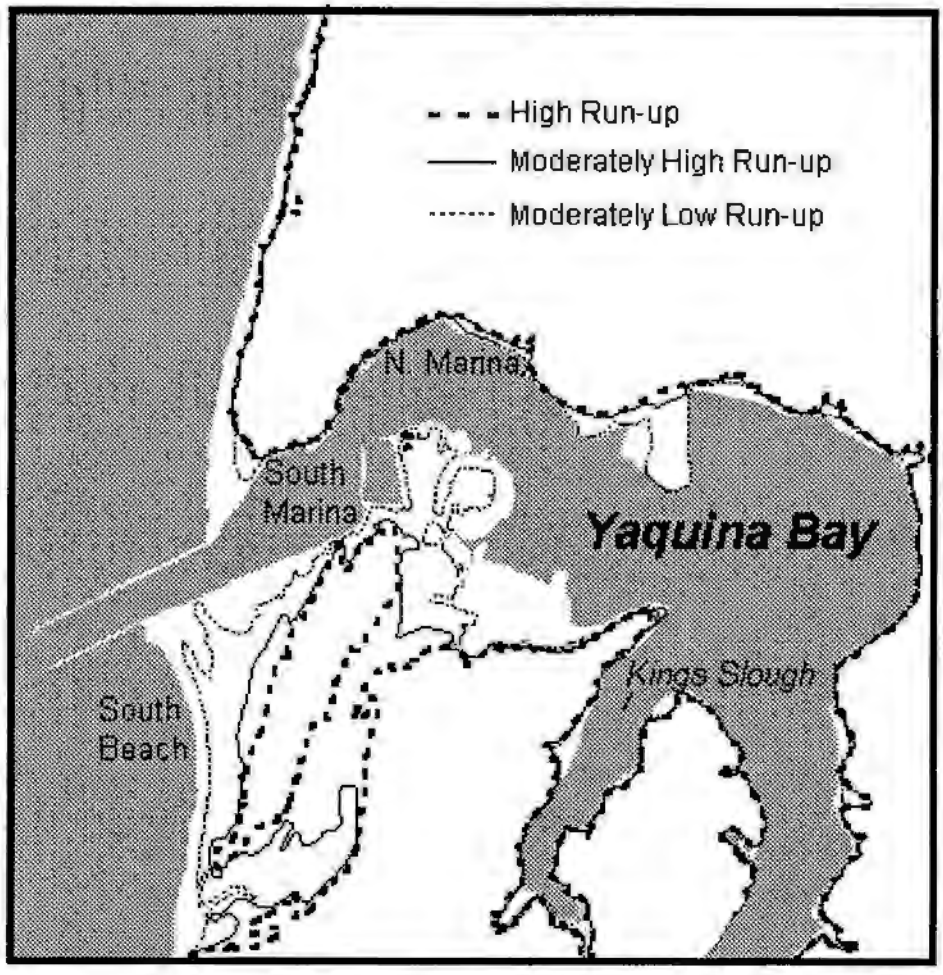

Figure 5. Tsunami Inundation map of the Yaquina Bay area, Newport, Oregon. Moderately low run-up inundation line (Model 2Cs) outlines foredunes in the southwestern part of the area. High run-up (Model 1A Asperity) inundation lines outline two highlands in the southwestern part of the area with a flooded zone between. Moderately high inundation (Model 2B) floods the foredunes but does not fully flood the zone between the two highlands in the southwestern area. Note how the inundation lines fuse in the steep terrain that dominates the rest of the study area.. Map is about 6.5 km wide.

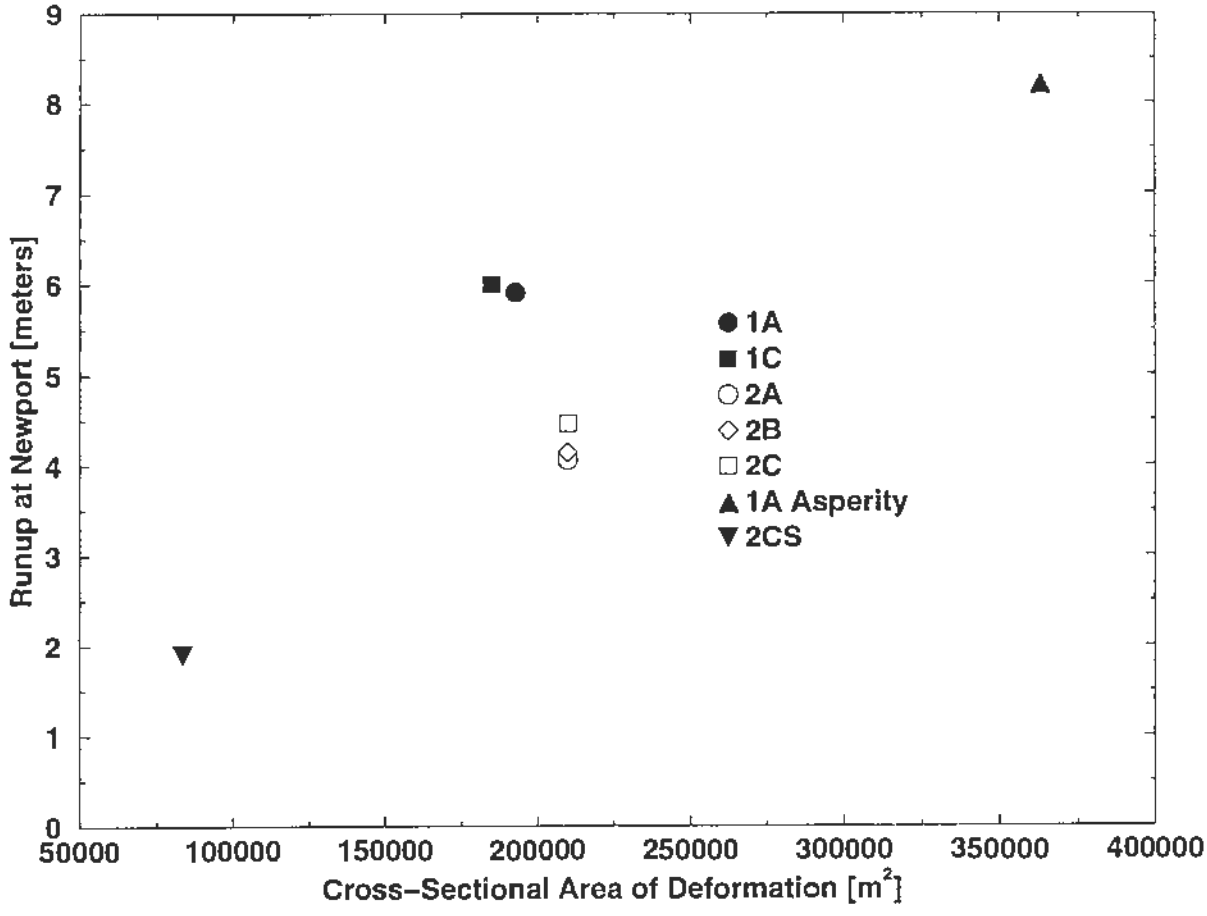

Figure 6. Covariance of open coastal run-up elevation with total positive and negative sea floor deformation for all models relevant to the Newport study area. Note (1) the similarity of run-up between the scenarios differing only with respect to slip in the STZ (e.g. 2A, 2B, and 2C; see Figure 7), (2) higher run-up of the narrow rupture scenarios (e.g. 1A) versus the wide rupture cases with the same slip (e.g. 2A), and nearly linear dependence of run-up on slip (see Table 1 for slip values).

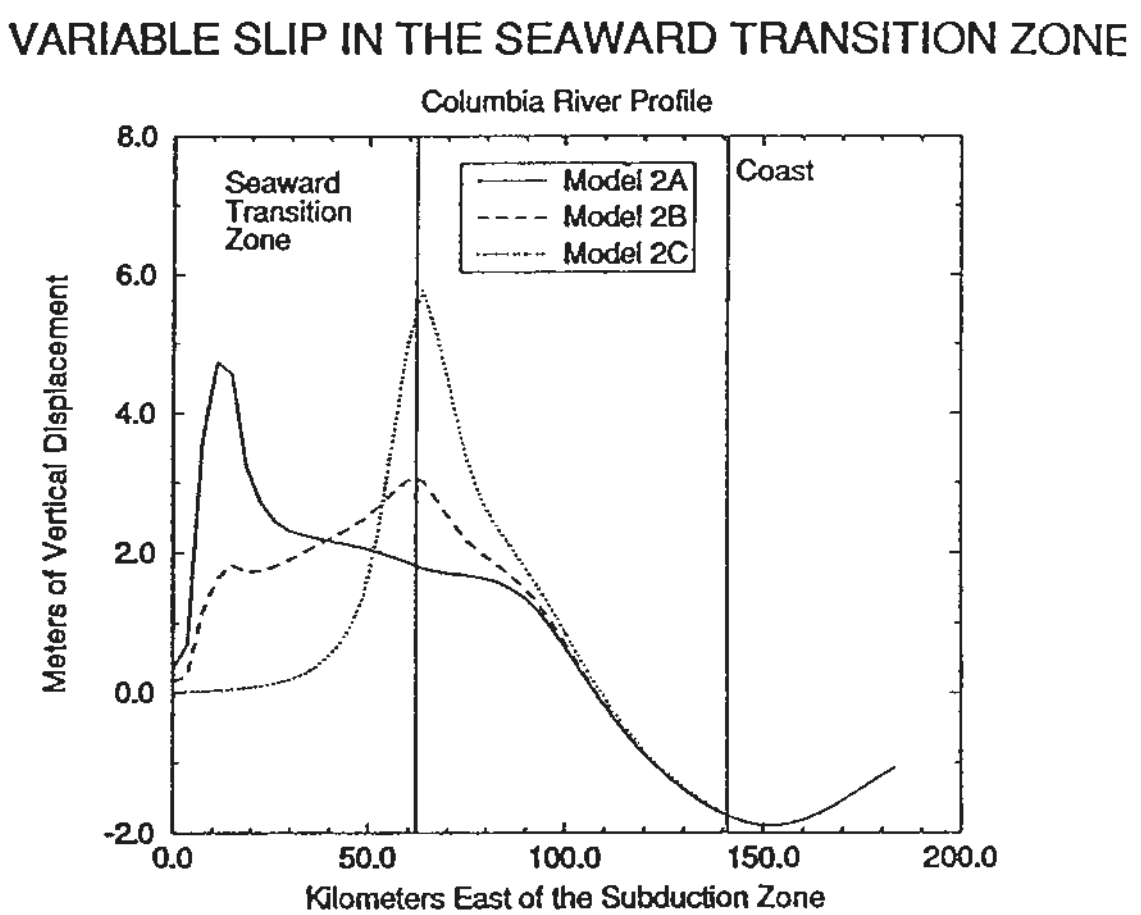

Figure 7. Examples of three fault rupture models sharing the same overall width and geometry (Model 2, the 140 km-wide case) but with slip in the STZ varying as in Figure 3 for scenarios A, B, and C. Note how the overall amount of displacement is about the same for each case (Figure 6).

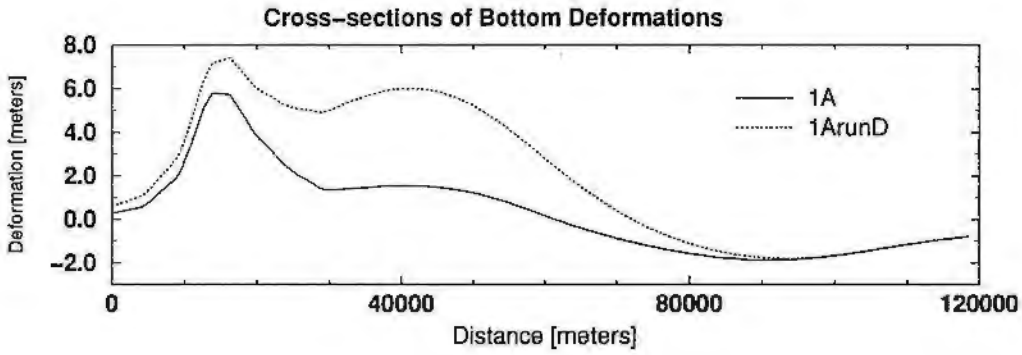

Figure 8. Comparison of the cross sectional profile of the narrow rupture scenario (Model 1A) with the same scenario but with a Gaussian uplift 100 km wide (at 2 sigma) and reaching 6 m height. The latter scenario emulates doubling of slip at an asperity on the subduction zone.

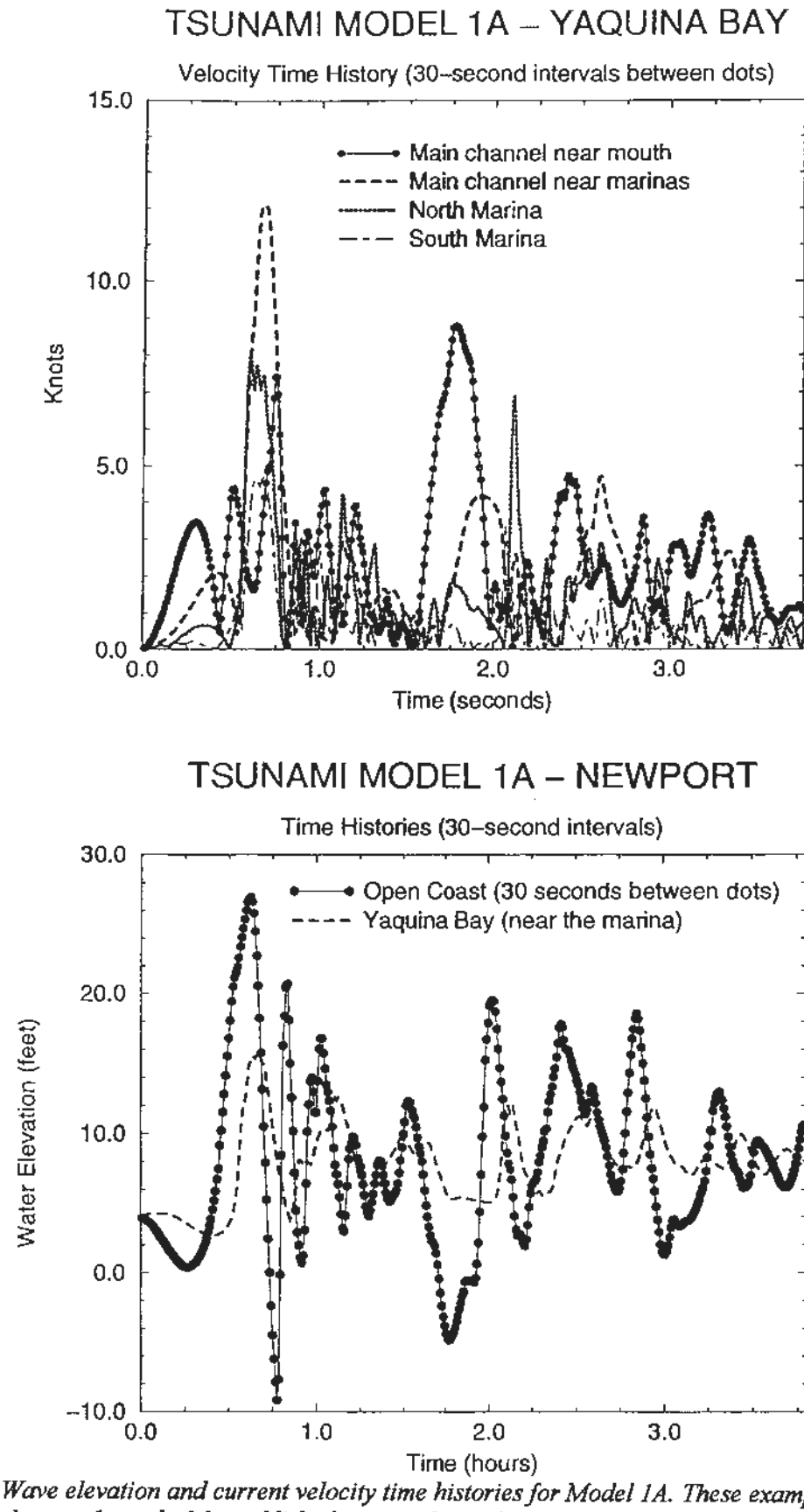

Figure 9. Wave elevation and current velocity time histories for Model 1A. These examples were shown on the map legend of the published tsunami hazard map.

Appendix A
Evaluation of Coastal Tsunami Hazards in Newport, Oregon Through the Use of a Finite Element Hydrodynamic Model

Edward Myers and António Baptista
Center for Coastal and Land-Margin Research
Oregon Graduate Institute of Science & Technology

Introduction

Communities bordering the Pacific Ocean are at an increased risk of being impacted by tsunamis due to the more frequent occurrence of subduction zone earthquakes in the Pacific basin. The most devastating damage from a tsunami will generally occur in coastal venues which are in close proximity to the subduction zone, but tsunami waves may also traverse the ocean to more distant lands in its path. While all Pacific Ocean communities are vulnerable to these latter transoceanic tsunamis, the city of Newport, Oregon is also susceptible to locally generated Cascadia Subduction Zone tsunamis.

The need to mitigate coastal hazards from either a Cascadia tsunami or a transoceanic tsunami has been identified, for example, by Oregon State Senate Bill 379 which limits construction of critical facilities in potential tsunami inundation zones. In this study, a finite element hydrodynamic model is utilized to assess the risks associated with the propagation and inundation of potential Cascadia and transoceanic tsunamis in the Newport, Oregon vicinity.

Current methods of modeling tsunamis carry a certain amount of uncertainty associated with how the earthquake mechanism will give shape to the initial tsunami wave and with the model's ability to reproduce the true physics of the waves' propagation and inundation. Steps are taken in this study to minimize and evaluate such uncertainties, thus permitting a clearer vantage of the physical processes affecting the evolution of potential tsunamis in Newport.

Modeling results are presented in a manner that is intended to be of practical use to hazard mitigation efforts. Such results include inundation patterns, spatial variation of maximum wave elevations, and velocity patterns in coastal regions. These results, combined with the insight gained throughout the modeling experience, help to procure a thorough assessment of the tsunami hazards posed to the Newport community.

Modeling Approach

The primary challenge in evaluating future tsunami hazards for a coastal community is to estimate how future subduction zone earthquakes will occur. Even though no two earthquakes are ever the same, our only clues as to what may potentially occur in the future come from what we know happened in the past. We know the Oregon coast has experienced large Cascadia subduction earthquakes approximately every 200-600 years, and that the last such event occurred about 300 years ago. The evidence supporting this is summarized by Atwater et. al. (1995). There is also significant documentation of a recent transoceanic tsunami which impacted the Oregon coastline: the 1964 Alaska tsunami.

Utilizing data, theories, documentation, and evidence from the 1964 Alaska event and prehistoric Cascadia events, this modeling study aims to simulate these past tsunamis as an indicator of what hazards the Newport community may face in the future. As mentioned in the Introduction, though, there are many sources of uncertainty which are associated with estimating the seismic sources of these past events and with how well the numerical model can represent the propagation and inundation of the tsunami waves.

Several tools are available for systematically disseminating various modeling uncertainties and interpreting the physical mechanisms of the waves. First, estimates of how the floor of the ocean deformed during the earthquake need to be made using the state-of-the-art in deformation modeling constrained by as much geologic and geophysical evidence as is possible. Second, the hydrodynamic model's ability to properly propagate waves will be monitored through the development of a regional tide model for the eastern north Pacific Ocean. The tide model will serve three primary purposes, (a) to ensure that our modeling can properly simulate this more-controlled application (tides should be reproducible to within tens of centimeters), (b) to understand the physical mechanisms affecting tidal propagation across various bathymetric domains, and (c) to provide input to modeling exercises examining the influence of tide and tsunami interaction on both wave propagation and inundation. Modeling of the 1964 Alaska tsunami will also help to verify the model's ability to propagate tsunami waves. Finally, physical interpretation of the tide and tsunami simulations will be complemented by close monitoring of numerical errors from the vantage of mass conservation, energy preservation, and truncation error analysis.

There are three critical components to numerical modeling of tsunamis: 1) estimating the deformation to the ocean floor caused by the subduction earthquake, 2) propagating the waves generated by the initial deformation, and 3) allowing the modeled waves to inundate coastal lands as the waves reach the coast. Each of these components are discussed in more detail next.

Initial Conditions: Deformation

Finite element simulations of tsunamis are dependent upon the sea floor deformation resulting from the subduction earthquake. This deformation basically maps itself into the water column and is therefore treated as an initial condition in the hydrodynamic modeling of the ensuing tsunami. Wave and velocity patterns are thus highly dependent upon the assumed deformation to the ocean floor. This deformation must be computed through the use of dislocation models such as those presented by Okada (1985) and Mansinha and

Smylie (1971). Dislocation models use fault parameters such as the length, width, dip angle, strike direction, rake angle, and slip to compute the deformation assuming an elastic half-space. Deformation computations for most tsunami modeling has, in the past, been achieved by either assuming some characteristic shape without a dislocation model (Hebenstreit and Murty 1989, Ng et. al. 1990) or by using a dislocation model and an assumption of a rectangular fault locked over its entire area prior to rupture (Myers and Baptista 1995, Whitmore 1993). The magnitudes of tsunami waves generated using the latter approach as compared with tide gauge responses demonstrate that the deformations appear to be the right order of magnitude. However, there is a plethora of ambiguity incorporated in the assumptions of the fault parameters as well as the location of the locked zone.

A better approach is to incorporate the wide range of heterogeneity of the fault zone (all of the dips and curves, etc.) into the dislocation model as well as allowing transition zones where the slip will be less than that occurring in the fully locked zone. Flück and Wang (1996) permits such an approach by not relying on the typical rectangular source formulas for computing deformation in an elastic half-space. Instead, the subduction is represented by the integration of many point sources throughout the subduction zone. Okada (1985) provides the necessary formulas for computing the deformation resulting from a point source as well as the rectangular source. Using the algorithm and program provided by Flück and Wang (1996), it is feasible to computationally break the fault up into a grid of triangular elements. The nodes of these elements contain information about the horizontal and vertical positions of the fault at that point. Over each triangle, the slip and direction of convergence are specified, which permits varying amounts of slip in different regions of the fault zone such as in transitions from full to partially locked conditions.

Geist and Yoshioka (1996) followed a similar approach to modeling the deformation by using a three-dimensional elastic finite element model. In that study, rupture along five different types of faults were considered for the Cascadia subduction zone. These included interplate thrust (rupture along the locked zoned), décollement (rupture updip of the locked zone), landward and seaward vergent thrust faults (rupture along abrupt branches from the décollement to the surface), and prominent thrust fault rupture near the edge of the continental shelf. The seaward vergent faulting mechanism is theorized (Fukao, 1979) to be characteristic of tsunami earthquakes (earthquakes which generate unusually large tsunamis as compared to the seismic moment). Geist and Yoshioka then use the resulting deformation from each of these faulting mechanisms to simulate possible tsunami impacts from each scenario, assuming different seismic parameters. These simulations are one-dimensional in space, and do not include inundation (although inundation is approximated using various runup laws). The tsunami simulations in that study are not intended to be intensive, but rather illustrative of differences in wave impacts associated with different seismic sources.

The modeling of the deformation proposed here is similar to that of Geist and Yoshioka, in terms of utilizing an elastic three-dimensional source model. The fault scenarios to be considered, though, are somewhat different. Due to the fact that many of the seaward and landward vergent thrust faults have not been seismically imaged for the entire Cascadia subduction zone (Geist and Yoshioka considered a smaller portion of the zone) and that

significant controversy still exists as to the generating mechanism of tsunami earthquakes, these types of faults are not considered here. The most probable generating mechanisms for tsunamigenic earthquakes in the Cascadia margin appear to be interplate and décollement thrust type faults. Therefore, these two mechanisms are evaluated in the contexts shown in Figure A1. Three scenarios are considered, each of which varies with respect to how the slip is distributed over the seaward transition, locked, and landward transition zones. The first scenario assumes that the locked zone actually extends all the way up to the surface of the sea floor (scenario A). The second assumes that there is a seaward transition zone in which the slip varies linearly (scenario B). Last, the third assumes that there is a seaward transition zone, but that no slip is occurring in this zone (scenario C). Each slip scenario assumes that a landward transition zone exists downdip of the locked zone.

Two different cases will be considered, with each case being comprised of the three slip scenarios mentioned above. The cases differ only in the placement of the 350° and 450° isotherms. The 350° isotherm is believed to represent the downdip extent of the locked zone due to the onset of quartz plasticity, and the 450° isotherm is theorized to represent the downdip limit of the stable sliding transition zone due to the onset of feldspar plasticity (Hyndman and Wang, 1993). The first case (case 1, combined with the above slip scenarios: 1A, 1B, and 1C) assumes the positions of these two isotherms from Hyndman and Wang's (1995) finite element model of the thermal regime. The second case (case 2, combined with the above slip scenarios: 2A, 2B, 2C) positions these two isotherms based on paleoseismic evidence. While Hyndman and Wang's isotherms are well constrained north of the Columbia River by geophysical data, poorer constraints south of this point lead to greater uncertainties, particularly in terms of comparisons with estimates of the deformation from paleoseismic data. Priest (1995) concluded that south of the Columbia River, it would be more appropriate to use limits for the landward transition zone which are different from the 350° and 450° isotherms of Hyndman and Wang. Priest derived such limits based upon paleoseismic data and previous deformation models in the Cascadia Subduction Zone. Thus, the second case considered will use Priest's limits for the landward transition zone south of the Columbia River. It should be reiterated that both cases will consider three different scenarios which differ in the way that slip is distributed in the seaward transition zone, the locked zone, and the landward transition zone. The isotherms for both cases are shown in Figure A2 along with the positions of the surface of the fault zone and the seaward transition zone which were provided by Goldfinger (1996).

In addition to these six deformation models, several shorter segment breaks will be considered. In 1995, Geomatrix Consultants performed a probabilistic acceleration map for the state of Oregon which included probability estimates of the type and recurrence interval of Cascadia subduction zone earthquakes. This study concluded that a rupture length of 450 km was most probable. Despite the fact that recognized geologic evidence indicates recurrence intervals mostly longer than 300 years, the probability study concluded that *for a 450 km rupture length*, a 225 year recurrence interval should be assumed. Using locations of local marine terraces and faults, Priest et. al. (1997) concluded that 450 km rupture scenarios should be bounded (either above or below) by the 44.8° latitude near Depoe Bay, Oregon. Segment scenarios based upon the case 2 isotherms will be considered both to the north and to the south of this latitude, extending 450 km in length (2CN and 2CS).

Cross sections of deformation at the latitude of Newport are shown in Figure A3 for all of the scenarios considered: 1A, 1B, 1C, 2A, 2B, 2C, 2CN, and 2CS. Scenarios 1A and 2A (fully locked to the surface) have large peaks of uplift near the deformation front. Case 2 has more volume of uplift for three slip scenarios than Case 1, and the region of subsidence for Case 2 is subsequently located further towards the land than Case 1. The 2CN scenario is essentially one-half of the 2C deformation, and the 2CS region of deformation is far enough south to not affect deformation at Newport.

The deformation for the 1964 Alaska tsunami will be determined without the use of the deformation model used for the Cascadia subduction zone, due to the complexity of the fault and its faulting mechanisms. Also, Holdahl and Sauber (1994) provide a comprehensive modeling study of the deformation from this earthquake. In their study, the complex faulting was modeled by separating the fault zone into a mosaic of 68 rectangular planes. The fault zone included the megathrust surface as well as the Patton Bay fault. An inversion technique was used in which single fault parameters were changed iteratively in the dislocation model of Mansinha and Smylie (1971). Geodetic and geologic measurements of the surface deformation were used as the controlling feature in the inversion. However, various other seismologic, geologic, and geodetic studies were also used to constrain the geometry of the fault surface. Their modeled deformation is the only scenario considered for this event, as it appears to be the most recent and the most comprehensive. A portrait of the deformation extracted from their study is displayed in Figure A4.

Description of Model: Governing Equations and Inundation Algorithm

In this study, the finite element model ADCIRC (Luettich et. al., 1991) is used to propagate waves in the open ocean until they reach the coastline, at which point inundation is allowed to occur. A recent extension of ADCIRC to allow for inundation and added matrix solver options (Luettich and Westerink, 1995) ensures that the state-of-the-art in finite element modeling is used here. The use of a finite element method for the hydrodynamic modeling allows the discretization to vary depending upon the bathymetric domain and numerical criteria, the coastline and topographic features may be better approximated, and the seismic source may be accurately depicted. These are more difficult to achieve through the use of a finite difference model. The seismic source was introduced to ADCIRC by adjusting the kinematic boundary condition to allow the ocean floor to dynamically move over three time steps. This is essentially equivalent to mapping the bottom deformation into the water column directly.

ADCIRC uses a generalized wave continuity formulation to supplant the primitive continuity equation, a technique which has proven to eschew the spurious $2\Delta x$ oscillations of early finite element applications. The modified generalized wave continuity equation (GWCE) is derived as a summation of the time derivative of the continuity equation, the primitive continuity equation weighted by a factor, and the spatial gradient of the momentum equations expressed in conservative form. The GWCE is used to solve for elevations, and velocities are determined from the non-conservative form of the momentum equations. The final form of the governing equations, the GWCE and momentum equations, are written as:

$$\frac{\partial^2 \eta}{\partial t^2} + G\frac{\partial \eta}{\partial t} - \frac{\partial^2 \gamma}{\partial t^2} - G\frac{\partial \gamma}{\partial t} +$$

$$\frac{\partial}{\partial x}\left\{ u\frac{\partial \eta}{\partial t} - uH\frac{\partial u}{\partial x} - vH\frac{\partial u}{\partial y} + fvH - H\frac{\partial}{\partial x}\left[\frac{p_s}{\rho_0} + g(\eta - \alpha\Psi)\right]\right\} +$$

$$\frac{\partial}{\partial x}\left\{ -E_h\frac{\partial^2 \eta}{\partial x \partial t} + \frac{\tau_{sx}}{\rho_0} - (\tau - G)uH\right\} + \qquad \text{(EQ 1)}$$

$$\frac{\partial}{\partial y}\left\{ v\frac{\partial \eta}{\partial t} - uH\frac{\partial v}{\partial x} - vH\frac{\partial v}{\partial y} - fuH - H\frac{\partial}{\partial y}\left[\frac{p_s}{\rho_0} + g(\eta - \alpha\Psi)\right]\right\} +$$

$$\frac{\partial}{\partial y}\left\{ -E_h\frac{\partial^2 \eta}{\partial y \partial t} + \frac{\tau_{sy}}{\rho_0} - (\tau - G)vH\right\} = 0$$

$$M \equiv \frac{\partial}{\partial t}\hat{v} + \hat{v} \bullet \nabla\hat{v} + \hat{f} \times \hat{v} + \tau\hat{v} + \nabla\left[\frac{p_s}{\rho_0} + g(\eta - \alpha\Psi)\right] +$$

$$\frac{E_h}{H}\left[\frac{\partial^2}{\partial x^2}\hat{v}H + \frac{\partial^2}{\partial y^2}\hat{v}H\right] + \frac{\tau_{s\hat{k}}}{\rho_0 H} = 0 \qquad \text{(EQ 2)}$$

where η is the free surface elevation, u, v are the depth-averaged velocities, H is the total water column, G is a weighting factor, γ is the bottom deformation (positive for uplift), $\hat{f}$ is the Coriolis vector, α is the effective Earth elasticity factor, Ψ is the Newtonian equilibrium tide potential, E_h is the horizontal eddy diffusion coefficient, $\tau_{s\hat{k}}$ is the applied free surface stress, τ is the bottom friction, c_f is the bottom friction coefficient, p_s is the atmospheric pressure at the free surface, ρ_0 is the reference density of water, and g is the acceleration due to gravity. A Manning formulation is used to represent bottom friction. Further details about the derivation of (EQ 1) and (EQ 2) are provided in Myers and Baptista (1995).

Dirichlet boundary conditions may be imposed in one of three manners: 1) elevations may be specified in the GWCE, 2) velocities may be enforced in the momentum equations, or 3) normal velocities may be set equal to zero to represent a no-slip condition. Transmissive boundaries have been added to ADCIRC using the first of these methods. A Lagrangian technique is used whereby the elevation at a boundary node is specified by backtracking a distance ct ($c = \sqrt{gH}$) in a direction specified by the nodal velocities ($\theta = \text{atan}[v/u]$) and interpolating the elevation from the previous time step at this location.

Inundation is handled inside ADCIRC through the use of an element based wetting and drying implementation (Luettich and Westerink, 1995a, 1995b). In this approach, elements are turned on if they are considered wet and turned off if they are considered dry.

Nodes are classified at each step as either being wet, dry, or interface nodes. Dry nodes are connected only to dry elements, interface nodes are connected to both wet and dry elements, and wet nodes are only connected to wet elements. Dry nodes are constrained to have a minimal water level and zero velocity, interface nodes have an imposed no slip condition, and wet nodes are not constrained in any manner.

Elements are allowed to dry if the water level at a node falls below a specified minimum value. If the node has recently become wet, though, the user may control the number of time steps before the node is permitted to dry (for stability purposes). Wetting of interface nodes may occur if the water level gradient favors motion toward all dry nodes connected to that interface node.

Modeling Results

Grid Setup

The semi-automatic grid generator, ACE/gredit (Turner and Baptista, 1991), permits interactive development of finite element grids. Such a flexible tool is critical in assembling a grid, as the manner in which elements are interconnected will influence the amount of numerical error introduced throughout a simulation. Some common rules which should be followed include the following: 1) ensure that the grid spacing abides by the Courant number [$(\Delta t\sqrt{gH}) / (\Delta x) \leq 1$], 2) there should be at least 40 nodes per wavelength of interest, 3) the number of elements surrounding one node should be less than eight, 4) the skewness (maximum length of any side of an element divided by the equivalent diameter) should be kept as small as possible, and 5) there should be an even transition between larger and smaller elements. In addition, elements which will be undergoing inundation need to be much smaller (than wet elements) in order to facilitate a better representation of the wetting and drying process.

Using these criteria, three different grids for tsunami simulations were utilized at various times throughout the duration of this study. Grid 1 is displayed in Figure A5a and extends from the Aleutian Islands to central California. An enhanced zoom of Grid 1 around Newport is shown in Figure A5b. Grid 2 is displayed in Figure A6a and extends between northern Washington and northern California. A similar zoom of Newport for Grid 2 is shown in Figure A6b. Both Grid 1 and Grid 2 have the same level of refinement in the Newport region. Grid 2, however, has more refinement along the rest of the coast, as may be seen by close examination of the coastline to the north and to the south of the Newport vicinity. Grid 3 was used solely for simulations of the 1964 Alaska tsunami and the tidal influence at the time. Grid 3 is coarser than the first two grids in the Newport area, and essentially equivalent to Grid 1 for the rest of the domain.

Bathymetry and topography were interpolated onto the finite element grids. The sources of these databases include NOAA/NOS hydrographic surveys, digitized NOAA charts, local bathymetric surveys (Goldfinger, 1996), USGS topographic data, and digital elevation models.

Validation of the Model

The primary sources of error in the modeling process are derived from estimations of the seismic source, the ability of the numerical model to reproduce the propagation and inundation of the waves, and selection of numerical parameters used by the model. Controlling the uncertainties associated with the seismic source were discussed in the deformation section, and focus will now be given to evaluating the model's ability to simulate wave propagation and inundation and the errors associated with parameter selection.

In order to validate whether the model is properly simulating the wave propagation and inundation, one must be sure that the forcings which initially create the waves are correct. This is not a trivial task with tsunamis due to potential errors in the estimation of the ocean floor deformation that cannot be verified. One solution is to evaluate how well the model is able to simulate another type of long wave for which the forcings are known in great detail: tides.

A regional tide model was developed for the eastern north Pacific Ocean, the results of which can be used to verify the model's ability to reproduce observations at selected tide gauges. The finite element model used to simulate tides, TIDE2D (Walters, 1987) is formulated in the frequency domain. Inverse theory is used to determine boundary forcings along the open ocean boundary for the tidal constituents of interest. The inverse tidal method (ITM), developed by Nunez (1990), uses a least-squares fitting algorithm to match TIDE2D simulation results to tide gauge observations. Tidal elevations were compared between model and tide gauge observation over a period of one year at the 12 tide gauges shown in Figure A8. Root mean square (RMS) differences between the two were computed and plotted in Figure A9. ENPOM (Eastern North Pacific Ocean Model) represents the RMS between this regional tide model and the tide gauge observations. The other bars in the graph (ME-SCHW, RSC94, CSR3.0, TPX0.2, and FES95.2) represent RMS differences between various global tide models (available on CD from the Jet Propulsion Laboratory Physical Oceanography Distributed Active Archive Center) and tide gauge observations. Differences between the regional tide model (ENPOM) and observations compare favorably with the other global tide models, and errors are generally constrained to within 10 centimeters. Results from this tide model have been successfully used as a boundary forcing in more local tide modeling studies using ADCIRC. Figure A10 displays some results from a Columbia River tide modeling study (Das and Baptista, 1997) using forcings from the tide model. The results from Figures A9 and A10 exemplify that the models are propagating these long waves properly and accurately.

With the model verified for tides, the next step is to validate the model's ability to reproduce tsunami events for which tide gauge and runup observations are available. For the Oregon coast, the 1964 Alaska tsunami represents the best documented event in terms of available data. Using the estimated deformation to the ocean floor from Holdahl and Sauber (1994) mentioned earlier, ADCIRC was used to propagate the waves on Grid 3 for 18 hours after the earthquake. Tides were also incorporated into this simulation by formulating a boundary condition which would permit the tsunami waves to exit the open ocean boundary undisturbed yet still allow the tidal forcing to be enforced along the same open ocean boundary. A comparison between the model results and the tide gauge observation

at Yakutat, Alaska is displayed in Figure A11. The arrival time, amplitude, and wavelengths of the first couple of waves are reasonably reproduced. Later waves do not appear to be as well reproduced. Figure A12 shows the maximum wave elevations observed in the numerical simulation of the 1964 tsunami along the Oregon, Washington, and California coasts. These elevations include the influence of tides. Three regions have larger modeled wave heights than others: 1) from Gray's Harbor to Seaside, Oregon, 2) central Oregon, near Yaquina and Alsea bays, and 3) northern California, particularly near Crescent City. The increased energy near Crescent City is encouraging from a modeling perspective, as Crescent City was observed to be a focus of much of the transoceanic energy from this event. The modeled coastal runup along the west coast of the continental United States appears to be smaller than observed values documented by NOAA (Lander et. al. 1993, Lander and Lockridge 1989) and local observations (Horning, 1997).

Finally, modeling studies of recent tsunamis in other parts of the world have helped to evaluate the robustness of the state-of-the-art in numerical modeling of tsunamis. Myers and Baptista (1997) have shown the importance of numerical parameters such as the GWCE weighting factor, the time step, and the spatial refinement of the finite element grid near the coastline. Such parameters can greatly influence the solutions in the numerical model and, when carefully monitored, can provide results which reasonably reproduce the amplitudes and phases of waves as they reach the coastline.

Regional Modeling Results

Before examining the modeling results in the Newport area, it is insightful to first review what is occurring in the model at a regional scale. It should first be mentioned that the Cascadia simulations do not include the influence of tides, although research is currently being performed to evaluate tide and tsunami interactions during Cascadia events. The results shown here, rather, were generated assuming that mean higher high water (MHHW) exists throughout the duration of the simulation. MHHW is assumed for safety purposes, because it is instructive to evaluate the impact of the tsunami at maximum water levels.

Seven different simulations are presented, each of which uses a different source scenario for the initial conditions (1A, 1C, 2A, 2B, 2C, 2CN, and 2CS). 1B is not simulated because comparisons of 2B to 2A and 2C are sufficient to infer results from 1A and 1C simulations. In order to differentiate between these seven simulations, it is useful to evaluate the maximum coastal wave heights that are generated over the duration of each simulation. Figure A13 shows these maximum coastal wave elevations for the seven simulations that were made on Grid 1, as well as two (1A and 1C) which were also simulated using Grid 2. Recall that Grid 1 and Grid 2 essentially have the same refinement in Newport and Seaside, but Grid 2 has more refinement along the rest of the Oregon, Washington, and northern California coastlines. Scenario 1A generally has larger wave heights than 2A, and similarly 1C has larger wave heights than 2C. Because the seaward transition zone becomes very narrow starting from north central Oregon to northern California, 1A and 1C give very similar results in those regions. Above north central Oregon, 1C shows higher coastal wave elevations than 1A. Scenarios 2CS, and 2CN yield values which are about one half the values of the other scenarios, owing to about half as much deformation.

Use of Grid 2 significantly increases the coastal wave elevations for the two scenarios simulated on this grid, 1A and 1C. 1C on Grid 2 showed much larger values than 1C on Grid 1, particularly in the north and south portions of the domain. The increased values appear to be the result of the greater refinement, both along the coastline and further out in the ocean, in Grid 2. This is an important result, as it provides a standard for what levels of grid refinement need to be used in studies such as this. Too little refinement can significantly dampen the resulting waves. The grids used here are approaching 100,000 nodes, with levels of refinement at Newport and Seaside approaching 5 meters. This was not feasible on the computers of a couple years ago and is currently pushing the limits of today's state-of-the-art computers.

Bathymetry is also an important factor which influences which coastal regions will be susceptible to higher energy waves. Shallow banks and canyons can focus the energy of waves towards certain regions. The effect of bathymetry on wave elevations is exemplified in Figures A14a-g which show isolines of maximum elevation for each of the seven scenarios. Numbers were not placed on the isolines (the same isolines were used for each figure), because it is the patterns of the isolines which instead yield insight into the bathymetric focusing mechanisms affecting the wave propagation. In each of these cases (except 2CN), the isolines show that higher wave elevations occur over offshore banks on the shelf off Yaquina and Alsea Bays. These patterns of isolines at this latitude are associated with a shallow bank along the continental shelf which is acting to "bend" the wave train inward towards Newport and Alsea Bay. The canyons off the coast of the Columbia River, Willapa Bay, and Gray's Harbor can also act to change the propagation of the initial wave train.

The location of the deformation front for each scenario can also be seen in Figures A14a-g by the concentration of isolines further out in the ocean which run parallel to the coastline. The deformation generally occurs further out in the ocean in the northern portions of the domain. Thus, the initial waveforms in the north have more of a chance to amplify as they head towards the coast, although it will take those waves longer to reach the coast than in the south.

Local Modeling Results

While regional features can influence the spatial variability of the tsunami impact, local features will likewise play a significant role in determining the fate of the waves as they reach land. Figures A15a-g show the maximum velocity vectors throughout each simulation. The dark line in each of these figures is the coastline, so any velocity vectors which are located inside the coastline represent points which were inundated by the modeled tsunamis. Figures A15a and A15b (1A and 1C, respectively) show the most inundation and generally have fairly uniform maximum velocity vectors in the same areas (i.e. zooms of the various portions of the bay show vectors which are generally pointing in the same direction). The inundation for 1A and 1C comes from two primary points: 1) a narrow valley in the southern end of the South Beach State Park, and 2) from the Yaquina Bay channel into the north end of the South Beach State Park. Figures A15c and A15g (2A and 2CS, respectively) have more scatter among maximum velocity vectors in the same regions. Interestingly, these two simulations differ from the others in that no diffusion was

utilized in the model simulation. The other simulations had a small amount of diffusion added to the solution. Maximum velocity vectors in the mouth of the Yaquina Bay channel tend to occur with waves exiting the domain, whereas maximum velocity vectors for the rest of the bay tend to occur as water is moving towards the interior of the bay for each of the simulations. The magnitude of the velocity vectors throughout the bay is also significant: on the order of 10 meters per second.

The inundation mapping of the Newport area also incorporated into the modeling results factors to represent the subsidence of the land caused by the earthquake and the difference between mean sea level and mean lower low water. With these additions, the maps show more potential inundation in other parts of Newport such as near the Hatfield Marine Science Center.

Figures A17a and A17b show elevation and velocity magnitude time histories, respectively, for the four station locations displayed in Figure A16. Notice first that the elevations are damped as they move into the interior of the bay. Depending upon the geometry of a particular bay, it is possible for the wave to amplify inside a bay, but not in this case. The 1A and 1C waves are generally 1-2 meters larger than the other modeled waves. Part of this is probably due to the source defined for these scenarios, but part is possibly also due to the fact that these two waves are arriving in Newport with a leading depression wave rather than an initial rise in water. Tadepalli and Synolakis (1994) have shown that leading depression waves lead to higher runup values than leading elevation waves. Figure A17a also shows a large wave which arrives approximately two hours after the earthquake and which is similar in magnitude to the initial wave arriving in Newport.

Conclusions

Communities such as Newport, Oregon face the task of designing hazard mitigation plans for tsunamis, either locally generated by the Cascadia subduction zone or generated from other parts of the Pacific Ocean such as the 1964 Alaska tsunami. Modeling past tsunami events under the constraints of current geologic and geophysical data (when applicable) provides the best indicator as to what could potentially occur in future tsunami events. The seismic source scenarios used in this study were based upon a careful selection of deformation modeling techniques and utilization of geophysical, geologic, and thermal information in an effort to minimize uncertainties associated with the initial conditions to the hydrodynamic model.

Likewise, the hydrodynamic model was held under the microscope of model validation to ensure that the physical mechanisms affecting wave behavior in the model were well represented. Modeling of tides showed that these long waves were properly propagated by the numerical models, and a simulation of the 1964 Alaska tsunami showed promising signs as to the model's ability to reproduce this more recent event.

Simulations of potential Cascadia tsunamis, using the initial conditions from the deformation scenarios, were evaluated from both regional and local perspectives. From a regional

vantage, bathymetric focusing mechanisms are present throughout the domain which will affect the eventual wave train reaching the coast. One of the prominent focusing mechanisms is the Hecate Bank off the coast of central Oregon, which will act to focus the energy of the waves toward the Yaquina Bay and Alsea Bay regions. Deformation occurring in deeper waters will allow the generated waves more of an opportunity to increase in amplitude as they head toward the coast, although it will take more time to reach the coast.

The amount of refinement in the grid was shown to have pronounced effects on the ultimate wave elevations seen along the coastline. This exemplifies the importance of monitoring and validating the numerical model and associated numerical parameters.

From a more local perspective, inundation in the Newport area from potential Cascadia tsunamis appeared to be occurring primarily at the northern and southern ends of South Beach State Park for the more extreme events. The large velocities seen through the Yaquina Bay channel stress the importance of incorporating the kinetic energy of the wave into hazard mitigation planning. Elevations through the mouth of the channel were modeled to be approximately within 4-6 meters, with damping of the elevations occurring as the wave headed toward the interior of the bay.

The incentive for a modeling study as presented here is derived from two roots: 1) there is an enormous amount of scientific understanding which can be gained from evaluating the physical mechanisms represented in a numerical model, and 2) there is a critical need to have adequate mitigation plans in place in the event of future tsunamis impacting the Newport community. These two roots have a lot of common ground as exemplified by the inundation maps which are constructed for Oregon coastal communities such as Newport. That common ground should not be extended for anything other than the intended purposes of such a modeling study: to provide a scientific tool which may assist hazard mitigation planning and community awareness.

References

Atwater, B.F., Nelson, A.R., Clague, J.J., Carver, G.A., Yamaguchi, D.K., Bobrowsky, P.T., Bourgeois, J., Darienzo, M.E., Grant, W.C., Hemphill-Haley, E., Kelsey, H.M., Jacoby, G.C., Nishenko, S.P., Palmer, S.P., Peterson, C.D., and Reinhart, M.A., 1995, Summary of Coastal Geologic Evidence for Past Great Earthquakes at the Cascadia Subduction Zone, *Earthquake Spectra*, 11(1).

Committee on the Alaska Earthquake of the Division of Earth Sciences National Research Council, 1972, *The Great Alaska Earthquake of 1964, Oceanography and Coastal Engineering*, National Academy of Sciences, Washington, D.C.

Das, S. and Baptista, A.M., 1997, personal communication.

Flück, P. and Wang, K., 1996, (in preparation).

Fukao, Y., Tsunami Earthquakes and Subduction Processes Near Deep-Sea Trenches, *Journal of Geophysical Research*, 1979, 84, 2303-2314.

Geist, E. and Yoshioka, S., 1996, Source Parameters Controlling the Generation and Propagation of Potential Local Tsunamis Along the Cascadia Margin, *Natural Hazards*, 13, 151-177.

Goldfinger, C., 1996, personal communication.

Hebenstreit, G.T. and Murty, T.S., 1989, Tsunami Amplitudes from Local Earthquakes in the Pacific Northwest Region of North America Part 1: The Outer Coast, *Marine Geodesy*, 13, 101-146.

Holdahl, S.R. and J. Sauber, 1994, Coseismic Slip in the 1964 Prince William Sound Earthquake: A New Geodetic Inversion, *Pure and Applied Geophysics*, 142(1), 55-82.

Horning, T., 1997, personal communication.

Hyndman and Wang, 1993, Thermal Constraints on the Zone of Major Thrust Earthquake Failure: The Cascadia Subduction Zone, *Journal of Geophysical Research*, 98(B2), 2039-2060.

Hyndman and Wang, 1995, The Rupture Zone of Cascadia Great Earthquakes from Current Deformation and the Thermal Regime, *Journal of Geophysical Research*, 100(B11), 22133-22154.

Lander, J.L. and Lockridge, P.A., 1989, United States Tsunamis, National Geophysical Data Center, Publication 41-2.

Lander, J.L., Lockridge, P.A., and Kozuch, M.J., 1993, Tsunamis Affecting the West Coast of the United States, National Geophyical Data Center, Documentaion No. 29.

Luettich, R.A. and Westerink, J.J., 1995a, *An Assessment of Flooding and Drying Techniques for Use in the ADCIRC Hydrodynamic Model: Implementation and Performance in One-Dimensional Flows*, Dept. of the Army, U.S. Army Corps of Engineers, Vicksburg, MS.

Luettich, R.A. and Westerink, J.J., 1995b, *Implementation and Testing of Elemental Flooding and Drying in the ADCIRC Hydrodynamic Model*, Dept. of the Army, U.S. Army Corps of Engineers, Vicksburg, MS.

Luettich, R.A., Westerink, J.J., and Scheffner, N.W., 1991, *An Advanced Three-dimensional Circulation Model for Shelves, Coasts, and Estuaries*, Dept. of the Army, U.S. Army Corps of Engineers, Washington, D.C.

Mansinha, L. and Smylie, D.E., 1971, The Displacement Fields of Inclined Faults, *Bulletin of the Seismological Society of America*, 61(5), 1433-1440.

Myers, E.P. and Baptista, A.M., 1995, Finite Element Modeling of the July 12, 1993 Hokkaido Nansei-Oki Tsunami, *Pure and Applied Geophysics*, v. 144 (3/4), 769-801.

Myers, E.P. and Baptista, A.M., 1997, Enhanced Finite Element Modeling of the Hokkaido Nansei-Oki Tsunami: Comparison between Model and Observation, *Advances in Water Resources (in progress).*

Ng, M.K.-F., Leblond, P.H., and Murty, T.S., 1990, Simulation of Tsunamis from Great Earthquakes on the Cascadia Subduction Zone, *Science*, 250, 1248-1251.

Nunez, R. 1990, Prediction of Tidal Propagation and Circulation in Chilean Inland Seas Using a Frequency-Domain Mode, *Master of Science Thesis, Oregon State University.*

Okada, Y., Surface Deformation due to Shear and Tensile Faults in a Half-Space, *Bulletin of the Seismological Society of America*, 1985, 75(4), 1135-1154.

Priest, G.R., 1995, Explanation of Mapping Methods and Use of the Tsunami Hazard Maps of the Oregon Coast, State of Oregon, Department of Geology and Mineral Industries, Open-File Report O-95-67, 95 p.

Priest, G.R., Myers, E.P., Baptista, A.M., Fleuck, P., Wang, K., Goldfinger, C., 1997, Fault Dislocation Scenarios for a Tsunami Hazard Analysis of the Cascadia Subduction Zone.

Tadepalli, S. and Synolakis, C.E., 1994, The Run-up of N-waves on Sloping Beaches, *Proc. R. Soc. Lond. A*, 445, 99-112.

Turner, P.J. and Baptista, A.M., 1991, *ACE/Gredit Users Manual: Software for Semi-automatic Generation of Two-Dimensional Finite Element Grids,* CCALMR Software Report SDS2(91-2), Oregon Graduate Institute of Scienee & Teehnology, Portland, OR.

Walters, R., 1987, A Model for Tides and Currents in the English Channel and Southern North Sea, *Advances in Water Resources*, 10, 138-148.

Whitmore, P.M., 1993, Expected Tsunami Amplitudes and Currents Along the North American Coast for Cascadia Subduction Zone Earthquakes, *Natural Hazards*, 8, 59-73.

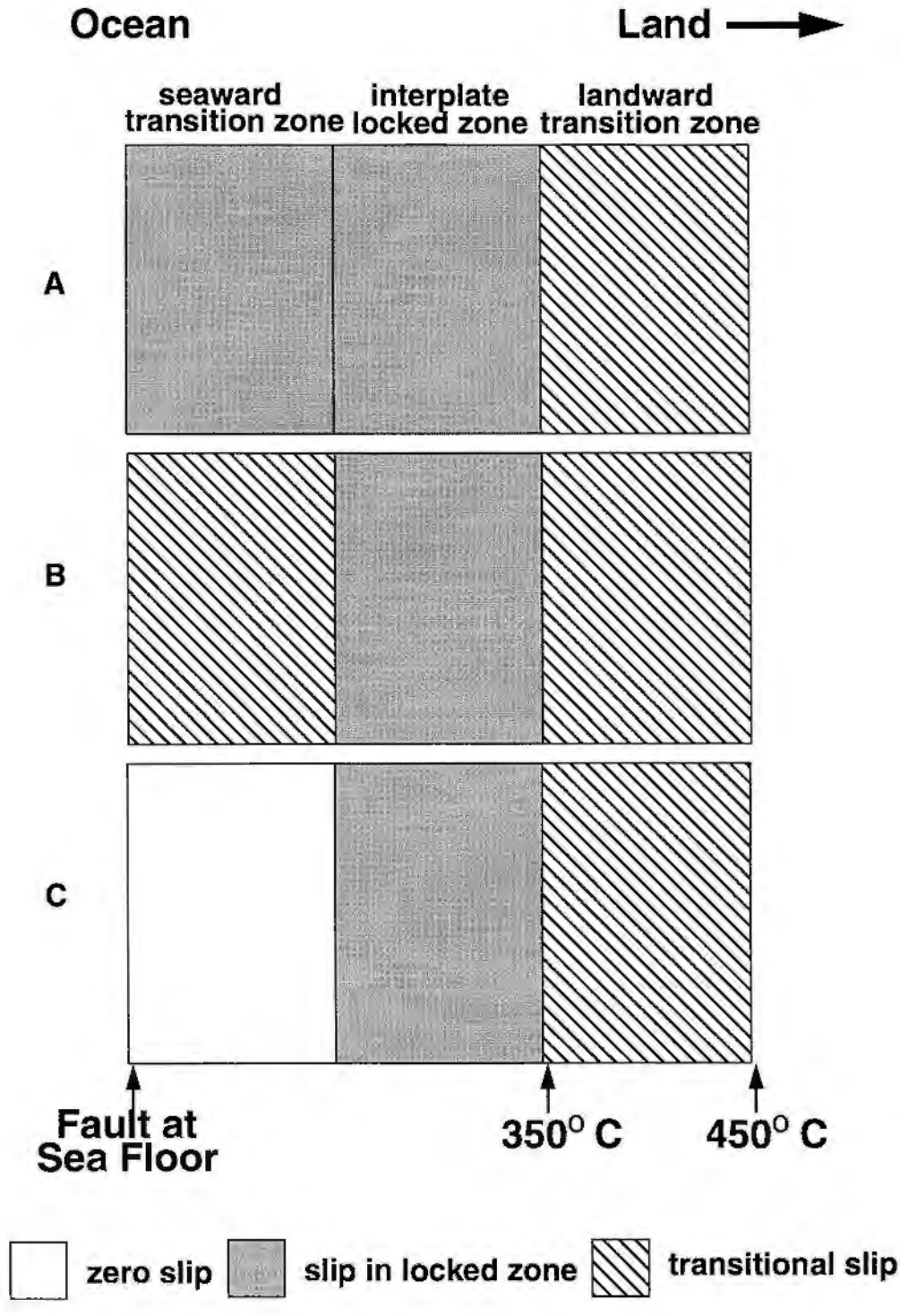

Figure A1 Distribution of slip for scenarios A, B, and C

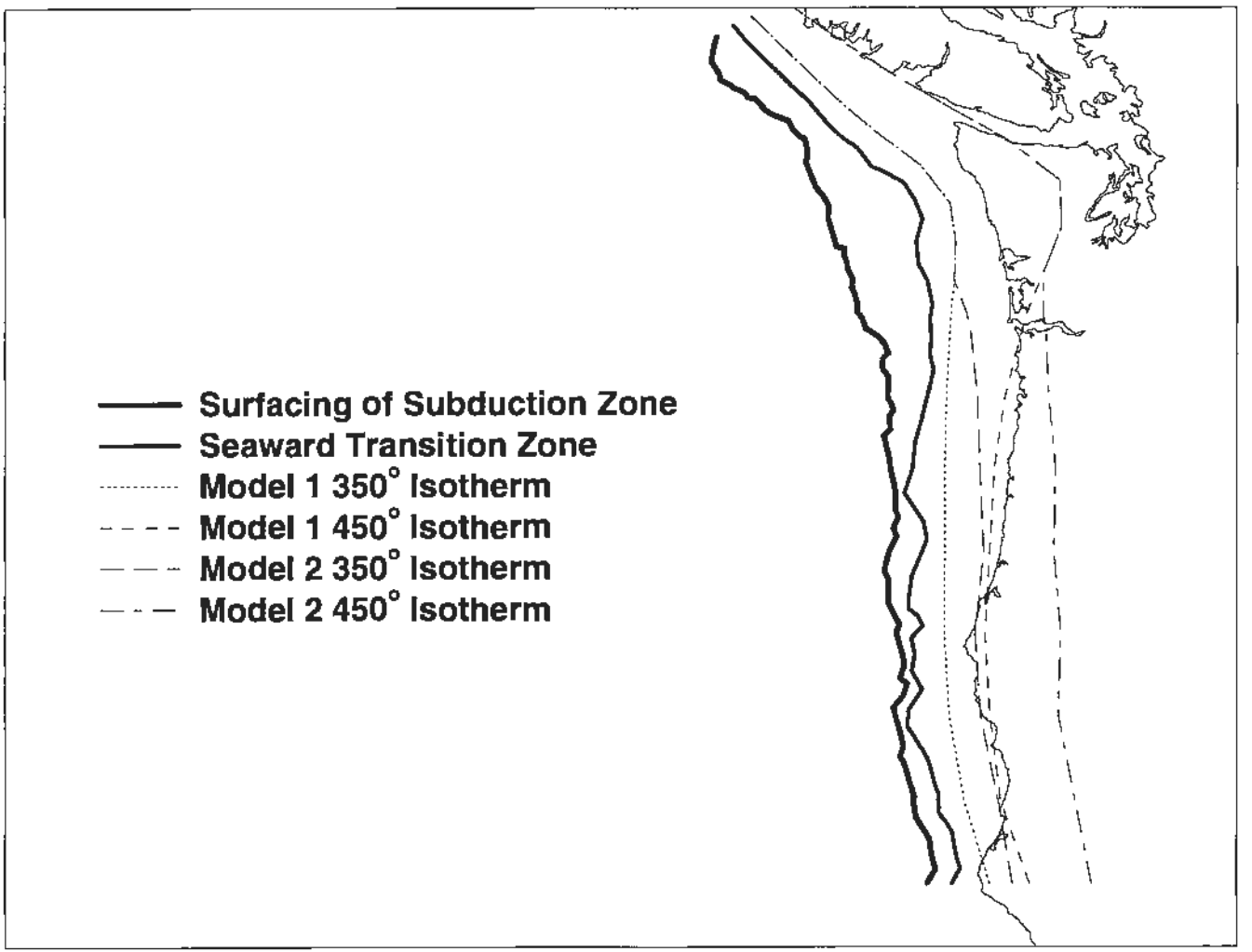

Figure A2 *Geologic boundaries for cases 1 and 2*

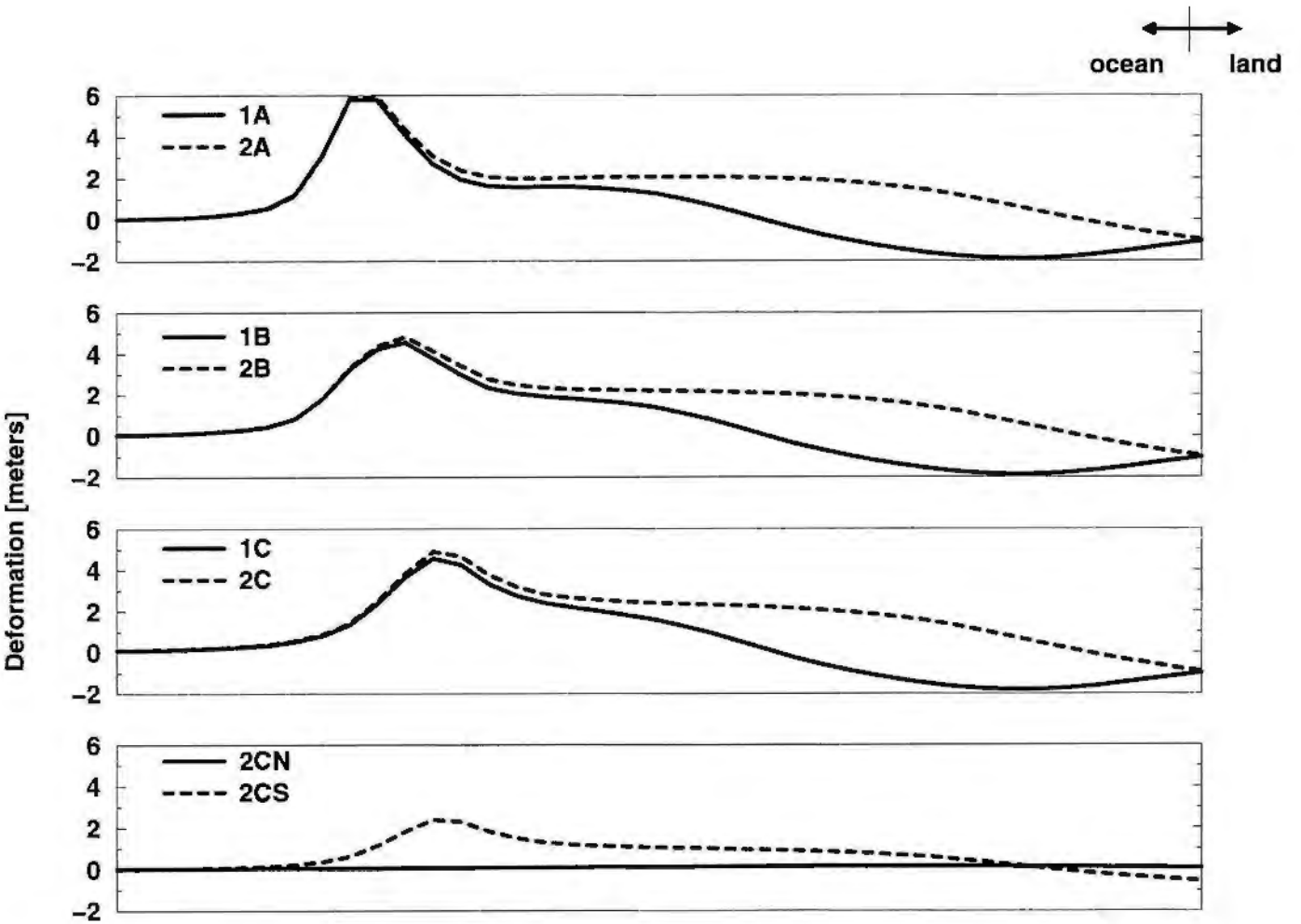

Figure A3 Deformations offshore of Newport, Oregon

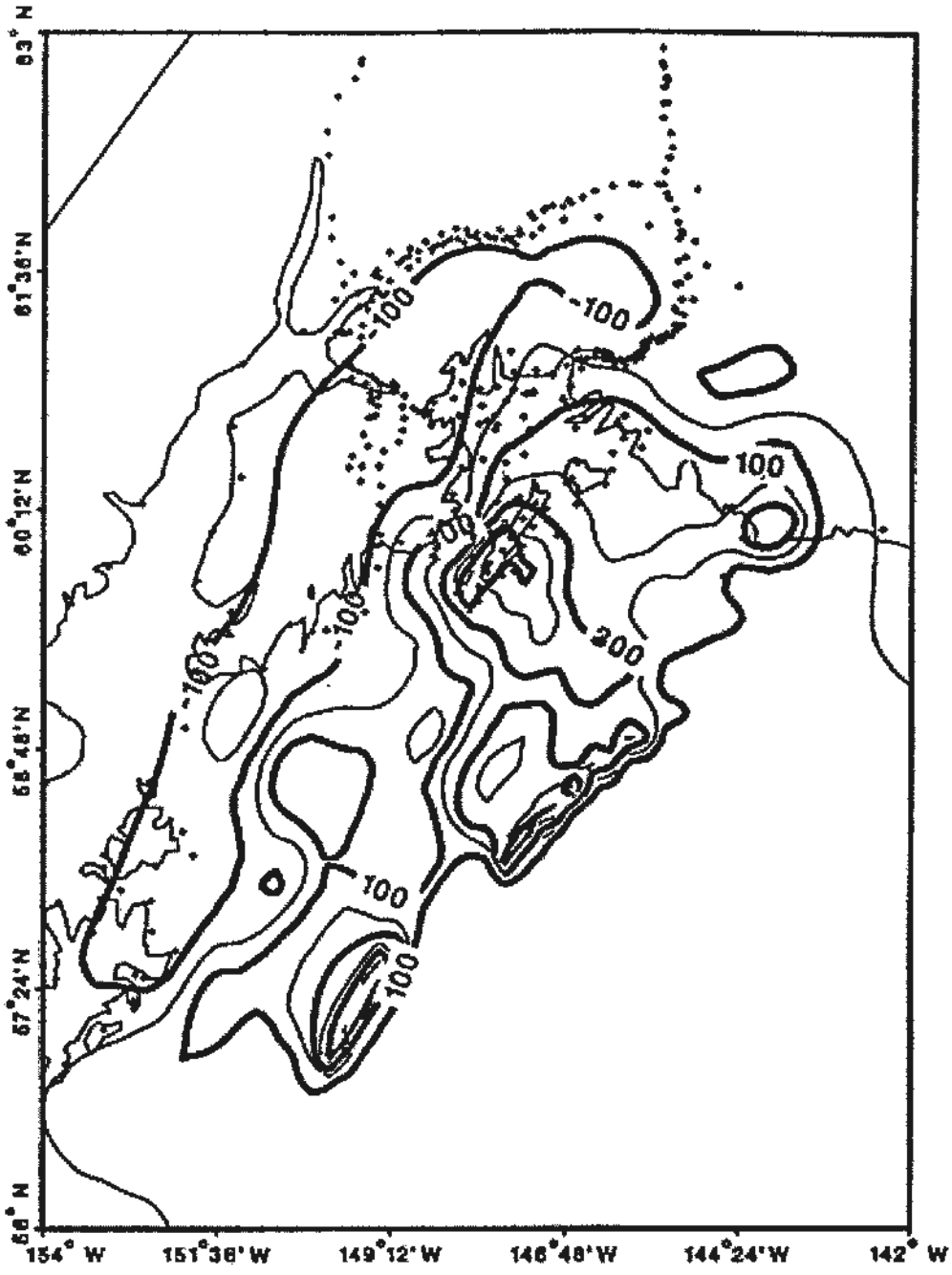

Figure A4 1964 Alaska deformation (extracted from Holdahl and Sauber, 1994)

Figure A5a Grid 1

Figure A5b Zoom of grid 1 at Newport

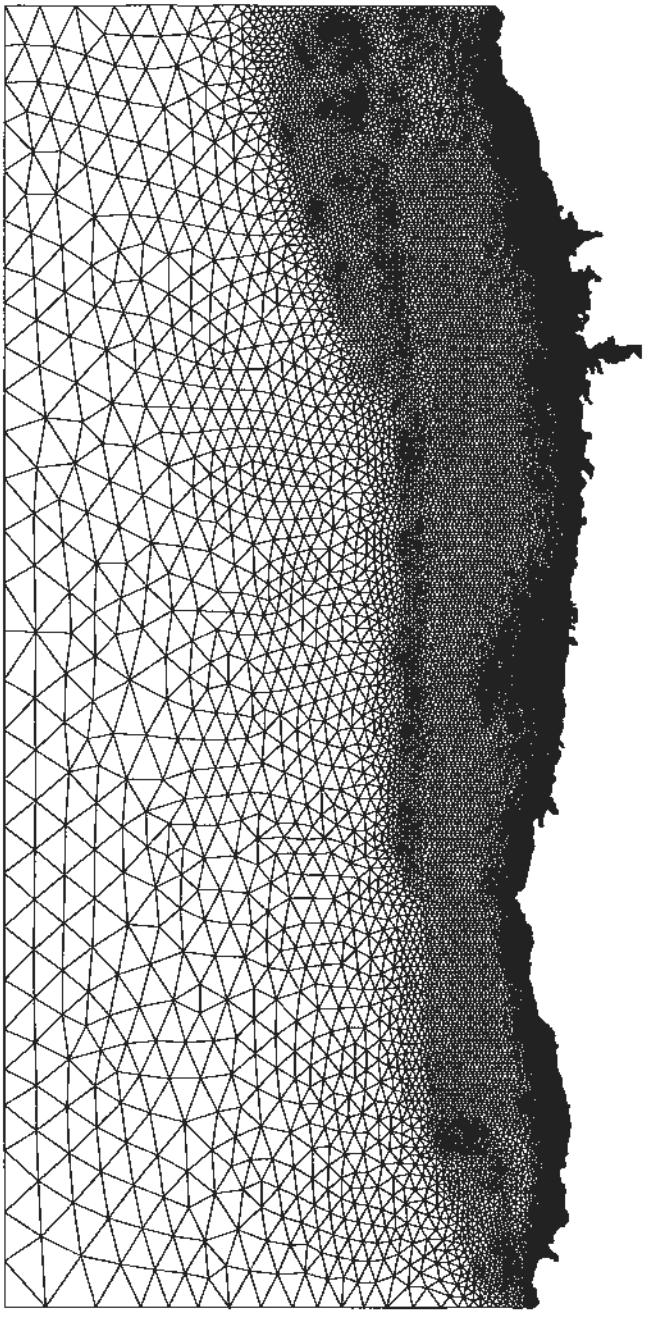

Figure A6a *Grid 2*

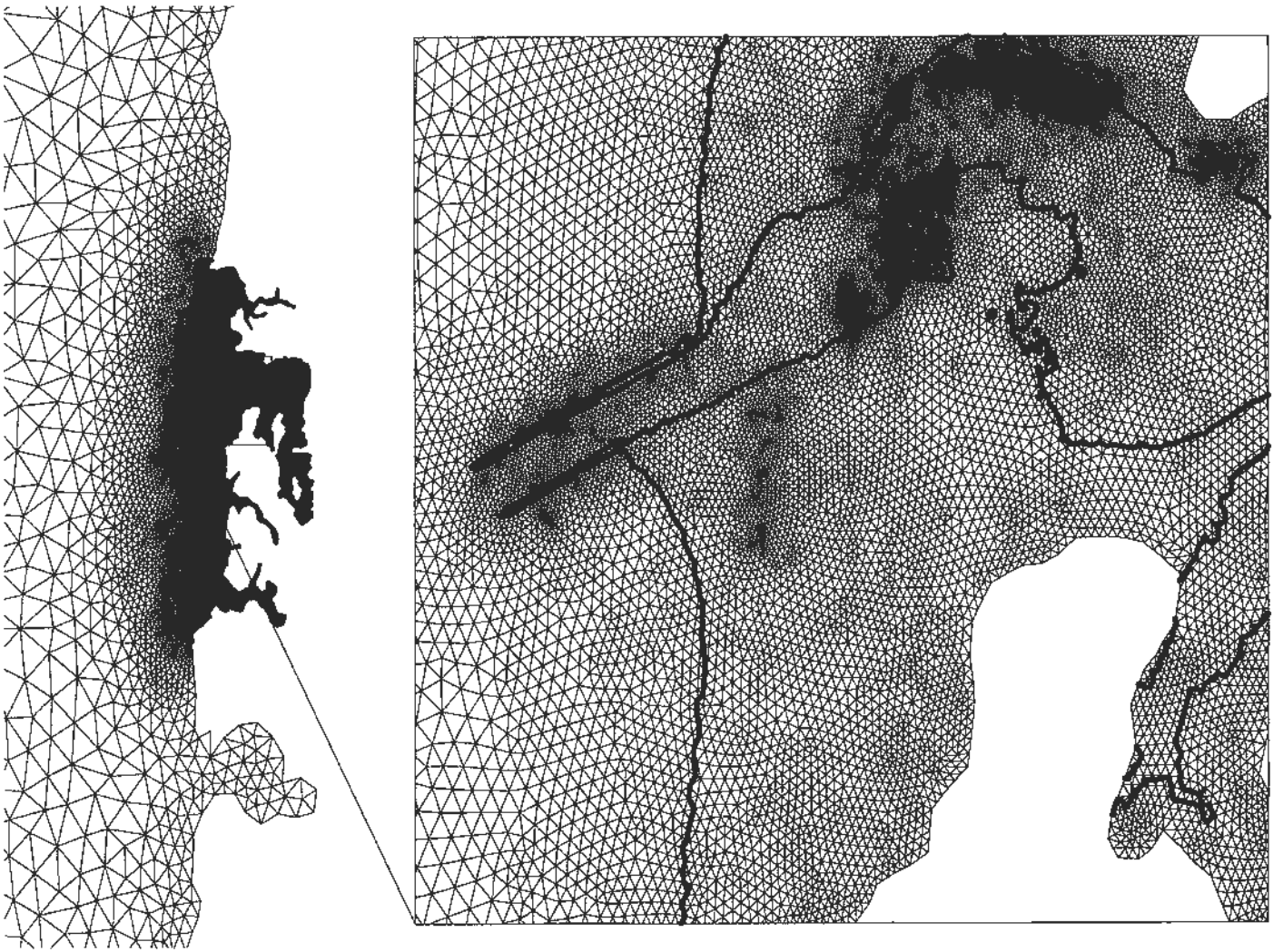

Figure A6b *Zoom of grid 2 at Newport*

Figure A7a Grid 3

***Figure A7b** Zoom of grid 3 at Newport*

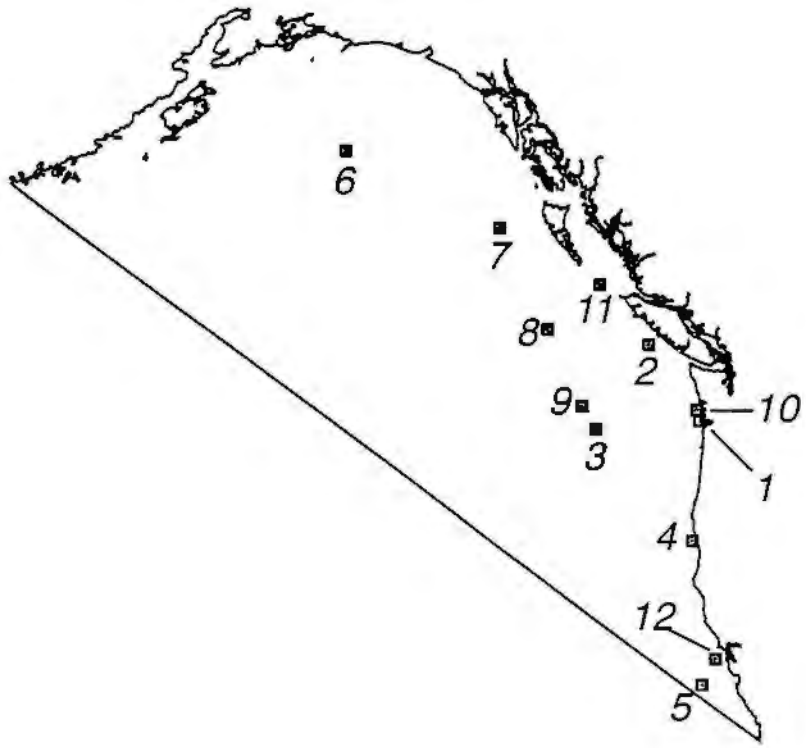

Figure A8 Selected tide gauge locations in the eastern north Pacific Ocean

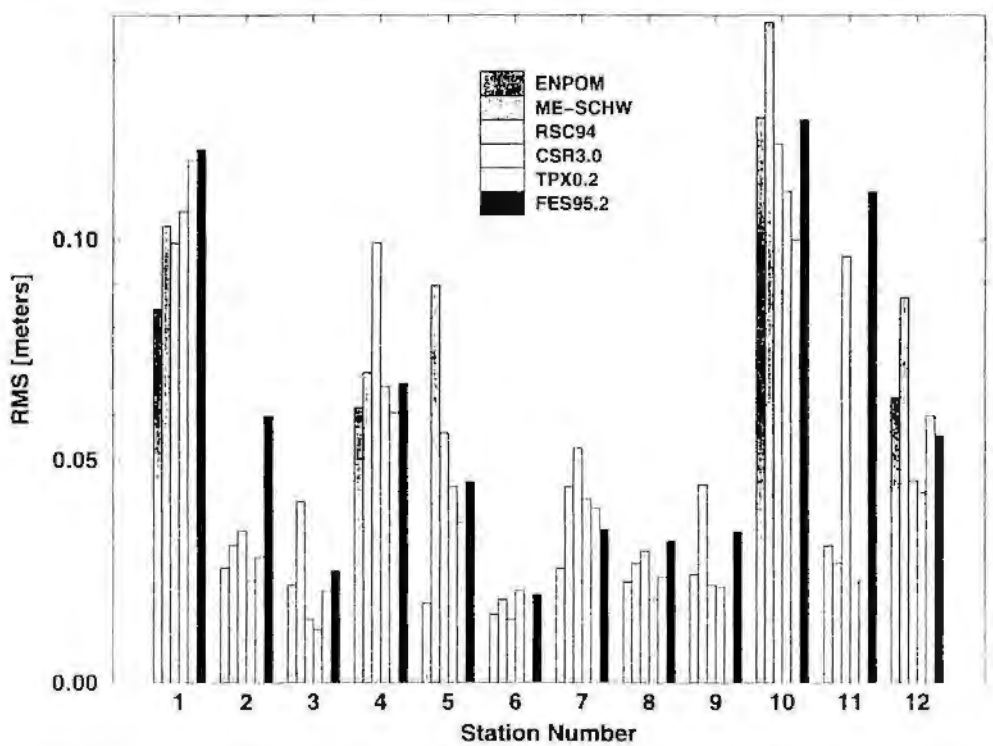

Figure A9 Root mean square errors in elevations at selected tide gauges

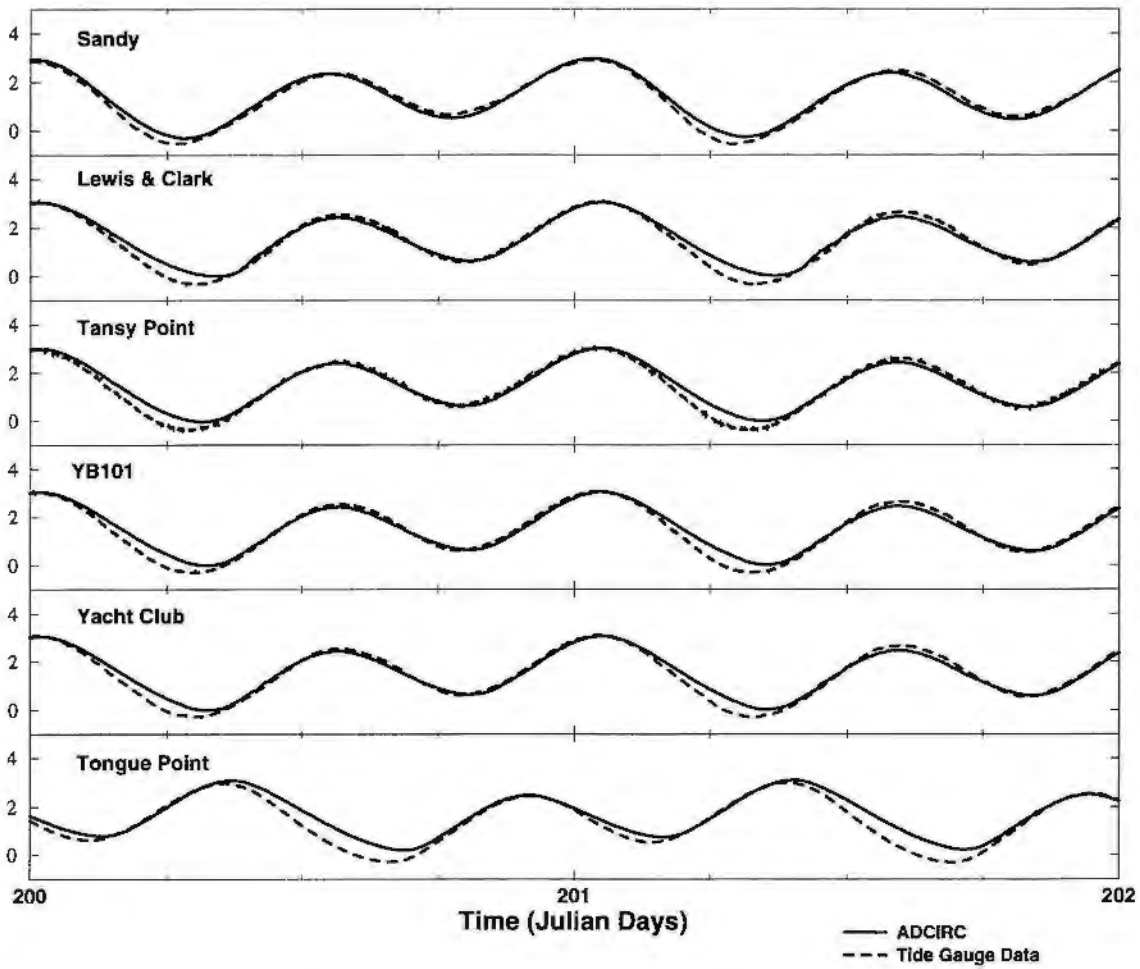

Figure A10 *Tide model and tide gauge comparisons in the Columbia River*

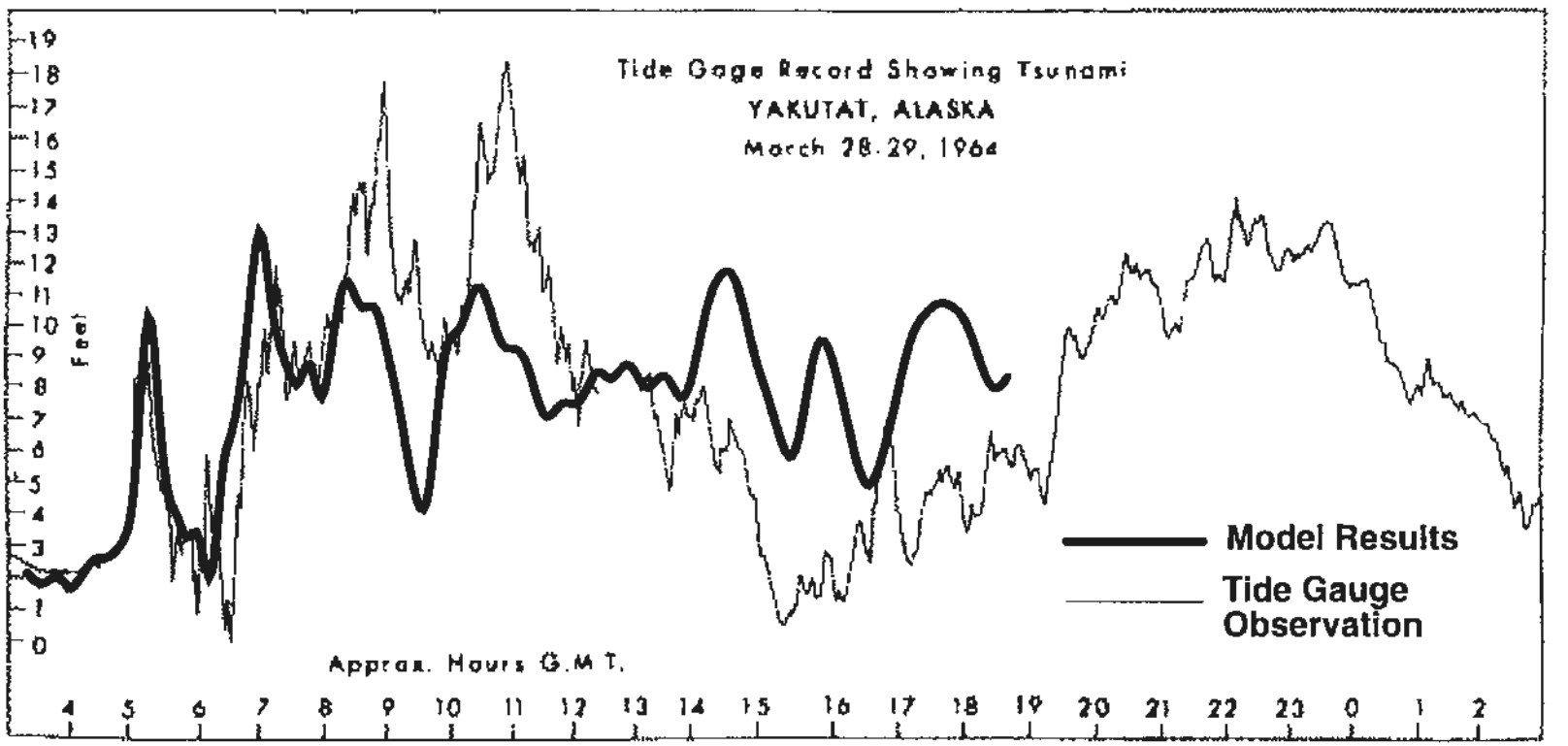

Figure A11 Numerical modeling results compared to tide gauge observation at Yakutat, AL for the 1964 Alaska tsunami (image of tide gauge observation extracted from Committee on the Alaska Earthquake of the Division of Earth Sciences National Research Council, 1972)

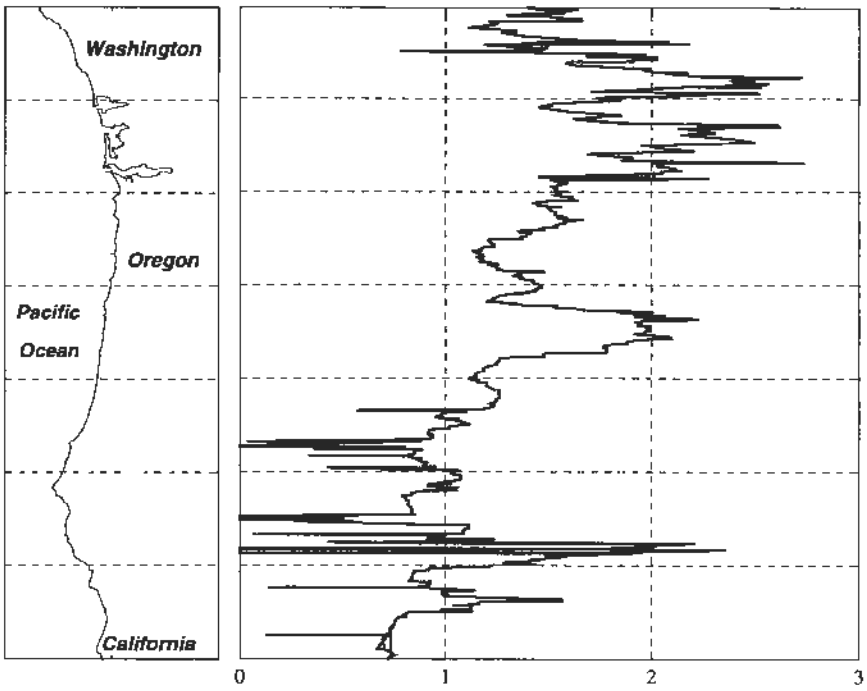

Figure A12 Maximum coastal wave heights for the 1964 Alaska tsunami simulation (tide included)

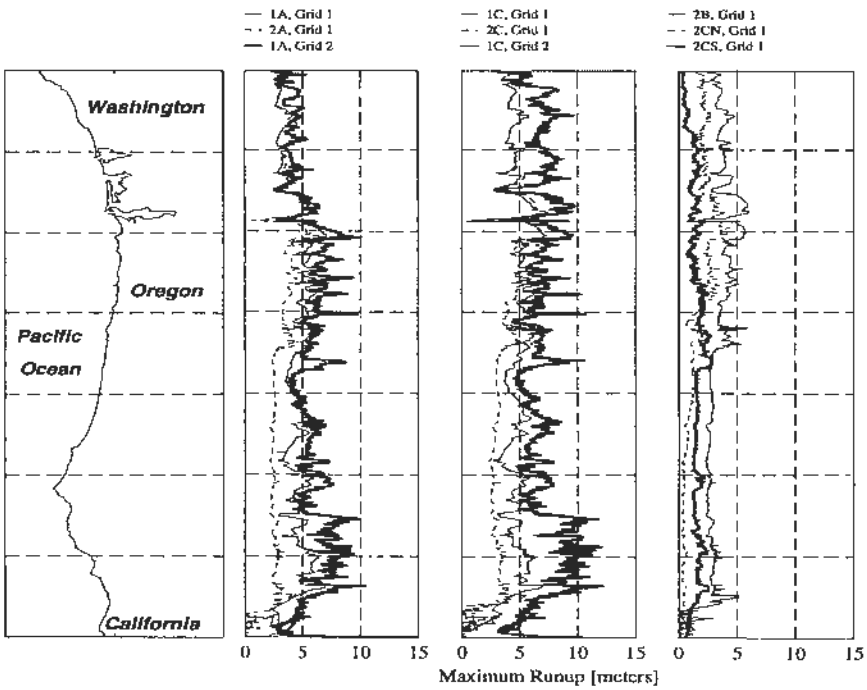

Figure A13 Maximum coastal wave heights for modeled cascadia tsunamis

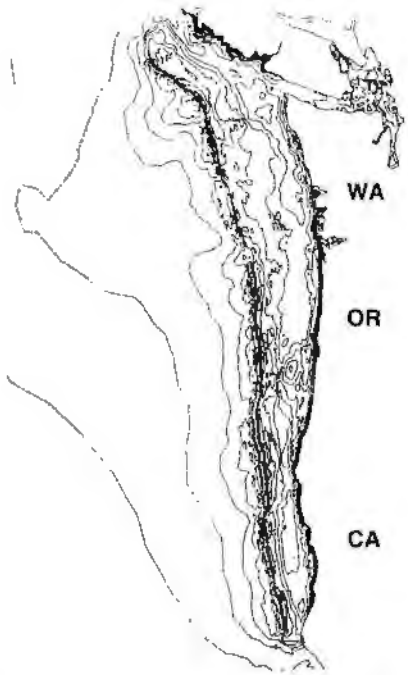

Figure A14a *Isolines of maximum elevation - model 1A*

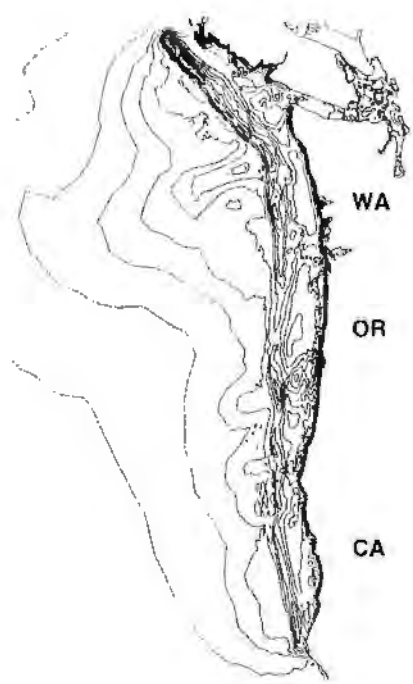

Figure A14b *Isolines of maximum elevation - model 1C*

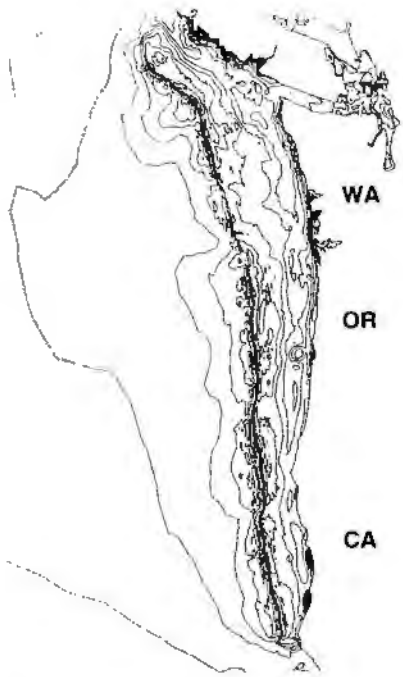

Figure A14c *Isolines of maximum elevation - model 2A*

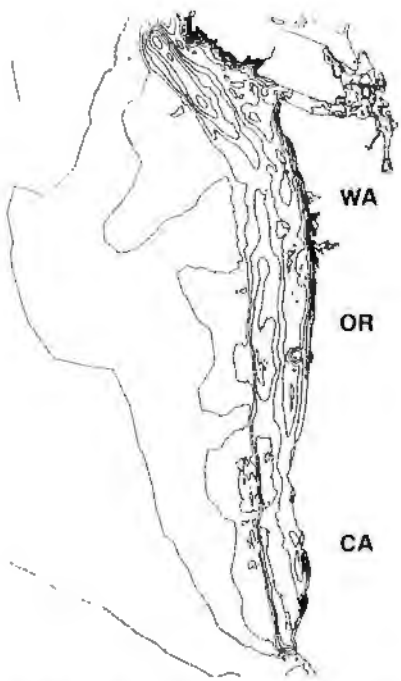

Figure A14d *Isolines of maximum elevation - model 2B*

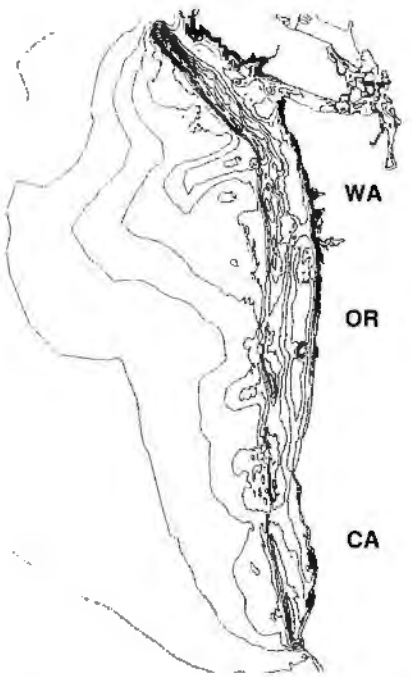

Figure A14e *Isolines of maximum elevation - model 2C*

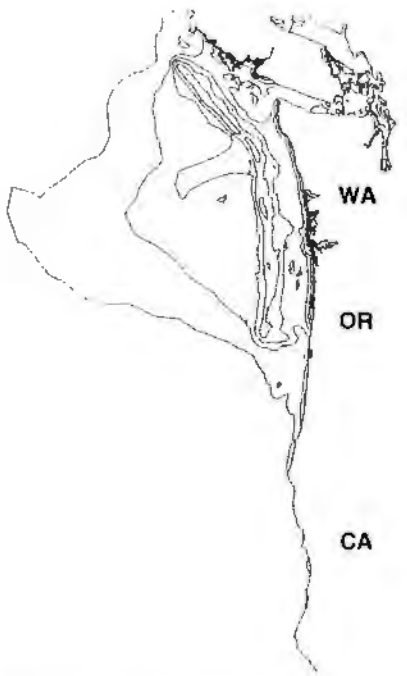

Figure A14f *Isolines of maximum elevation - model 2CN*

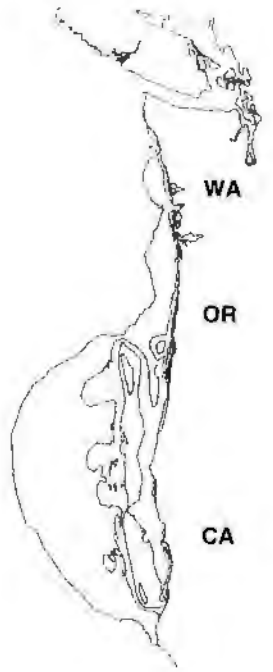

Figure A14g *Isolines of maximum elevation - model 2CS*

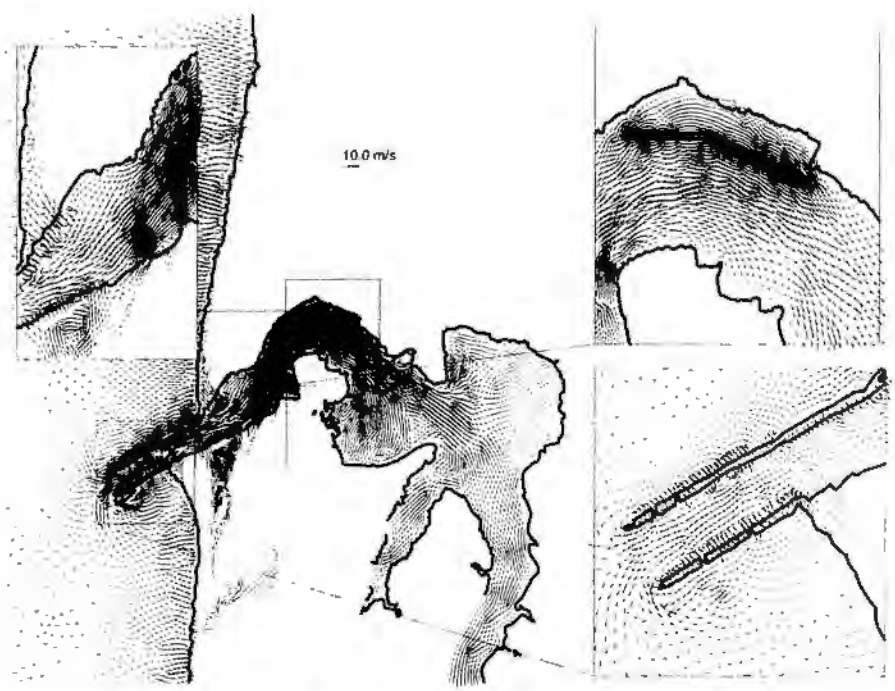

Figure A15a *Local Tsunami effects for model 1A in Yaquina Bay*

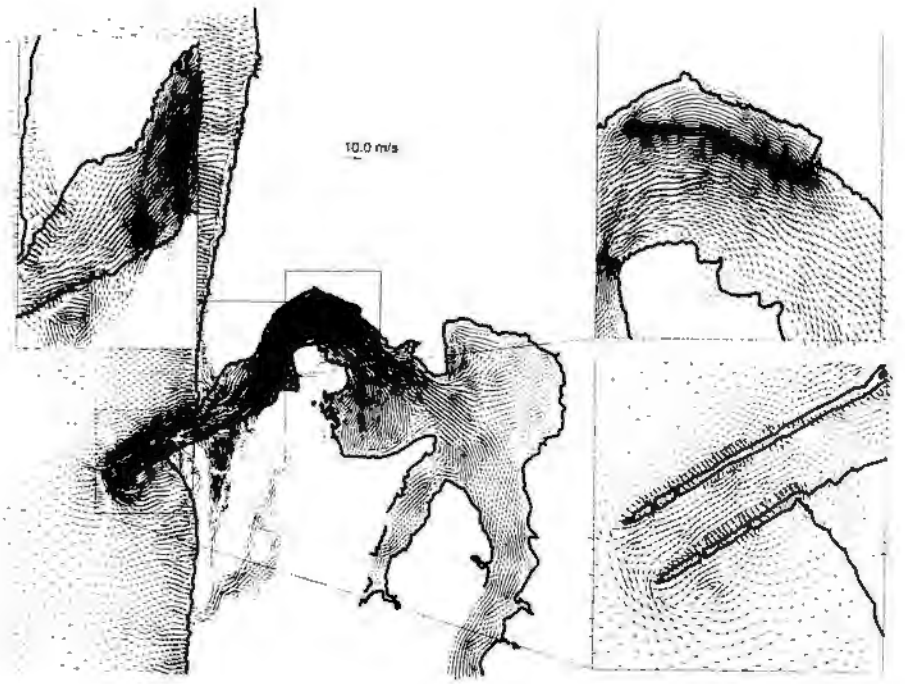

Figure A15b *Local Tsunami effects for model 1C in Yaquina Bay*

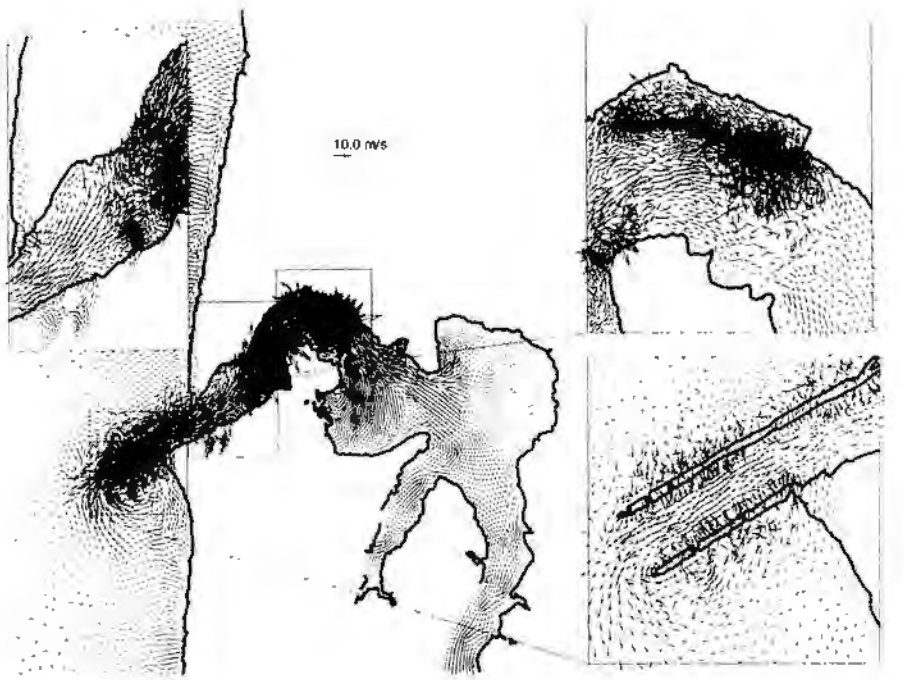

Figure A15c *Local Tsunami effects for model 2A in Yaquina Bay*

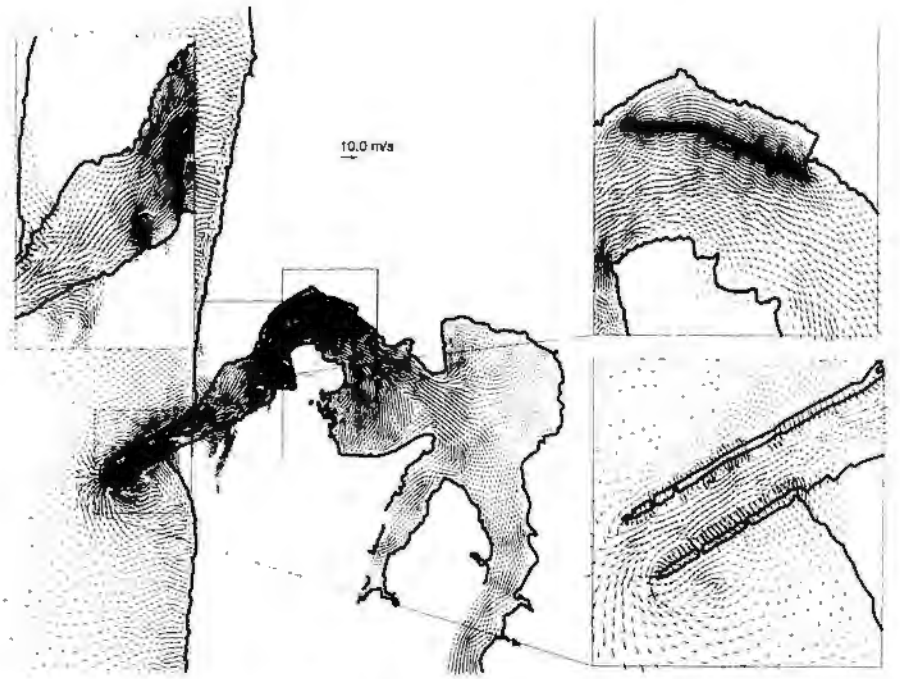

Figure A15d *Local Tsunami effects for model 2B in Yaquina Bay*

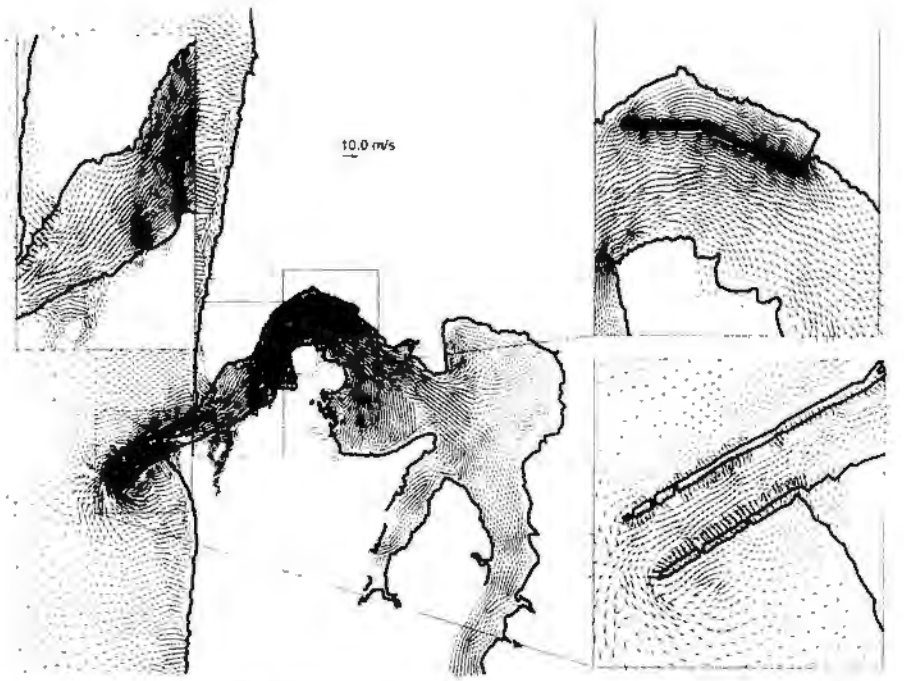

Figure A15e *Local Tsunami effects for model 2C in Yaquina Bay*

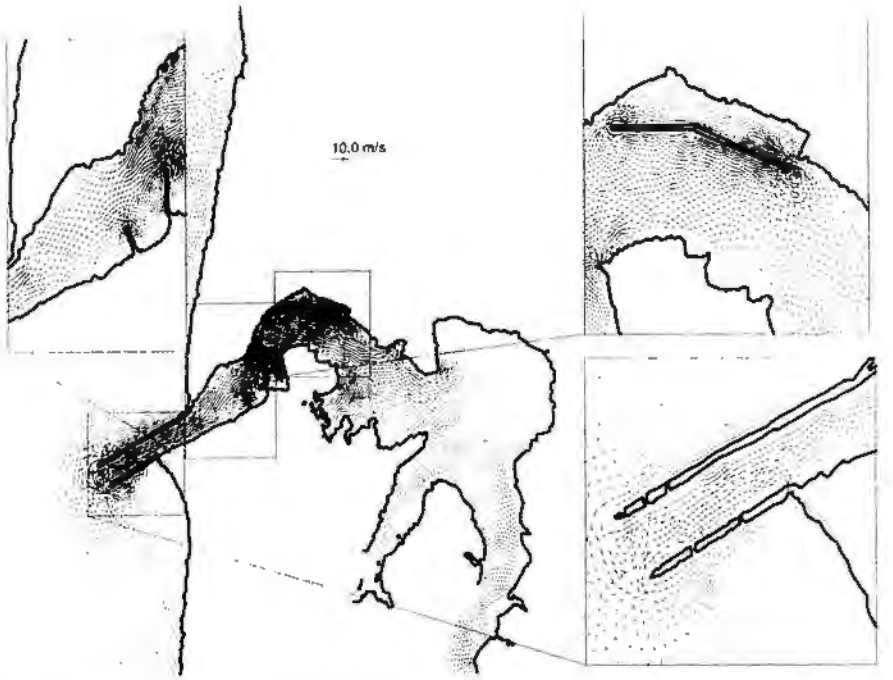

Figure A15f *Local Tsunami effects for model 2CN in Yaquina Bay*

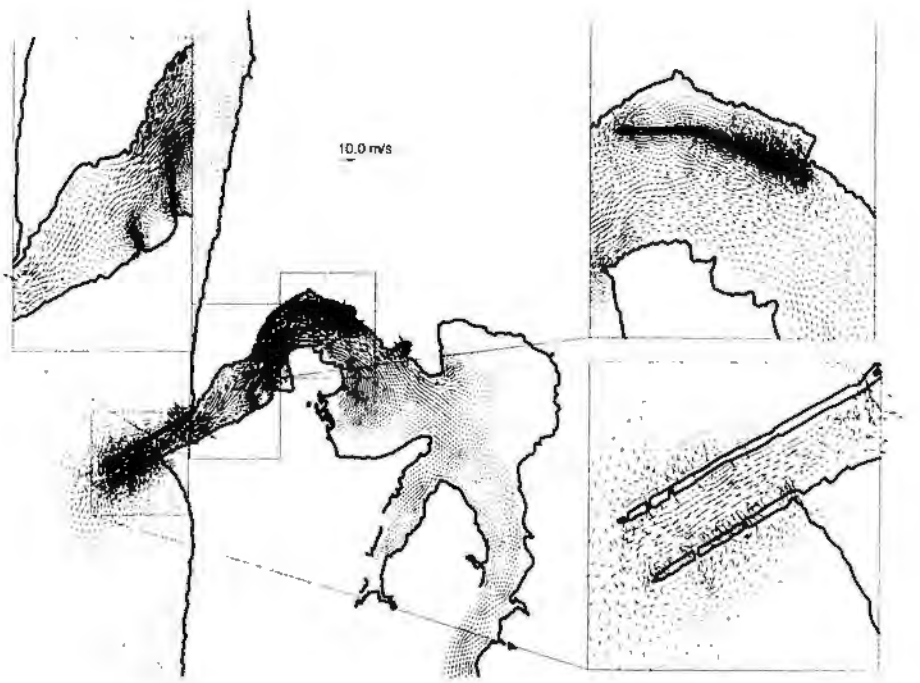

Figure A15g *Local Tsunami effects for model 2CS in Yaquina Bay*

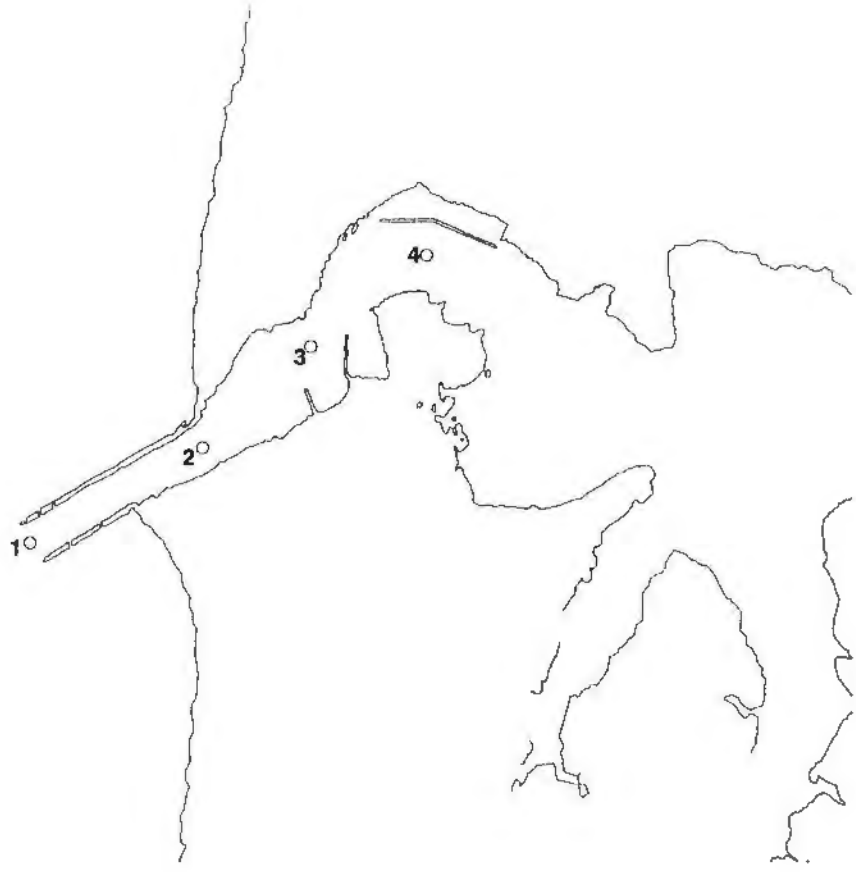

Figure A16 *Locations of Yaquina Bay stations for elevation and velocity time histories*

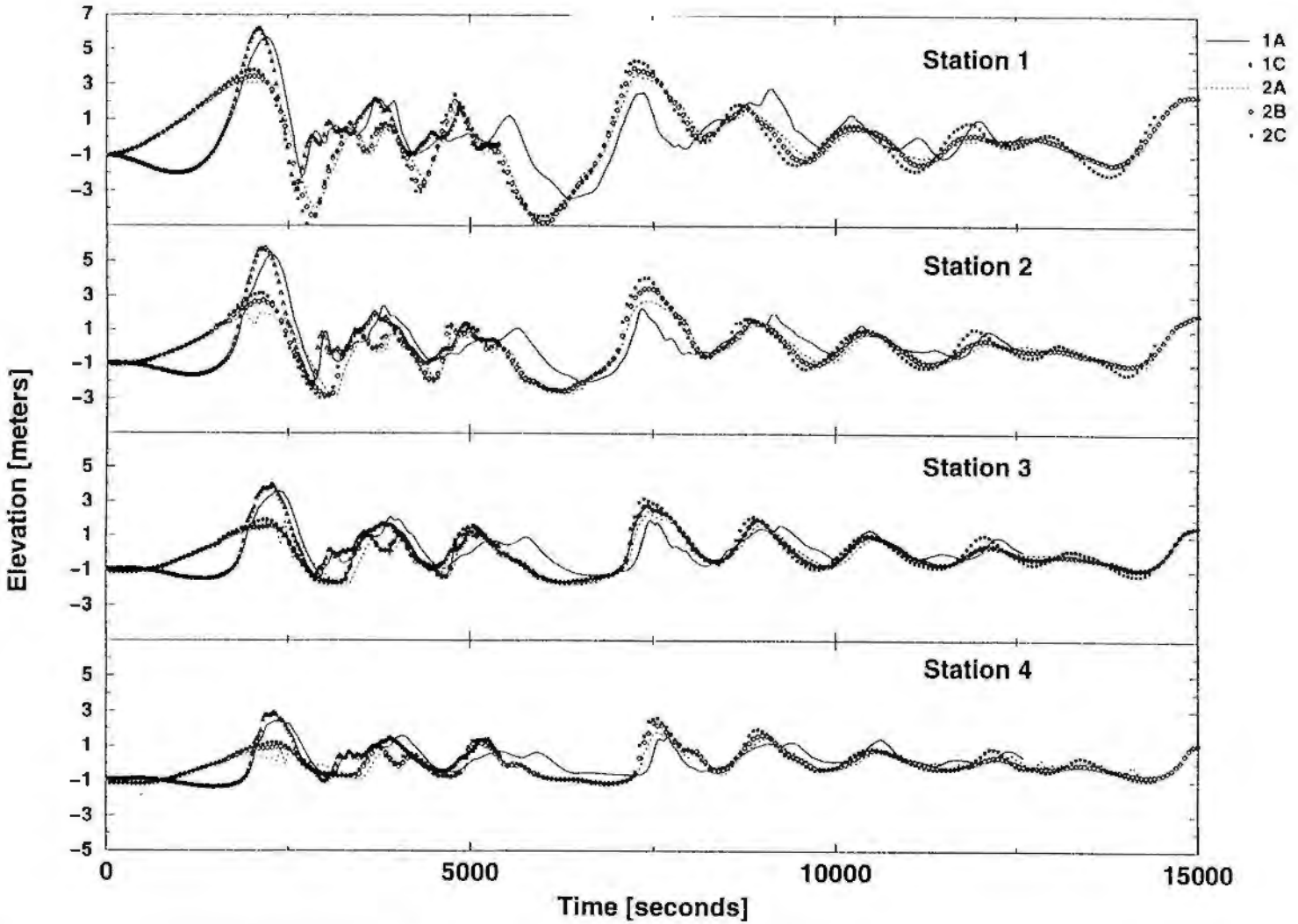

Figure A17a Elevation time histories in the Yaquina Bay channel

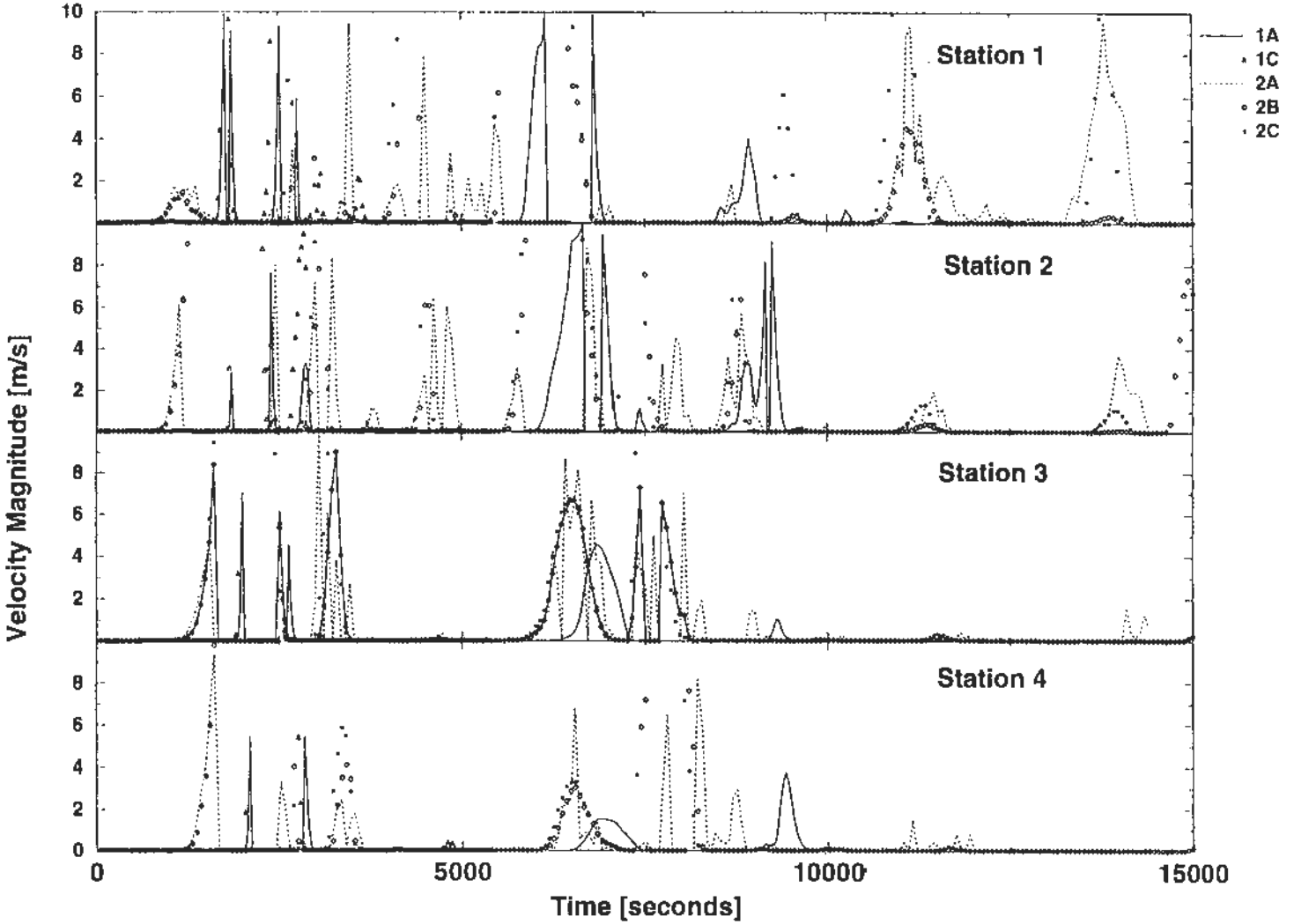

Figure A17b Velocity magnitude time histories in the Yaquina Bay channel

APPENDIX B

MODELING OF TSUNAMI WAVES GENERATED BY AN ADDITIONAL LOCALIZED UPLIFT FEATURE OFFSHORE OF THE YAQUINA BAY AREA, LINCOLN COUNTY, OREGON

Plate boundaries, including subduction zones, build stress in a heterogeneous manner along the fault [Lay and others, 1981; Rundle and others, 1984]. In some areas, the fault exhibits little stress and the interacting plates appear to slide past each other in aseismic or small seismic events. In other regions of the plate boundary, a large amount of stress appears to build, suggesting that the two plates are not able to move easily past each other. These regions of higher strength, or rough spots, on the fault plane are called asperities. Much of the research theorizing and investigating asperities was conducted in the 1980's by Hiroo Kanamori [Kanamori 1981; Lay and others, 1981; Ruff and Kanamori 1983; Rundle and others, 1984].

The presence of an asperity in a subduction zone may result in an area of concentrated coseismic (during the earthquake) slip during a subduction zone event that is sufficiently large to 'break' the asperity. The increase in slip corresponds to a vertical uplift which is significantly larger than the general uplift for the fault. This localized area of intensified bottom deformation has the potential to produce a tsunami or modify the tsunami waves produced by the larger fault rupture. Although there is no consensus on the nature of asperities, the associated high-slip areas are proposed to be present in several great subduction zone earthquakes [Ruff and Kanamori 1983; Barrientos and Ward 1990; and Yabuki and Matsu'ura 1992].

A concerted effort of finite element computer modeling was completed to investigate the possible effects of an asperity, and more specifically the area of concentrated uplift, on tsunami wave heights and coastal inundation. A variety of Gaussian (bell-shaped) uplifts were added to previously investigated earthquake deformations to test the sensitivity of the study area to these potential tsunami sources. Several model runs were completed to show the potential impact of such a source on the Yaquina Bay area in Lincoln County, Oregon.

Test Channel:

In order to investigate the effects of various sized asperities, numerous test channel cases were run. A rectangular channel 15 km wide and 130 km long (from 30 km offshore of the subduction zone to the shoreline) was constructed at the latitude of the Yaquina Bay area near Newport, OR. The grid was made of regularly spaced right triangle grid cells (see Figure B1). The size of the grid cells decreased at set locations along the x-axis of the channel, sometimes referred to as a nested grid. Higher discretization of the grid at the shore-side of the channel allows for better representation of the wave in shallow water and the inundation that may follow.

A profile of actual bathymetry at the latitude of Newport, OR was extracted from Myers and Baptista's regional grid. The bathymetry was then mapped across the 15 km wide channel so that the depth was independent of latitude (y-direction) across the channel. A similar procedure for extracting and mapping was used to construct the bottom deformations for the channel. The simplified grid spacing of the test channel allowed for faster computational times; this allowed numerous model runs with various sizes and shapes of asperity type ruptures to be completed in the test channel. The y-independent bathymetry and bottom deformations allowed for more direct interpretations of the model results.

Three deformation scenarios, 1A, 2A, and 2B (all referenced earlier in this report), were completed in the test channel. Scenario 1A, a magnitude 9.1 earthquake with a 1,050 km long rupture, and 15-20 m of slip, showed the highest run-up of the three models in the test channel (See Table B1). These results agreed with Myers and Baptista's results for the regional grid. The majority of the remaining model runs were therefore completed using scenario 1A as the baseline deformation in the test channel.

A variety of 1-dimensional (extending across the entire width of the channel) Gaussian shaped uplift areas were added to the baseline scenarios. Amplitude, width, and location of these deformation features were varied systematically. A strong linear relationship was seen between the amplitude of the uplift and the wave height at the coastline. Similarly, a proportional relationship was seen between the width (standard deviation) of the Gauss curve and the maximum wave height. More data are needed to better analyze these relationships. The location of the imposed uplift was also a significant parameter. Surprisingly, in certain locations, the uplift feature interfered with the propagation of the main wave generated at the subduction zone, and diminished the maximum run-up. Table B1 summarizes a few of test channel results.

TABLE B1

Scenario	Max. Elevation Center of coastline (meters)	Maximum Elevation in Grid (meters)
1A	12.0	12.8
2A	9.6	10.4
2B	7.6	8.1
1A + high-slip	13.2	13.5
2A + high-slip	11.5	11.7
2B + high-slip	12.0	12.3

Table B1: Summary of test channel model results. This table lists the results for various test channel model runs. Scenarios 1A, 2A, and 2B are background deformation scenarios described earlier in this report. The same high-slip area (Amplitude=4.43 m, σ=13 km) was added to each background scenario.

After the results of the test channel runs were analyzed, several decisions were made on the location, amplitude, length and width of the high-slip uplift area to be carried out in the larger regional grid.

Pacific Northwest Grid:

The final asperity runs were made using the Pacific Northwest regional grid (Grid 2) constructed by Myers (See Appendix A for description). Grid 2 had higher resolution around Yaquina Bay and Seaside, OR. All Cascadia subduction zone (CSZ) Gaussian uplifts were superimposed on a 9.1 magnitude earthquake that ruptured the entire length of the subduction zone with 15-20 m of slip proposed by Fleuck, Hyndman, and Wang (known as Scenario 1A as adapted by Myers, Baptista and Priest). Scenario 1A produced the largest run-ups on the open coast of any of the scenarios run by Myers, Baptista and Priest. The maximum deformation for this scenario was an uplift of 7.6 meters. The results from scenario 1A were used to draw the 'Moderately high run-up' line on the Tsunami Hazard Map of the Yaquina Bay Area. The model runs were performed using the same modeling techniques and codes used in the previous regional grid model runs.

The Alaska 1964 Prince William Sound deformation constru[1] cted by Holdahl and Sauber [199?] included several areas of concentrated deformation. The dimensions$_1$ (length, width, cross-sectional area, and volumes) of these high-slip areas were estimated and used as a reference to construct CSZ asperity like ruptures.

The location for a realistic asperity induced uplift was concluded to be in the locked zone of the subduction zone. Relating this to CSZ, the high-slip uplift area was centered approximately 26 km inshore from the crest of maximum deformation or 71 km offshore. It was placed on the continental slope in 865 meters of water. In order to have a maximum impact on the study area, the high-slip area was placed directly offshore of Yaquina Bay, centered at a latitude of approximately 44^0 40'N (See Figure B2). Several model runs with various size two-dimensional Gaussian high-slip uplift areas, all centered in the same location, were completed. Only the most relevant model runs are discussed here.

An uplift of 6.0 meters amplitude was added to the 1A scenario; the total vertical uplift at the feature was 7.5 meters. As noted earlier, the maximum uplift of the baseline case was 7.6 meters. This extreme value in scenario 1A was located in a small area at the northern end of the subduction zone. Although not the point of maximum uplift, the high-slip feature imposed was the dominant uplift formation. This was especially true for the Yaquina Bay area due to the placement of the rupture directly offshore. The dimensions$_1$ of the 6.0 m rupture (1ArunC) were 46 km wide by 119 km long (area of uplift greater than 0.5 m was 36 km by 93 km). The cross-sectional area of the high-slip area in 1Arun C was 120,800 m^2, and the volume was 6.2 km^3.

Further investigation of documented high-slip areas on other subduction zones [Barrientos and Ward 1990; and Yabuki and Matsu'ura 1992] and conversations with others researchers [Kanamori 1997] suggested that a 'reasonable' high-slip area owing to an asperity has roughly twice the slip as the entire fault. For CSZ, with a 10 degree dip angle and 15-20 meters of slip, the generalized fault uplift was 2.6-3.5 meters. Using the previous relationship, a theoretical value of total uplift owing to an asperity was found to be 5.2-7.0 meters. Therefore, the final run was made with an amplitude of 4.5 m superimposed in the area of 1.5 m uplift of Scenario 1A at the given location to make a total uplift of 6 meters (1ArunD).

A relationship between the length and width of high-slip areas was also noted by measuring those associated with the 1960 Chile earthquake

[Barrientos and Ward 1990] and the 1946 Nankaido earthquake [Yabuki and Matsu'ura 1992]. It was determined that the asperity type ruptures are about 1.5 times as long as they are wide. A characteristic width of these ruptures was estimated to be 80-90 km. Therefore, the final model run (1ArunD) was constrained by these parameters. Its dimensions$_1$ were approximately 100 km wide by 150 km long, with the significant uplift (> 0.5 m) contained in an area 76 km by 114 km. This was markedly different from the previous cases where the length of the asperity was more that three times the width. It also followed that 1ArunD had a much wider uplift area than the previous cases. The deformation, with the high-slip area, used in 1ArunD is represented in Figure B2.

The cross-sectional area and the volume of the high-slip area in 1ArunD were 201,800 m^2 and 13.7 km^3 respectively. Although this uplift feature had a larger area and volume than those used in previous runs, the values of this theoretical rupture were still in the range of other proposed deformation features. The deformation of the 1964 Alaskan earthquake [Holdahl and Sauber, 199?] showed two areas of concentrated vertical uplift which were estimated to be 10 km^3 and 15 km^3.

Yaquina Bay Wave Heights:

The far field effects of the theoretical high-slip area owing to an asperity were seen by contrasting the results of scenario 1A and 1ArunD. Using sampling technique developed hy Myers (described in Appendix A), a plot of the maximum coastal run-up versus latitude was generated (Figure B3, center panel) for model runs 1A and 1ArunD. A significant increase in the maximum run-up owing to the high-slip area in 1ArunD was seen in the latitudes of Oregon (42N to 46N). The largest differences in run-up occur between 44N and 46N. This is due to the location of the high-slip area centered at approximately 44^0 40'N (See Figure B2). The added rupture area appeared to have small effects on the maximum run-up outside the immediate area.

The local effects of an added area of concentrated deformation on the Yaquina Bay area are shown on the Tsunami Hazard Map (O-97-?). The 'High run-up' line was achieved by analyzing the result of model 1ArunD. Comparisons of the inundation patterns and maximum elevations for scenario 1A and 1ArunD showed that the high-slip area had a large influence at the open coast. Closer investigation revealed that the high-slip

area produced significant increases in elevations throughout the Yaquina Bay region.

The potential influence of this high-slip area was further investigated by closely comparing time histories in the Yaquina Bay area. Using sampling techniques developed by Myers (discussed in Appendix A), time histories were taken at a total of seven stations around the Yaquina Bay area. The locations of these stations are illustrated in Figure B4 (labeled A-E, OCN and OCS). All stations were chosen at locations that remained wet throughout all three model simulations (1A,1ArunC, and 1ArunD) to allow for better comparison. For this reason, the open coast stations, OCN and OCS, were placed in at least 9 meters of water to avoid drying.

Figure B5 shows the time histories computed at two open coast stations (OCN and OCS) and at the channel entrance (station A) for scenario 1A, 1ArunC and 1ArunD. As expected, the high-slip area produces a larger amplitude incident wave than scenario 1A by itself. Also apparent, is the earlier arrival of the 1ArunD wave owing to it's closer proximity to the coastline. Scenario 1ArunD, the wide high-slip area with an uplift of 6.0 m, produced a larger trough after the first wave.

By looking at the patterns of inundation and the high run-up line on the hazard map, it appeared the influence of the added deformation diminished as the wave propagated into the bay. However, analyzing the time histories for the first wave entering the bay showed that the percentage increase of elevations was highest (54%) at the back bay station (station E). In contrast the channel entrance (station A) only showed a one-third (33%) increase in water elevations from the 1A case, while the open coast stations (OCN, OCS) showed an average increase of 40%. The back bay increase was not readily apparent in the Yaquina Bay inundation patterns due to the relatively steep topography surrounding the bay. The largest low-lying area near the bay is east of the south support of the US 101 bridge. This area did show significant differences in the inundation patterns when the wide high-slip area (1ArunD) was imposed. Other low lying study areas will likely show dramatic differences in inundation patterns if a high-slip area is imposed directly offshore.

As a supplement to this research, the sensitivity of the study area to various tsunami sources was investigated by comparing the run-up and inundation patterns from several different high-slip areas. Comparisons were made between the various model runs; the differences between 1ArunC, a narrower but larger amplitude rupture, and 1ArunD, a wider but smaller amplitude area, are discussed here. Sampling techniques

identical to those used above, were employed to contrast 1ArunC, (46 km wide, 7.5 m maximum uplift; see previous section for other dimensions) with 1ArunD (100 km wide, 6.0 m maximum uplift).

The right panel of Figure B3 illustrates the maximum run-up for the two asperity rupture scenarios versus latitude. The significant differences between the two lines again occurred between the latitudes of 44N and 46N. They are nearly identical outside this area. This suggests that the proposed localized high-slip areas have a corresponding limited area of impact along the coast. Additional comparisons between the tsunami source mechanisms were completed by generating time histories for model 1ArunC at the stations described earlier (Figure B4). The elevation time histories for the two asperity rupture cases (Figures B5 and B7) were very similar.

The most dramatic differences between the two high-slip cases (1ArunC and 1ArunD) were seen in time histories of the first wave at the open coast stations (Figure B5). The most striking difference was the trough after the first wave. Water elevations dropped much lower in run D than in run C, suggesting that more water receded from the bay in scenario 1ArunD than in 1ArunC. Given that the area under the curve for the first wave was larger and that a larger volume of water flowed onshore, the larger trough could be justified. The moving water volumes were related to the volumes of the high-slip areas. Since the added rupture area in1ArunD possessed over twice the volume (13.7 km^3 to 6.2 km^3) of 1ArunC, it followed that 1ArunD displaced a larger volume of water toward the coastline. Additional research to relate the cross-sectional area and volumes of the deformations to the maximum run-up is underway.

Also evident in Figure B5 is the larger amplitude for the 1Arun C wave recorded at stations OCN and OCS. The amplitude of the rupture in 1ArunC was 25% higher than in 1ArunD; this difference in amplitude of the high-slip area produced elevations from 1ArunC that were 8% higher than those from 1ArunD. It is proposed here that a wider rupture for the larger amplitude would have produced an increase in elevations that approached the 25% factor. Finally, Figure B7 shows the arrival of waves generated in case 1ArunD arrived shortly before those of 1ArunC. This is due to the wider nature of the rupture in 1ArunD. Since the two ruptures were centered in the same location, the wider one obviously had an uplift closer to the coastline, causing the waves to arrive faster.

SUMMARY

Imposing a localized rupture feature offshore of the study area had a significant impact on the maximum run-up, time histories of elevations, and, to a lesser extent, the patterns of inundation. However, in low-elevation study areas, it is likely that superimposing an asperity type rupture will have more dramatic effects. These studies should be completed for various study areas to investigate the vulnerability of each community to such an event.

Both the amplitude and width of a theoretical high-slip area owing to an asperity are important measures of their potential impact on the coast. A larger amplitude rupture produced higher elevations at the open ocean coast, while a wider rupture caused larger increases in elevations inside the Yaquina Bay area. Cross-sectional area and/or volumes of the concentrated uplift areas are obviously better measures of the bottom deformation, and therefore tsunami generating potential. More data are needed to see if a direct relationship exists between the shape or size of an asperity and the maximum run-up at the coast.

---

1 All dimension measurements were made using the xmgredit, and xmvis programs, part of the ACE software package, written by Paul Turner at the Oregon Graduate Institute. The edges of the high-slip areas were defined to the 0.1 meter level. Areas of uplift greater than 0.5 meters were considered to be significant uplift.

FIGURES

TABLES

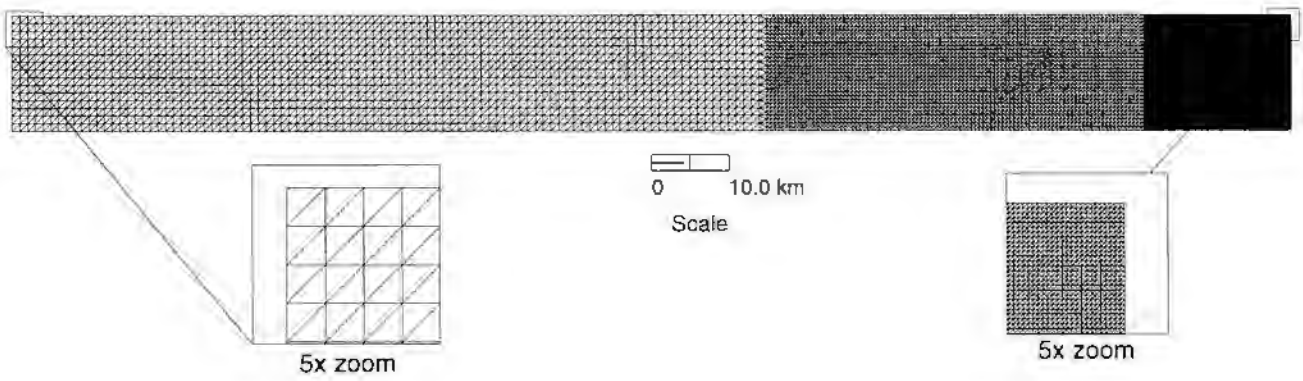

Figure B1. Numerical test channel grid used for finite elment modeling.

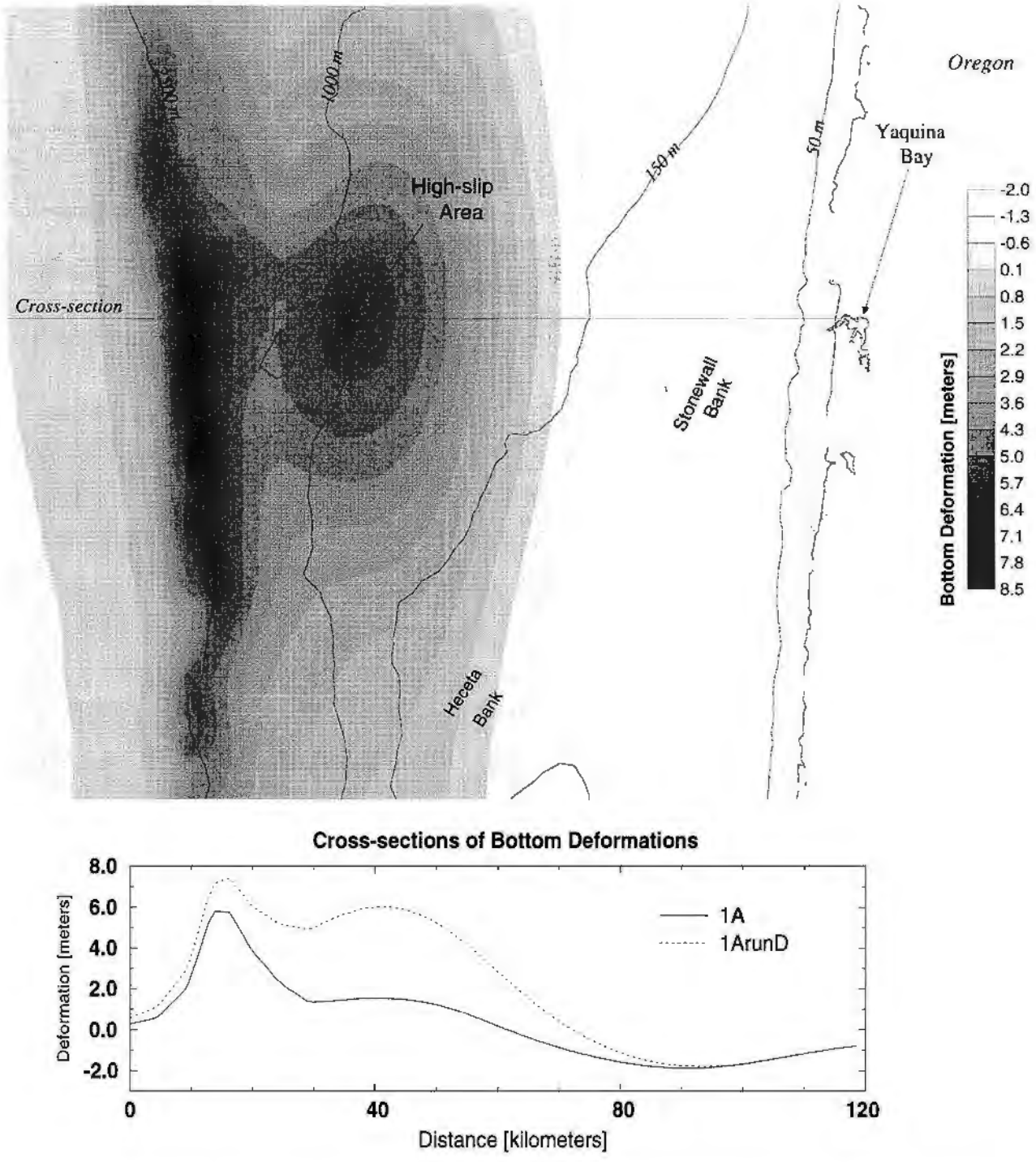

Figure B2. Map of seafloor deformation showing high-slip area for 1ArunD with cross-section of deformations for model 1A and 1ArunD.

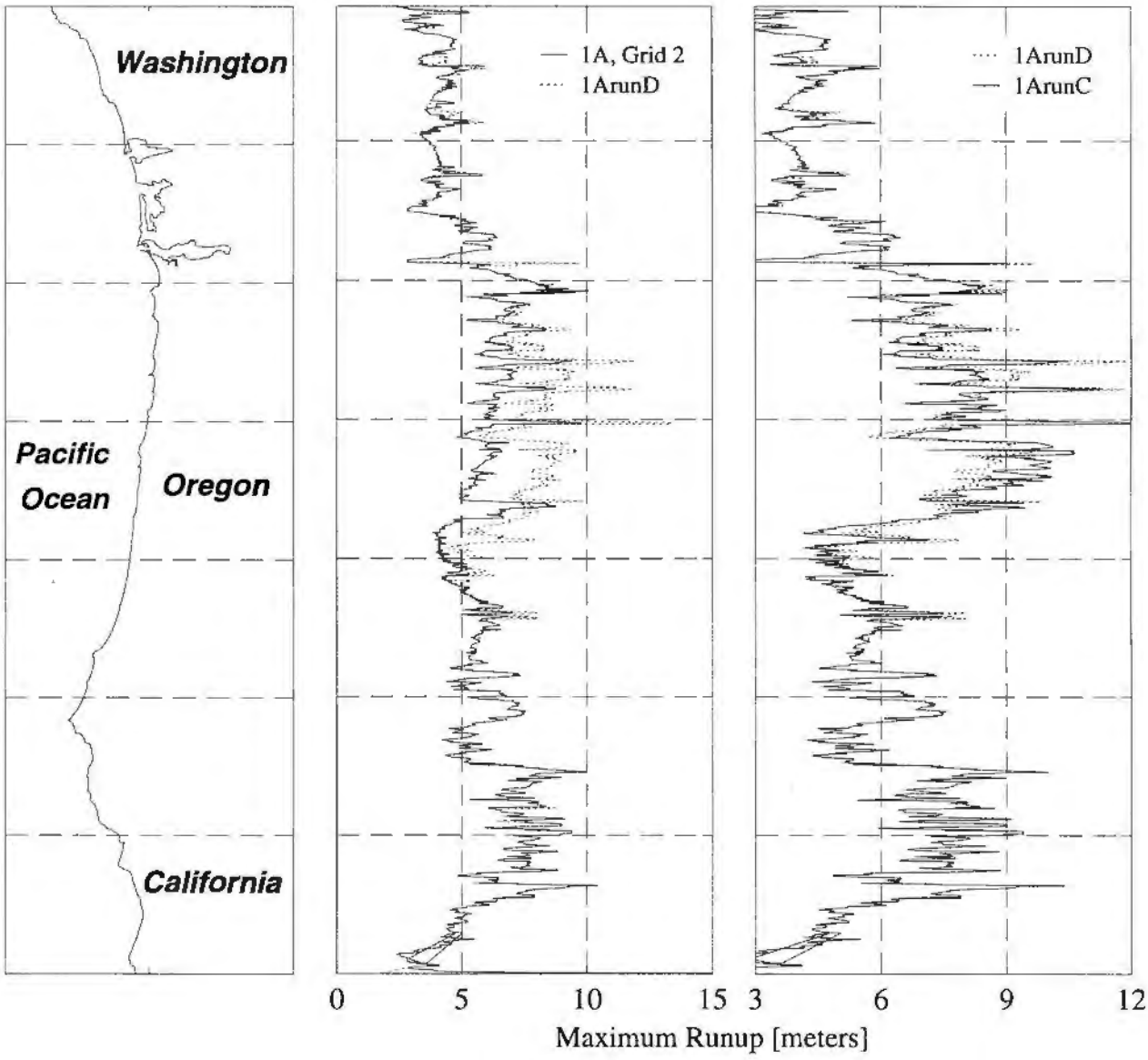

Figure B3. Maximum coastal run-up elevation versus latitude for 1A, 1ArunC, and 1ArunD

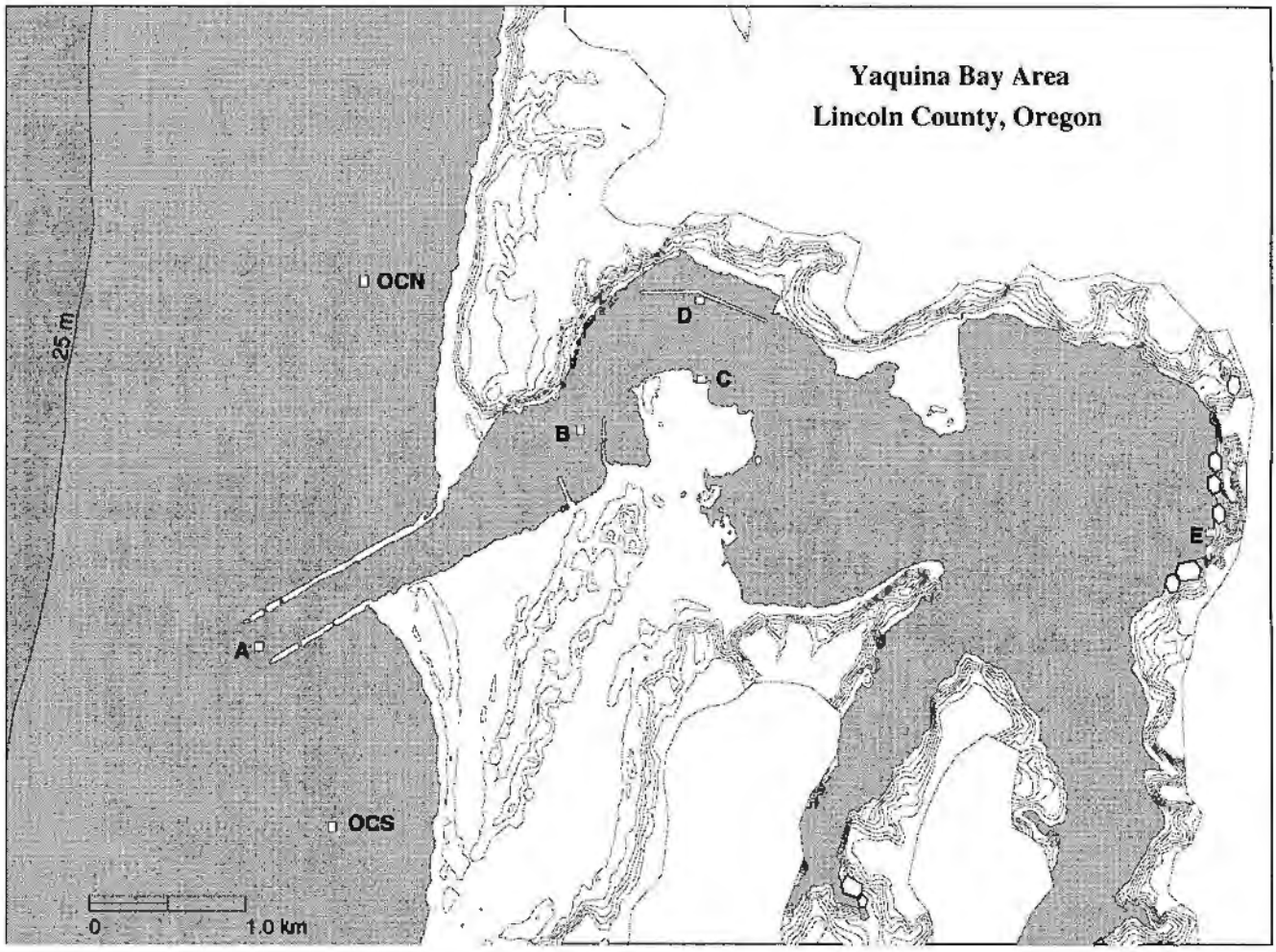

Figure B4. Map of Yaquina Bay study area with time-history station locations

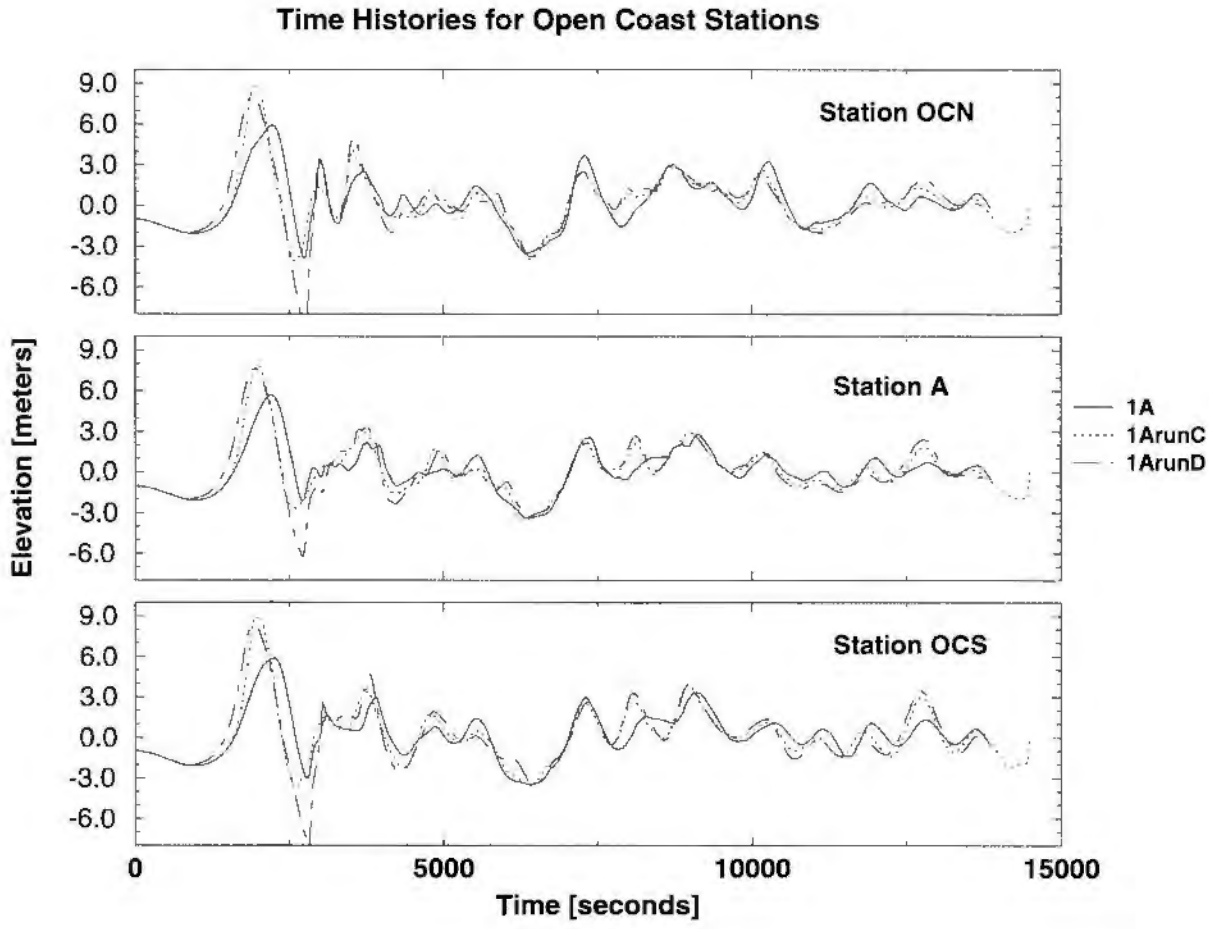

Figure B5. Time histories at open coast stations for model 1A, 1ArunC, 1ArunD

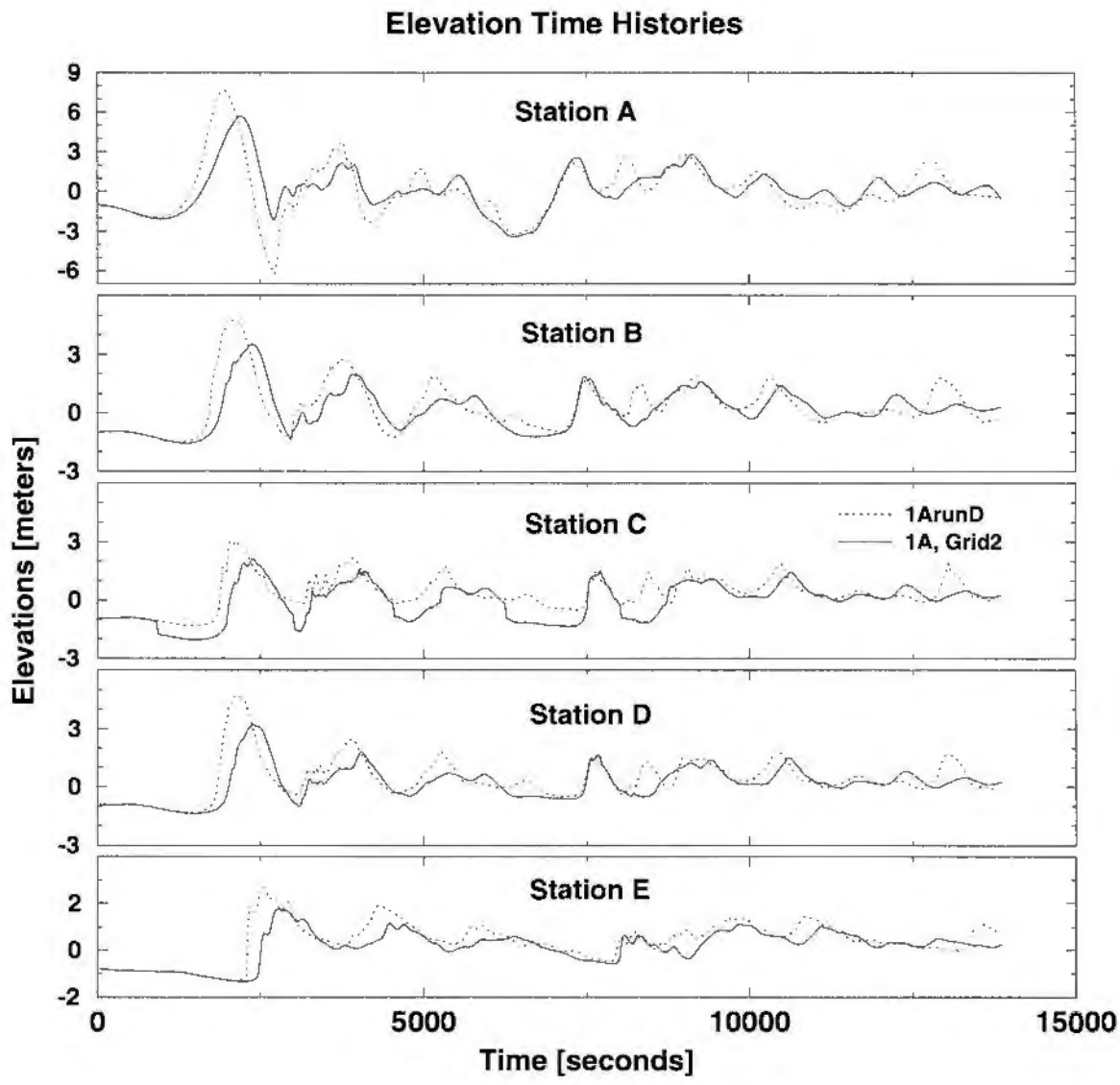

Figure B6. Time histories at stations inside Yaquina Bay for model 1A and 1ArunD

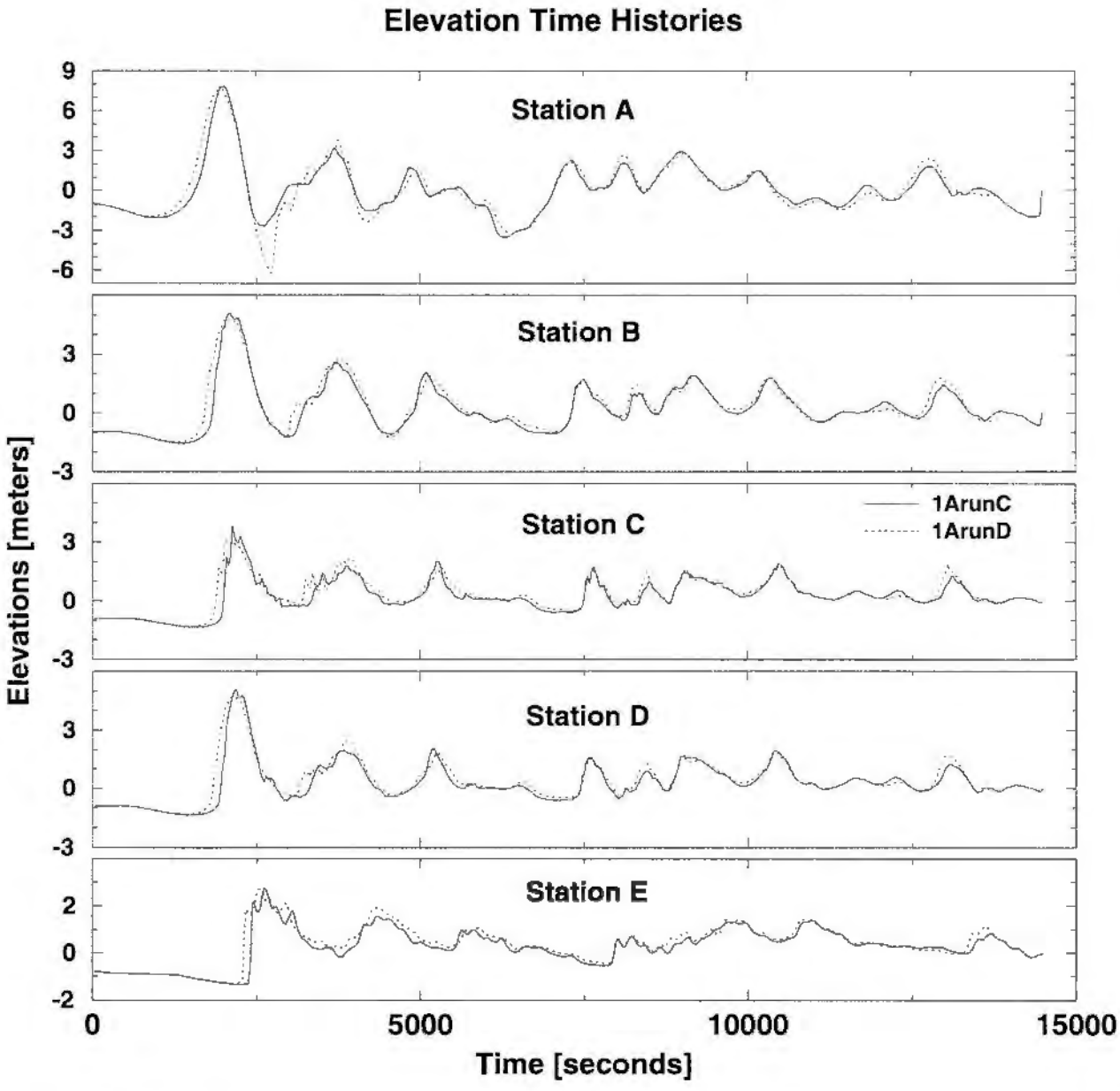

Figure B7. Time histories at stations inside Yaquina Bay for models 1ArunC and 1ArunD

APPENDIX C

FAULT RUPTURE MODELING OF THE CASCADIA SUBDUCTION ZONE FOR A TSUNAMI HAZARD ANALYSIS

George R. Priest
Oregon Department of Geology and Mineral Industries

Edward Myers and Antônio M. Baptista
Oregon Graduate Institute of Science & Technology

Paul Fleuck and Kelin Wang
Geological Survey of Canada

Curt D. Peterson
Portland State University

ABSTRACT

Sea floor deformation from great (M8-9) earthquakes on the Cascadia subduction zone will cause tsunamis to strike the North American coast. Fault dislocation modeling can be used to explore possible vertical deformation scenarios as sources for tsunami simulations. Fully three dimensional models are used here to simulate complex changes in strike, dip, and slip of the subduction zone megathrust. Coseismic ruptures with recurrence on the order of 450 years, slip on the order of 15-20 m, and rupture widths extending well onshore provide a best fit to paleoseismic data. Narrower ruptures that occur mostly offshore in Oregon and northern California provide a best fit to thermal and geodetic data. A rupture 1,050 km long with 15-20 m of slip was utilized as a worst case. Segmented ruptures 450 km in length and 7-10 m slip are most consistent with coupling and aspect (length:width) ratios of world wide analogues to Cascadia. Onshore geodetic and paleoseismic data does not sufficiently constrain coseismic deformation offshore to predict coseismic or interseismic bottom deformation in the seaward transition zone (STZ) updip of the locked zone (LZ). Three cases were simulated: (1) coseismic slip in STZ essentially equals slip in the LZ; (2) coseismic slip in STZ linearly decreases from the LZ to the deformation front; and (3) essentially no coseismic slip in the STZ. In all, ten fault dislocation models are presented which illustrate most of the possibilities for vertical deformation caused by regional coseismic plate flexure during Cascadia subduction zone earthquakes. The models do not treat inelastic deformation or deformation from local faults, asperities, or submarine landslides. Any of these phenomena could amplify deformation (and tsunamis) in local areas relative to the models. Inelastic deformation near the deformation front will tend to decrease coseismic uplift relative to the models, because the elastic models produce "spikes" of uplift near the seaward

ends of the buried ruptures. Left lateral faults bounding large clockwise rotating upper plate blocks in areas of oblique convergence can partition the strike-parallel component of convergence, possibly lowering coseismic slip by as much as 13 percent relative to all models.

INTRODUCTION

Scientific findings of the last several years have shown that the Oregon coast is vulnerable to great (M 8-9) earthquakes that can occur on the offshore Cascadia subduction zone fault system (Figure C1; see Madin, 1992, Atwater and others, 1995, and Nelson and others, 1995, for summaries). Such earthquakes can generate tsunamis that will be very dangerous to populated areas of the Pacific Northwest coast. This study explores possible fault dislocation scenarios for great earthquakes on the Cascadia subduction zone. These scenarios will provide sea floor deformation for a companion study of numerical simulations of tsunami inundation. Available data on the geometry of the Cascadia subduction zone and paleoseismic history of earthquakes and tsunamis is used to constrain possible dislocation scenarios.

The impetus for the study is the need for the Oregon Department of Geology and Mineral Industries (DOGAMI) to produce tsunami inundation maps for the Oregon coast. Various map products are used by evacuation planners and by building codes officials in charge of implementation of Oregon Senate Bill 379 (SB 379). SB 379 limits construction of certain critical and essential facilities in potential tsunami inundation zones.

PREVIOUS WORK

Whitmore (1993; 1994) produced estimates of expected tsunami amplitudes from a M_w 8.8 earthquake extending 650 km along the Cascadia Subduction Zone. This dislocation model was based on a fault segment rupture postulated by Weaver and Shedlock (1989) to extend from southern Washington to northern California (41.5° N lat.).

Priest (1995), in cooperative work with Oregon Graduate Institute of Science and Technology, utilized this same rupture length to explore dislocation scenarios. He tried to make the scenarios consistent with prehistoric coseismic deformation at estuarine marsh sites, the dip of the subduction zone, as imaged by seismic reflection and refraction data, and the thermal regime. Fault dislocation modeling was based on either (1) a three-dimensional (3-D) dislocation model derived from Okada (1985) that simulates vertical deformation of rectangular fault planes after coseismic slip on fully locked faults, or (2) linear extrapolation of 2-D profiles of coseismic deformation derived by reversing interseismic uplift and subsidence rates of Hyndman and Wang (1993). Hyndman and Wang's (1993) simulations of interseismic deformation on the Cascadia subduction zone were based on the 2-D

dislocation model of Savage (1983), which incorporates the effects of full and partial locking on the fault plane. Their models simulated the transition from zero to 100 percent slip deficit in the brittle-ductile transition at the down dip (landward) end of Cascadia ruptures (Figure C2). The models could also be used to simulate similar transitions in slip deficit in the up dip (seaward) direction as well (Figure C2). Neither the 3-D nor 2-D model could simulate the complex behavior of the fault zone at sharp changes of strike and dip like those that occur in southern Washington (Figure C1; Weaver and Shedlock; 1989). Changes in strike and dip can be approximated by hand smoothing the data between adjacent rectangular models (3-D cases) or transects (2-D cases) (e.g. Priest, 1995), but this is not an accurate way to simulate fault behavior.

Priest (1995) found that when 2-D and 3-D models were constrained by the same paleoseismic estimates of coseismic subsidence, the 2-D model produced tsunami run-up large enough to explain known paleotsunami deposits, whereas the 3-D model produced tsunamis that were too small. The reason the 2-D method produced higher run-up was its ability to simulate partial locking on the subduction zone. Partial locking in the landward transition from stick slip to stable sliding behavior (Figure C2) spreads the vertical deformation over a larger area, effectively lowering the subsidence for a given amount of slip. Incorporating the transition zone demanded larger slips (and associated sea floor uplift) to produce the maximum of 2 m subsidence indicated by the paleoseismic data.

This paper summarizes the results of modeling coseismic deformation on the Cascadia subduction zone using software developed by Fleuck and others (in press) that allows fully three dimensional (3-D) simulation of locked and partially locked zones. This technique, when combined with geological and geophysical constraints, offers a powerful tool for evaluation of fault rupture scenarios.

ANALYTICAL METHOD

Fault Dislocation Model

The fault dislocation model used here is the method of Fleuck and others (in press). They developed a 3-D fault dislocation model based on point source solutions of the Okada (1985) equations for surface deformation and strain due to shear faults in an elastic half space. A FORTRAN program was written that uses equations (8) and (16) of Okada (1985) to calculate surface deformation and strain due to a point source. Analytical expressions for 3-D simulation of surface deformation and strain caused by fault slip can be obtained by integrating this point source solution over the fault plane. The fault plane is divided into a number of triangular elements, each with a finite area, and a point source is located at the center of mass of every triangle. The solution for

deformation at a surface observation point is obtained by summation of the point source solutions over all triangular elements.

Fleuck and others (in press) tested the 3-D model and found that it reproduced surface deformations from Okada's (1985) 3-D rectangular solution and Savage's (1983) 2-D solution. The best fits were obtained by descretizing the calculation to sufficient triangular elements to reproduce a smooth pattern of displacement.

Sensitivity Analysis

Fleuck and others (in press) also performed sensitivity analysis for variations in thrust fault width, dip, depth, displacement, and transitions between full and partial slip. They found that the fault parameters generally follow simple geometric predictions. Simple geometry demands that decreasing the vertical component of displacement, by decreasing dip or slip, decreases vertical deformation. Deeper burial of the rupture produces smaller, broader surface deformation (Figure C3). Likewise, increasing the width of the rupture broadens the zone of coseismic uplift and subsidence but without significant decrease in vertical displacement for a given slip (Figure C4). The trough of maximum subsidence over a fully locked rupture lies approximately above the down dip end of the rupture (Figure C3).

When the rupture is buried, part of the horizontal deformation is transferred into vertical deformation, owing to compression where the thrusting block runs into a resisting mass at the unruptured end of the buried fault (Figure C3). The resulting "spike" of uplift at the up dip end of the rupture decreases with increasing burial and disappears altogether when the fault slips all the way to the surface (Figure C3). This "spike" may not be a realistic representation of subduction zone behavior, since it is unlikely that the youthful sediments in the seaward portion of the fault zone would offer complete compressional resistance to failure on a buried rupture. The fundamental problem is that the accretionary wedge probably acts to some degree as an inelastic body ruptured by numerous faults, while the model is treating it as an unbroken elastic body. Priest (1995) found that this spike added about 3 percent to the run-up elevation on Cascadia subduction zone scenarios with narrow (5 km) seaward transition zones.

The down dip end of a subduction zone rupture will likely be a zone of transition between brittle and ductile behavior, corresponding to temperatures between 350° C and 450° C (Figure C2; Hyndman and Wang, 1993; 1995). The effect of adding a down dip transition zone, decreasing linearly from full slip to zero slip in down dip direction is illustrated in Figure C5. Uplift and horizontal deformation are shown for a fault with 50 km locked and 50 km transition, compared to fully locked zones with widths of 50, 75, and 100 km. The transition zone does not influence the deformation near the up dip end of the fault, and coseismic subsidence is lower and wider with a transition zone than

without. A linear decrease in coseismic slip across the landward transition zone will be assumed for all scenarios in this study.

The trough of maximum subsidence lies down dip of the fully locked zone by about one half the width of the landward transition zone, so the axis of maximum subsidence for the 75 km locked zone approximately matches the position of the 50 + 50 km case, because both have the same total seismic slip (Figure C5). Note that more displacement is needed to produce the same maximum coseismic subsidence with a transition zone than without, since the displacement is spread out across the transition zone.

Computational Grid

Figure C6 illustrates an example of the computational grids utilized for this study. The computational domains cover the entire region of the Cascadia subduction zone south of the Nootka Fault at Vancouver Island and north of the Mendocino Fracture Zone (Figure C1), extending on land far enough to cover the full extent of each fault rupture width. The grid is arranged in triangular elements whose size is smaller where the model must simulate sharp transitions in slip or dip.

Paleoseismic Data

Paleoseismic estimates of coastal coseismic deformation, especially subsidence, are useful checks on the dislocation models. Evidence for episodic subsidence has been found in estuarine marshes throughout the Cascadia margin (e.g. see Atwater and others, 1995). Some of these events may be caused by regional plate flexure during great earthquakes, while others may be caused by local faults and folds which may or may not be related to great earthquakes. Coastal estuaries generally have continuous sedimentation, owing to eustatic sea level rise. Fringing estuarine marshes without coseismic subsidence usually leave a stratigraphic record of continuous peat development, as marsh sedimentation keeps pace with eustatic sea level rise. Episodic subsidence is indicated by a series of organic-rich marsh soils, each overlain by less-organic-rich intertidal sediment across a very narrow (< a few millimeters) interval. Abrupt changes in organic content is one of many indicators of coseismic subsidence that have been recognized (see Atwater [1996]; Nelson and Personius [1996]; Peterson and Darienzo [1996], and Peterson and others [1997] for comprehensive discussions). Figures C7 and C8 illustrate typical ecological zones in coastal wetlands, and how these zones record relative land-sea level changes. Raw paleosubsidence data and the field calibration of the data for the Cascadia margin is given in Peterson and others (1997).

These data will be projected into a series of east-west profiles for comparison to vertical deformation predicted by the scenario fault dislocation models. The

major problem that must be addressed is the pattern of increasing paleoseismic subsidence landward of the coast at Grays Harbor, Willapa Bay, the Columbia River, Yaquina Bay, and the Siuslaw River (Peterson and others [1997], their Tables 6 and 7). The maximum paleosubsidence in southern Washington and the Columbia River is on the order of 1.5-2+ m (Peterson and others, 1997). It is apparent from Figure C5 that, if this subsidence is coseismic with megathrust events on the Cascadia subduction zone, it was caused by slip on the order of 10-20 m on a rupture extending onshore. The large variability of the subsidence from event to event vertically in single drill core samples (Peterson and others [1997], their Table 7 and Appendix 1) makes it clear that paleosubsidence has not had a constant pattern through time, so a variety of rupture scenarios can be accommodated by the data.

Fault Length

Dependence of Maximum Rupture Length and Recurrence: As noted by Scholz (1982), mean coseismic slip and rupture length for subduction zone earthquakes appear to be linked such that slip = $2 \times 10^{-5} \times$ length. Romanowicz and Rundle (1993) postulated that width rather than length is the controlling variable for slip, but much of their data comes from historical records for strike slip earthquakes rather than interplate thrust events (Scholz, 1994); hence the Scholz ratio will be assumed to apply in this study. Since the maximum amount of slip is dependent on recurrence interval (interseismic strain accumulation), recurrence and rupture length are discussed together.

Mean Recurrence: The mean recurrence is difficult to specify, owing to large errors in the paleoseismic estimates of earthquake age (Nelson, 1992; Atwater and others, 1995), but some crude calculations can be made. Mean recurrence is 400 ± 200 years for northern Oregon estuaries (Darienzo and Peterson, 1995). Atwater and Hemphill-Haley (1996) estimate a recurrence of 500-535 years at Willapa Bay, Washington but note the high variability of interseismic intervals, which range from a few centuries to about 1,000 years. Geomatrix (1995)[1], utilizing most available paleoseismic data for the last 2,800 years suggest that "the entire margin is involved in *sequences of ruptures* (either single ruptures or multiple, closely spaced in time, ruptures) and that the average interval between these sequences is 450 [years] with a 90% confidence interval of 200 years (assuming at most five independent sequences are represented in the data)."

Assuming the Scholz (1982) ratio of slip to length, earthquakes that rupture lesser lengths of the margin will have smaller recurrence intervals. For

[1]Geomatrix Consultants were hired by the Oregon Department of Transportation to do a statewide probablistic acceleration map to guide highway construction practices. This extensive study enlisted the help and advice of most of the scientists actively researching Cascadia subduction zone earthquakes in the Pacific Northwest. The report from this effort summarizes most of the available information up to 1994.

example, Geomatrix assigned an appropriate probability distribution and calculated that lengths of 450 km, 250 km, and 150 km give recurrences of 225, 112.5, and 64 years (Geomatrix, 1995). Atwater (1996) points out that "recognized geologic evidence for great Cascadia earthquakes implies recurrence intervals mostly longer than 300 years."

If the multiple segment rupture model is the rule instead of the exception, then there should be many tsunami sediment layers between coseismically buried soils, since tsunamis from ruptured segments would inundate adjacent segments. Darienzo and Peterson (1995) argue that most potential tsunami sediment layers preserved in marshes on the Cascadia margin are directly atop buried soils thought to record coseismic subsidence from subduction zone events. One notable exception is a probable tsunami deposit that lies between the uppermost two buried soils in Oregon estuaries north of Yaquina Bay (Darienzo and Peterson, 1995; Peterson and Priest, 1995). Examination of the stratigraphic evidence in southern Washington (e.g. Atwater and Hemphill-Haley, 1996) shows a similar lack of potential tsunami sediments other than atop buried soils. Some buried soils may be the result of local faulting, and tsunami deposits are not always preserved or deposited owing to local variations in current velocity, sediment supply, and post-depositional erosion. The paleoseismic data thus offers only permissive evidence that single large ruptures may be more common than a number of small ruptures clustered in time.

The most completely studied Cascadia earthquake is the one that occurred about 300 years ago (Atwater and others, 1995; Nelson and others, 1995). Nelson and others (1995) conclude that the most reasonable earthquake scenario that could explain paleoseismic data for this earthquake is a single rupture that encompassed most of the length of the subduction zone, a distance on the order 1000 km. A series of smaller earthquakes are also consistent with the data, but they would have had to occur within a period of less than 20 years to explain the dendrochronologic ages of trees killed by coseismic subsidence (Nelson and others, 1995). World wide analogues for multiple ruptures on this time frame are rare (Nelson and others, 1995) and there is no paleoseismic evidence to support this scenario. Unless the ruptures occurred over periods of a year or less, multiple tsunamis so generated would leave stratigraphic records of sand layers with intervening intertidal mud layers, but such records are rare in the paleoseismic data for the last event, even in areas with rapid estuarine sedimentation (Peterson and Darienzo, 1992; 1996; Darienzo and Peterson, 1995). instead, most candidate tsunami deposits, particularly those thought to correlate with the 1700 AD event, are single thin blankets of sand with negligible intertidal mud interbeds (Atwater, 1992; Peterson and Darienzo, 1992; 1996; Clague and Bobrowsky, 1994; Darienzo and others, 1994; Darienzo and Peterson, 1995; Peterson and Priest, 1995; Peterson and others, 1997). Therefore there is, again, permissive evidence that at least one of the Cascadia earthquakes may have ruptured nearly the entire length of the subduction zone.

In assigning weighted probabilities for various rupture scenarios, Geomatrix (1995) gave a low weight to a whole-subduction zone rupture, because they could find no historical precedent for a subduction zone rupturing its entire length, and because the aspect ratio (length/width) would be higher than suggested by worldwide data. They also cited lack of historical records in Japan of teletsunamis that might be attributed to magnitude 9+ Cascadia events, particularly the 300 year event. Satake and others (1996) concluded from study of historical records in Japan that a destructive tsunami striking the Japanese coast in 1700 AD is consistent with a magnitnde 9 Cascadia subduction zone earthquake that ruptured the most of the subduction zone. Uncertainties in the numerical simulation of Satake and others (1996), however, make the magnitude assignment highly speculative, and sources other than Cascadia are not ruled out. The match of this date to the dendrochronologic data of Nelson and others (1995) is, however, permissive evidence of a Cascadia event. Continued studies of the dendrochronology of this earthquake in southern Washington have recently narrowed the uncertainty to about 1 year relative to the 1700 AD date (Atwater, 1997, personal communication), so it appears even more likely that the 1700 AD teletsunami in Japan is this Cascadia event.

Recurrence and Coseismic Subsidence: Using interseismic deformation rates from the preferred fault dislocation model of Hyndman and Wang (1993), Priest (1995) concluded that about 400-450 years of interseismic strain accumulation would be needed to produce the maximum of 2.0-2.25 m of coseismic subsidence estimated from paleoseismic data at the Columbia River estuary and Willapa Bay (Peterson and others [1997], their Tables 6 and 7). However, he assumed that the interseismic uplift rate estimated from the elastic dislocation model of Hyndman and Wang (1993) was constant throughout the interseismic period. In reality the rate of interseismic uplift is probably higher in the early part of the cycle, becoming relatively constant after about 300 years (Dragert and others, 1994; Wang and others, 1994). For example, a viscoelastic model approximately matching the fault parameters of Hyndman and Wang (1993) for the Columbia River area predicts maximum uplift rates greater than 10 mm/yr during the first 100 years after an earthquake, falling to about 5 mm/yr after 300 years, and 4.5 mm/yr at 500 years (Wang and others, 1994, their Figure 8b, p. 118.). Therefore the predicted maximum uplift is in excess of 2.6 m over a 450-year cycle. This uplift is larger than the 2.25 m maximum interseismic uplift derived for 450 years from the elastic model of Hyndman and Wang (1993), but within the range of uncertainty in maximum coseismic subsidence estimated from the paleoseismic data of Peterson and others (1997) at the Columbia River. They found that maximum coseismic subsidence there needs to be at least 1.6-1.9 m in order to explain local sediment cores with high marsh soils overlain by intertidal muds. This interpretation is based on surveys of the vertical separation of modern high marsh and tide flats at Deep River, Blind Slough, and the John Day River (all

in the Columbia River estuary). Similar observations have been made in the Willapa Bay area, where greater than about 1.5 m subsidence has been estimated (B.F. Atwater, 1996, personal communication; Peterson and others, 1997). Changes in micopaleontological assemblages at Grays Harbor are consistent with at least one coseismic subsidence event in excess of 1.5 m (Shannon, 1996).

The upper limit of subsidence is not, however, well constrained by these data. Post-seismic rebound (e.g. Plafker, 1978; 1988; Wang and others, 1994) may be so rapid that the maximum subsidence does not leave a stratigraphic record. Peterson and others (1997) list mean vertical separations of 1.6-2.4 m for modern forests at marsh edges (tree roots in peat) to tidal flat conditions (organic-poor mud) in northern and central Oregon estuaries. Higher elevations have less peaty soils as oxidation increases, so larger subsidence than 2.4 m should be noticeable but may be difficult to identify in practice.

The minimum coseismic subsidence needed to bring forested marshes to tidal flat elevations may be lower where there is a restricted tidal range or where fresh water dominates the estuary (Peterson and others, 1997). An example is the Copalis River area where forested high marshes can reach as low as 0.5 m above tide flats (Atwater and Hemphill-Haley, 1996). Data from areas with small tidal ranges were excluded from the compilation of Peterson and others (1997). Areas underlain by thick sections of Holocene sediment may be subject to settlement from compaction during or after an earthquake, thus exaggerating estimated coseismic subsidence. Hence, the main error that could reduce estimated coseismic subsidence is from compaction, and this is not quantified in the compilation of Peterson and others (1997). However, they reduced the bias from this factor by documenting paleotidal level change from multiple sites in the paleosubsidence localities.

In any case, the minimum subsidence of 1.6-1.9 m in the Columbia River estuary is similar to the 2.3 m estimated for the 1964 Alaska and 1960 Chilean earthquakes (Plafker, 1972). Both of these earthquakes had rupture lengths approaching 1000 km, similar to a maximum Cascadia event. However, significant differences in age (temperature) of the subducted plate and convergence rate between these subduction zones and Cascadia make direct comparisons tenuous at best.

Segmented Ruptures: All subduction zones appear to rupture more or less randomly within and across various segment boundaries (e.g. Ando, 1975; Huang and Turcotte, 1990), so a segmented rupture will almost certainly occur at Cascadia in the future. The Geomatrix (1995) analysis assigned the highest probability to a maximum rupture length of 450 km, based on a statistical analysis of aspect ratios of large (magnitude >7.0) thrust earthquakes and potential geological segment boundaries. Goldfinger and others (1992a; 1992b; 1993; 1994) argue that ruptures on Cascadia should be 600 km or less in length because of the narrow locked width (aspect ratio), particularly in

northern Oregon, heterogeneous uplift rates onshore, the broad, weak accretionary wedge, and total lack of seismicity in the wedge. McCaffrey and Goldfinger (1995) concluded that Cascadia has a weak deforming upper plate similar to subduction zones world wide that lack great (magnitude 9) earthquakes.

Darienzo and Peterson (1995) note that the second coseismic subsidence event from the top of the stratigraphic section at Yaquina Bay is absent at Netarts Bay and represented by only weak subsidence evidence at Siletz Bay. However, a tsunami sand layer lies in the same stratigraphic position as this event in most northern Oregon estuaries (Peterson and others, 1993; Darienzo and Peterson, 1995). Darienzo and Peterson (1995) suggest that segment boundaries for this event may lie on the north-central Oregon coast either between Netarts and Nestucca Bays or between Siletz and Yaquina Bays. The weakness of this evidence is the uncertain correlation between possible tsunami sands and buried soils among these estuaries. Scatter in the radiocarbon and stratigraphic data allow a number of possible interpretations.

Geological and geodetic discontinuities at the latitude of Netarts-Yaquina Bay also make this area a possible segment boundary. Near zero geodetic uplift rates increase north and south of the area to values of 1-4 mm/yr (Mitchell and others, 1994). This part of the margin is also characterized by a wide, weak accretionary wedge with landward vergent thrust faults (e.g. Cochrane and others, 1988; Goldfinger, 1994; Goldfinger and others, 1992b). A particularly well developed west northwest left lateral fault cuts the accretionary wedge (Wecoma Fault of Goldfinger and others, 1992b). The youngest Pleistocene marine terrace is cut by faults 5 km south of Siletz Bay at Fogarty Creek and Fishing Rock (Priest and others, 1994). The Wecoma Fault projects to the coastline at about 44.75° N , whereas the faults at Fishing Rock are at about 44.84° N. Segmented rupture scenarios utilized here will terminate at a somewhat arbitrary average position of 44.8° (Depoe Bay, Oregon). This segment boundary will be used for the 450 km rupture scenarios, the most probable earthquakes from the Geomatrix (1995) study.

Conclusions: We conclude that recurrence is on the order of 250-650 years with a mean near 450 years. Large earthquakes rupturing much of the subduction zone in single events are possible though not necessarily the most likely scenarios. The best studied rupture, the 1700 AD event, may have had a length approaching 1,000 km, most likely rupturing in a single earthquake. A scenario rupture extending from the Nootka Fault to the Mendocino Fracture Zone, a distance of 1,050 km, will be simulated here as a maximum possible event. This scene will place an upper limit on rupture length.

The most probable case from the Geomatrix (1995) analysis is a rupture 450 km long. Two scenario ruptures should be considered, one propagating 450

km north to southern Vancouver Island and one propagating south to Eureka, California from 44.8° N latitude.

Fault Strike

The surface trace of the model fault was assumed to coincide with the deformation front. The location of the deformation front is taken from Goldfinger and others (1992b), Clarke (1992), Clarke and Carver (1992), and Fleuck and others (in press). Note, however, that much of the north central part of the margin is characterized by landward vergent thrust faults at the deformation front, so no simple surface trace exists for the megathrust. This complication is ignored in the models, the most seaward fault being assumed to be a simple seaward vergent thrust.

Fault Dip

Megathrust: Fault dip is assumed to correspond to the dip of the décollement on the Cascadia subduction zone. The décollement is thought to lie near the top of the subducted oceanic plate throughout much of the margin (Davis and Hyndman, 1989; Hyndman and others, 1990; and Hyndman and Wang, 1993). The geometry of the décollement below a depth of about 5 km is taken from Fleuck and others (in press) who refined the geometry of Hyndman and Wang (1995) utilizing Benioff-Wadati seismicity, seismic reflection, seismic refraction, teleseismic wave form analysis, and seismic tomography. Their structure contours on the top of the slab, referenced to mean sea level, are shown in Figure C9. The vertical positional error on the contours is estimated to ±0.5 km for the seaward end, increasing to ±5 km at depths of 50 km. The décollement dips 8-12° in potentially seismogenic parts of the subduction zone. The actual model fault plane was smoothed through the data of Fleuck and others (in press) utilizing a polynomial function.

The seaward 2-5 km of the simulated fault plane is extrapolated from the top of the subducted slab to the surface trace of the deformation front utilizing a polynomial curve (Figure C10). The thick (2-3 km) cover of sediment on the subducting slab makes this extrapolation necessary. This locally steeper dip produces a larger component of vertical uplift for a given model slip in this narrow zone.

Secondary Faults: Some portion of the coseismic slip on the Cascadia subduction zone may be partitioned into a variety of secondary faults and folds within the accretionary wedge (e.g. Clarke and Carver, 1992). The dip of these faults increases as they near the surface, approaching 25-45°, so the amount of net slip partitioned into vertical deformation is higher on these structures than on most of the décollement. Sensitivity analyses by Geist and Yoshioka (1996) determined that, given an equal slip, seaward vergent (landward

dipping) thrust faults produce the largest tsunami run-up of any fault type, including the megathrust, since the megathrust has a much lower dip. Berryman and others (1989) found that Holocene uplift associated with a series of seaward vergent thrust faults over a 500 km length of the Hikurangi subduction zone displayed very complex spatial and temporal variation. Offshore mapping of analogous structures on the Cascadia margin (Goldfinger and others, 1992a; 1992b; 1993; in press; Clarke, 1992), reveals that most of them are irregular and discontinuous, the largest ones varying in length from 20- to 80 km. Simulating their behavior is beyond the scope of this study, but their effect on tsunami generation could be important for local areas.

Fault Slip

Ratio of Seismic to Aseismic Slip: To a first approximation, slip magnitude during large subduction zone earthquakes is equivalent to total plate convergence between earthquakes (Davies and Brune, 1971). Later investigations (e.g. Kanamori, 1977) discovered that in most cases only a portion of this convergence slip is expressed as seismic slip, the rest occurring as aseismic slip between earthquakes. Ratios of seismic to total convergence slip (coupling ratio) range from about 0.2 to 0.9 for subduction zones geologically similar to Cascadia (Rogers, 1988). Observations (Pacheco and others, 1993) and theoretical considerations (Wang, 1995) suggest that ratios of 0.2-0.4 can be expected for most subduction zones. Based on the low seismicity of the Cascadia subduction zone, Acharya (1992) argued that seismic slip on Cascadia could be as little as 7 mm/yr (coupling ratio of about 0.2). Geomatrix (1995) estimated moment magnitudes for various Cascadia events based on a statistical analysis of world wide data and possible scenario ruptures. The slip derived from their moment magnitudes for 450 km ruptures varied from 3-6 m, depending on the rupture width chosen. Slip for 1000 km ruptures varied from 5-11 m. Assuming about 18 m of convergence over a 450 years recurrence, these slips correspond to effective coupling ratios of 0.17-0.33 for the 450 km rupture and 0.28-0.61 for the 1000 km rupture. Kanamori and Astiz (1985) estimated a coupling ratio of 0.3 for subducting plates as young as the Juan de Fuca Plate. However, they also estimated that seismic slip of about 20 m equaled total interplate convergence for the 1960 Chile earthquake (coupling ratio of 1.0), which, in the southernmost 250 km, has subducting oceanic crust as young as that at Cascadia (Heaton and Hartzell, 1986, their Figure 5). Ward and Barrientos (1988) estimate that this southernmost part of the 1960 rupture had at least 20 m of coseismic slip, but their estimate is based on geodetic data which cannot distinguish between prompt slip during the megathrust event and slip from aftershocks and creep within hours to months of the event. Indeed the theoretical work of Wang (1995) indicates that significant slip may occur immediately after a great earthquake. Clearly the prompt slip is all that is relevant to tsunami generation. The uncertainty in coupling ratio is therefore 0.2-1.0, based on

analogues to Cascadia, but ratios in the range of 0.2-0.4 are most probable with regard to prompt slip at the time of a great megathrust earthquake.

Assuming a fixed ratio of length to slip (i.e. Scholz, 1982), Rogers (1988) showed that a coupling ratio of 0.3 demands unrealistically long repeat times of 1300-1600 years for ruptures covering the Juan de Fuca or Juan de Fuca-Gorda plate interface with the North American Plate (i.e. the 1,050 km rupture scenario). The alternative is that segments about 300 km long rupture every 450 years. Assuming the Scholz (1982) ratio of slip to length, only 5-6 m of slip is needed for a 300 km rupture. Priest (1995) showed that, regardless of the fault dislocation model used, slip of less than about 10 m (coupling ratio of 0.5-0.6 for 450 years of convergence) does not generate the needed maximum 1.5+ m coseismic subsidence estimated from paleoseismic data (e.g. paleoseismic data from the Slack site of Darienzo and others, 1994; Netarts sites of Darienzo and Peterson, 1990; Grays Harbor, Willapa Bay, and Columbia River sites of Peterson and others, 1997). This conclusion is consistent with the fault dislocation models in this paper as well. Rogers (1988; his Table 2) showed that, if the recurrence rate is 466 years for a single rupture encompassing the Juan de Fuca-Gorda plates, the ratio of seismic slip to total convergence slip would be on the order of 1.0 (no aseismic slip). This is close to the mean Cascadia recurrence estimated independently from paleoseismic data (Geomatrix, 1995; Darienzo and Peterson, 1995; Atwater and Hemphill-Haley, 1996).

As mentioned above, these arguments do not rule out occurrence of some large portion of the slip as aftershocks and creep immediately after a megathrust event. These slips may be considered "coseismic" in the context of some geophysical analyses, whether or not they generate enough deformation to cause significant tsunamis. The paleoseismic data also cannot distinguish prompt subsidence of a great earthquake from that caused by creep or aftershocks happening hours or days later. There is plenty of variation in coseismic subsidence from event to event, as inferred from vertical cores through sequences of buried soils (Peterson and others [1997], their Table 7 and Appendix 1), so events with less than the maximum subsidence are recorded in the same areas where maximum values have been found (e.g. Peterson and others, 1997). Hence, the data do not rule out slips of less than 10 m or segmented ruptures. The entire argument also hinges on the fixed ratio of slip to length found by Sholz (1982), which, as discussed above, is open to debate.

While it is recognized that a coupling ratio near 1.0 is unlikely from a theoretical point of view, it will be used here to establish an upper limit for coseismic deformation and associated tsunami generation. A coupling ratio of about 0.5 will in effect be emulated by the 450 km rupture scenario, since, as explained below, it will have about half the slip of the scenario 1,050 km rupture.

Calculation of Slip: Coseismic slip was calculated by multiplying the convergence rate by recurrence, so the coupling ratio was assumed to be 1.0. The rate and direction of convergence of the Gorda and North American Plate is not known with certainty, owing to probable internal deformation of the Gorda Plate, but the rate of convergence probably follows the southerly decreasing pattern apparent in the data for the Juan de Fuca Plate (e.g. Riddihough, 1984). Hence, all slip calculations are based on the Euler pole solution for Juan de Fuca-North American Plate motion from DeMets and others (1990). Convergence direction varies from N69°E to N59°E and convergence rate 44 to 34 mm/yr from north to south.

A mean recurrence of 450 years yields a slip on the order of 15-20 m at these convergence rates. The scenario segment ruptures of 450 km length yield slip-length ratios of 3-4 X 10^{-5}, much larger than the 2 X 10^{-5} ratio of Scholz (1982). Slip should be about 9 m for such a short segment rupture. This slip demands a recurrence between of 205 and 265 years for the convergence rates used here. Assuming convergence at about 40 mm/yr, mean recurrence of about 225 years is appropriate for calculation of slip for the two segmentation scenarios. The slip so calculated effectively emulates a coupling ratio of about 0.5 for the known recurrence of 450 years.

Utilizing a 450 year recurrence yields a slip-length ratio of 1.4-1.9 X 10^{-5} for a rupture 1,050 km long, well within the error for the regression of Scholz (1982). These values are similar to the 1.9 X 10^{-5} ratio for the 1960 Chilean earthquake, which had a rupture geometry similar to that assumed here (Scholz, 1982).

Secondary Faults: As explained above, some portion of the slip in a megathrust event may be partitioned into secondary faults of the accretionary wedge. Clarke and Carver (1992) found good temporal correlation between probable Cascadia megathrust events and thrusting events on the Little Salmon and Mad River fault zones. The Holocene slip rate on these structures is 6-12 mm/yr, so a significant proportion (17-34 %) of convergence is taken up at faults 50-60 km landward of the deformation front (Clarke and Carver, 1992). According to Clarke and Carver, each thrust event on the two faults had 1-4.5 m of displacement; assuming about a 40° dip (from their cross section of the Little Salmon fault, p. 189), about 0.6-2.9 m of vertical displacement would occur over a narrow zone where the dip was this high. This amount of vertical displacement would probably be important for tsunami generation over the strike length of these faults, but the complexity of simulating these structures is beyond the scope of this study.

McCaffrey and Goldfinger (1995) argue that nearly all of the strike-parallel component of convergence is taken up by inelastic deformation in the North American Plate. The hypothesis is that the strike-parallel component drives clockwise rotation of large blocks of the upper plate. Goldfinger and others (1992a; 1992b; 1993; in press) mapped 9 west northwest trending left lateral

faults bounding these blocks on the continental slope from the latitude of Cape Blanco, Oregon (43° N) to Grays Harbor, Washington (47° N). This inelastic deformation could reduce the interseismic slip deficit on locked and partially locked portions of the subduction zone by as much as 13 percent in this portion of the margin. This potential reduction in slip is not simulated here, so simulated deformation in the central and southern part of the Cascadia margin may be 13 percent too high, if this hypothesis is correct.

Slip Transitions from the Locked Zone: Coseismic slip at the locked zone will probably decrease to near zero slip up and down dip (Hyndman and Wang, 1995). The distribution of the slip in these transition zones (Figure C2) is best understood after a discussion of rupture width.

Rupture Width

Analogous Subduction Zones: The Cascadia subduction zone is one of a class of subduction zones where young (<20 Ma) oceanic crust is subducting. The width of the down dip rupture in analogous subduction zones world wide is on the order of 100 km (Rogers, 1988).

Thermal Control: The locked portion of the fault is, to a first approximation, the coseismic rupture, although the rupture may actually propagate beyond this zone. The down dip limit of the locked zone is probably controlled by temperature, passing from locked (100 percent slip deficit between earthquakes) to unlocked (zero slip deficit) as the plate interface passes from brittle to ductile behavior. This occurs between 350° C and 450° C, according to Hyndman and Wang (1993; 1995). Savage and others (1991) assumed that full locking occurs up to a temperature of 450° C. Hence, there is some disagreement on the fundamental model for the locked zone. In addition, the location of the 350° C or the 450° C isotherms is uncertain, owing to uncertainties in thermal conductivities, temperature gradients, and the dynamic modeling process used to predict temperatures at the subduction zone interface (see Hyndman and Wang, 1993; 1995 for discussion). The lateral uncertainty in the down dip position of these isotherms is on the order of ±20 km for portions of the subduction zone where the dip profile is well constrained (Hyndman and Wang, 1995). The uncertainty is larger where the profile is less well known, as in central Oregon and northern California, but the amount of uncertainty there was not specified explicitly by Hyndman and Wang (1995).

Locked and Landward Transition Zones: Geodetic Strain Constraints: Hyndman an Wang (1993; 1995) and Savage and others (1991) used contemporary deformation rates estimated from geodetic data over the last 70 years or so to constrain the likely width of the locked and transition zones. The assumption is that contemporary strain on land is dominated by interseismic strain accumulation on the subduction zone. Savage and others (1991), utilizing dislocation models fit to high precision geodetic strain data in

Washington, concluded that the strain regime is dominated by the subduction zone. A further assumption is that the pattern (i.e. lateral positions) of contemporary uplift and subsidence is representative of the total interseismic strain history, so reversing the interseismic deformation will yield reasonable estimates of the pattern of coseismic deformation. The latter assumption appears to be valid in general, since study of viscoelastic strain models reveals that after the first hundred years following a model Cascadia subduction zone event, the lateral positions of interseismic uplift and subsidence zones do not change appreciably (Dragert and others, 1994; Wang and others, 1994). The last earthquake was likely in 1700 AD, about 230 years before the interval of geodetic observations, so geodetic strain patterns should approximate the pattern of interseismic strain.

The widths of locked and transition zones estimated by Hyndman and Wang (1995) from the pattern of geodetic strain are shown in Figure C11a). The widths match their estimated location of the 350° C and 450° C isotherms within the large uncertainty in the thermal data (Figure C11a). Fleuck and others (in press) refined the preferred model of Hyndman and Wang (1995), but did not change it significantly (Figure C11b).

Savage and others (1991) fit the interseismic strain data in Washington to a locked zone extending 100 km down dip with a transition zone extending landward an additional 75 km. The equivalent widths of locked and transition zones estimated there by Hyndman and Wang (1995) are 90 km and 90 km. Hence, the overall deformation model is very similar for the two cases, even though the basic assumption about thermal control on the locked zone (350° C for Hyndman and Wang; 450° C for Savage and others) was different.

Locked and Landward Transition Zones: Paleoseismic and Geologic Constraints: Priest (1995) found a mismatch between the pattern of coastal coseismic deformation predicted by paleoseismic data and the pattern predicted by geophysical models of regional plate flexure of Hyndman and Wang (1993; 1995). The match was relatively good from the Columbia River north, where the geophysical data governing the Hyndman and Wang (1993; 1995) models was of highest quality. The match was poor in northern and central Oregon, where the geodetic data has large errors and where there are somewhat fewer geophysical constraints on the dip and temperature of the subduction zone.

As explained above, paleoseismic data in northern and central Oregon is consistent with a rupture zone and corresponding trough of coseismic subsidence onshore. The geodetic data utilized by Hyndman and Wang (1993; 1995) supports an offshore rupture (Figure C11a). This apparent contradiction stems, in part, from interpretation of the data and possibly from differences in the data itself. Regarding the difference in interpretation, both geodetic data and paleoseismic data support decreasing coseismic subsidence (and interseismic uplift) from the northern to central Oregon coastline. Goldfinger

(1994), Mitchell and others (1994), McCaffrey and Goldfinger, and Hyndman and Wang (1993, 1995) attribute this decrease to increasing distance from the locked zone. Peterson and Darienzo (1992; 1996) attribute it to the north to south decrease in distance between the coast and the deformation front, effectively bringing the flexure point between subsidence and uplift (zero isobase) to the shoreline at the latitude of Florence (Siuslaw River). The first case requires decreasing coseismic subsidence from the shoreline east, whereas the second case requires increasing subsidence. The east-west polarity of paleosubsidence is illustrated by paleoseismic studies in south central Oregon, where there is clearly a change from a pattern of near zero subsidence (continuous peat development), to increasing subsidence (black "stripes" of buried peat layers) landward (Figure C12; Briggs, 1994; Briggs and Peterson,1992; 1993). This overall pattern is relatively easy to recognize, even where absolute subsidence is small (< 1 m).

The other reason that both a narrow and wide rupture zone seem to be possible is the chronological difference between the paleoseismic and geodetic data. Geodetic data is a snap shot of crustal deformation rates in the last several decades, whereas the paleoseismic data shows coseismic deformation from a series of past ruptures which may not bear a close resemblance to the next rupture. Indeed it is not entirely clear that current geodetic strain patterns (or rather the sudden reversal of these patterns during the earthquake) are entirely representative of this next event.

The observations on the east-west polarity of the paleosubsidence data led Priest (1995) to conclude that a 70 km locked zone and 70 km landward transition zone provided the best fit to the paleoseismic data in northern and south-central Oregon. Priest (1995) utilized the 70 + 70 model for southern Oregon as well, but suggested that the locked width might be narrower there, owing to subduction of hotter oceanic crust (<6 Ma in age) south of the Blanco Fracture Zone, relative to cooler crust (8-10 Ma) to the north. In fact the age disparity on the subducting plate is largest immediately south of Cape Blanco, where 8-10 Ma oceanic crust is juxtaposed with 4-5 Ma crust across the Blanco Fracture Zone (Peterson and others, 1986). The age of the downgoing plate increases southward, reaching about 6 Ma in the Eureka area. Hence, if there is a narrowing of the locked zone, it would occur abruptly near Cape Blanco and become less apparent in northernmost California. Modeling the thermal structure of the subduction zone south of Cape Blanco is beyond the scope of this study.

In northernmost California Clarke and Carver (1992) argue from paleoseismic and seismic data that the locked zone should be 70 to 80 km wide, extending from about 15-25 km landward of the deformation front landward to where the dip on the subducting plate increases from 11° to 25°. The toe of their locked zone is therefore 85-105 km east of the deformation front; however, they do not consider the possibility of a landward transition zone, so this distance could encompass some portion of a transition. They map east dipping thrust faults

exhibiting stick-slip behavior 50-60 km landward of the deformation front on the subduction zone. Correlation of slip events on these structures with coseismic subsidence events elsewhere on the margin is considered evidence that they deform in concert with stick-slip events on the megathrust (Clarke and Carver, 1992). If one assumes that their stick slip behavior means that these faults lie over the locked zone, then their down dip extent defines a minimum lateral extent of the locked zone. Thrust faults 150-180 km landward of the trench are inferred to penetrate down to the locked zone of the 1964 Alaska earthquake (Figure 4, p. 910 of Plafker, 1972). If the northern California faults dip 30° and penetrate all the way to the megathrust, the maximum landward extent would be 80-100 km east of the deformation front. By this reasoning the toe of the locked zone should lie landward of the deformation front somewhere between the surface trace of the landward-most thrust fault (60 km) and its possible toe in the megathrust (100 km). The geologic evidence is thus consistent with a locked zone extending at least 60-100 km landward of the deformation front in northern California.

Mapped Quaternary thrust faults and folds similar to those in northern California occur onshore in the Coos Bay area but are absent further north, where the coastline is more than 90 km from the deformation front (McInelly and Kelsey, 1990; Goldfinger and others, 1992b). Madin and others (1995) and Madin and Hemphill-Haley (1996) found that the one of the largest and most topographically distinct Quaternary thrust faults in the Coos Bay area (about 85 km from the deformation front) is mnch less active than the faults mapped by Clarke and Carver (1992) 50-60 km from the deformation front in northern California. If this fault is representative, then the structures at Coos Bay may be at the distal end of active compressional deformation from megathrust events. Alternatively, there may be highly active but unrecognized compressional structures present on land at Coos Bay and areas to the north, owing to lack of detailed mapping and trenching. Indeed, Goldfinger and others (1996) show some youthful compressional structures quite close to shore in these areas.

Combining the observations from northern California and south central Oregon, the width of the locked zone and perhaps some portion of the landward transition zone is probably on the order of 60-90 km. This conclusion is consistent with the 70 + 70 km (locked + landward transition zone) model of Priest (1995) inferred from paleoseismic data in northern and central Oregon.

Locked and Landward Transition Zones: Conclusions: The widths of these two zones, as inferred from geodetic and paleoseismic data, are in rough agreement from southern Washington north. Hence, the widths predicted by fitting dislocation models to geodetic data (Hyndman and Wang [1995], as refined by Fleuck and others [1997]) will be used for dislocation modeling in this region. The widths do not match south of the Columbia River, where, as explained above, geodetic data and, to a lesser extent, thermal data support narrow (35-

40 km) locked and landward transition zones, while paleoseismic data favors wider (70 km) locked and landward transition zones. Both cases will be explored in this study.

There may be abrupt narrowing of the locked zone in the vicinity of Cape Blanco, owing to contrasting age of subducted oceanic plate across the Blanco Fracture Zone. Geophysical modeling of this phenomenon is beyond the scope of the study.

Seaward Transition Zone: There is no paleoseismic or geodetic data in offshore areas to constrain the width or coseismic response of the seaward transition zone (STZ), so other, less direct types of data must be used. Hyndman and Wang (1993; 1995) assumed that for all practical purposes the STZ would be negligible, on the order of 5 km wide, based on the high temperature of the subducting oceanic plate. The high temperature should rapidly lithify sediments of the accretionary prism, possibly leading to stick-slip behavior. However, according to observations of Hyndman and others (1993) for the accretionary prism near Vancouver Island, "prism sediments are inferred to be substantially underconsolidated and pore pressures to be high for at least the seaward 30 km of the accretionary prism." Likewise Clarke and Carver (1992) noted that crustal seismicity indicative of coupling at the Gorda-North American plate interface begins about 15-25 km east of the deformation front in northern California. Goldfinger (1994, p. 153) infers from the structural deformation of the accretionary wedge and analogous Nankai subduction zone, that the "wedge itself is too weak to deform elastically and the plate boundary strength contrast is too great to nucleate earthquakes." Hence, a much wider STZ may be a more reasonable assumption for modeling seismic energy release, but it is not clear that it is a reasonable assumption for modeling the coseismic rupture and attendant vertical deformation, the critical forcing for tsunami generation. The coseismic rupture may penetrate into a zone with little or no stick-slip behavior, as the locked zone "pushes from behind" at the STZ during the earthquake; hence a narrow STZ, as assumed by Hyndman and Wang (1993; 1995) must be modeled, regardless of other considerations to explore this possibility. Nevertheless, the other extreme, very little penetration of the coseismic rupture into the STZ must be explored as well to capture potential variations in vertical deformation; hence the width of the STZ is a critical issue.

The down dip (landward) end of the STZ can potentially be inferred from the strike of compressional structures (folds and thrust faults) in the North American Plate (Clarke and Carver, 1992; Goldfinger and others, 1992a; Goldfinger, 1994). Over the locked zone, these structures should strike northwest, approximately perpendicular to the northeast direction of plate convergence. In a seaward zone of stable sliding these structures should strike approximately parallel to the subduction zone (north -south in Oregon and northernmost California; northwest in Washington and British Columbia). In

the latter case, the weak accretionary prism sediments on the continental slope are essentially compressed against a resistant backstop whose trend roughly parallels the strike of the subduction zone. This technique can define the landward extent of the STZ, where the strike of the subduction zone is not perpendicular to the convergence direction (i.e. oblique convergence), as in Oregon and northern California.

Clarke and Carver (1992) mapped the landward limit of the STZ in northern California, where strike of compressional structures changes from north-south to northwest about 15-25 km landward of the deformation front. They note that this is about where crustal seismic activity (seismic front) picks up as well, and related this to a change from stable sliding to stick-slip behavior on the Gorda-North American plate interface (see also empirical and theoretical arguments of Byrne and others, 1988).

There is little crustal seismicity in offshore Oregon, Washington, and British Columbia (see Figure 4 of Heaton and Kanamori, 1984), so no seismic front can be mapped. In Oregon and Washington Goldfinger (1994) and Goldfinger and others (1992a: 1996b) map the updip position of the seismogenic plate interface in the accretionary wedge, where the trend of compressional structures changes from north-south to northwest and where Pleistocene-Holocene sedimentary rock and sediment is juxtaposed with Pliocene and older rock. The younger rock and sediment has two or more of the following features: low wedge taper, landward vergent thrusts, margin-parallel folds, and widely spaced folds (Goldfinger and others, 1996b). In northern Oregon and Washington, this boundary occurs near 1000 m depth, where separate terraces on the continental slope are separated by a major seaward vergent thrust fault (Goldfinger and others, 1992b). Similar terraces appear to continue into northern Washington and British Columbia (see bathymetric map by Pacific Geoscience Centre, Earth Physics Branch, 1978) but are absent from the slope in southern Oregon and northern California (Goldfinger and others, 1992b).

Since nearly orthogonal convergence makes the trend of structures in the STZ and locked zone parallel in Washington and British Columbia, the width of the STZ must be inferred chiefly by analogy to areas of oblique convergence to the south. In general the landward boundary is inferred to lie at about 1,000 m depth in the same geomorphic setting as in northern and central Oregon. In all cases this landward boundary is assumed to be landward of landward vergent structures. North of 44° 45' N in central Oregon, landward vergent anticlines and thrust faults become common in the lowermost continental slope (MacKay and others, 1992). The same structures form the lower slope in Washington (Barnard, 1978). Landward vergent thrusts and folds are probably caused by a combination of low basal shear stress (Seely, 1977) and other, as yet poorly understood factors (MacKay and others, 1992). These structures are assumed to lie in the STZ.

The potential width of the STZ resulting from this mapping technique is displayed in Figure C13. The zone is on the order of 20-30 km wide in British Columbia, southern Oregon, and northern California, becoming 50-60 km wide in northern Oregon and Washington. Note how narrow the locked zone could be, if the STZ reaches this maximum potential width (Figure C13).

Slip Distribution in Transition Zones

Seaward Transition Zone: The STZ will ride passively on the underthrusting oceanic plate, until the earthquake; then coseismic ruptures will propagate into it as the locked plate "pushes from behind," but it is not known to what extent. The STZ may absorb motion by moving as a unit throughout most of its width or by partitioning the movement into numerous secondary faults and folds. Interseismic ruptures may be propagating into the zone, if the coupling ratio is less than 1.0, since slip will be occurring in the locked zone. The models used here can only simulate simple (full) locking on buried faults, which is a poor approximation of this complex behavior. Figures C14 and C15 illustrate the possibilities. Nearly full slip throughout the STZ (Scenario A), linearly decreasing slip across the entire STZ (Scenario B), and nearly zero slip in the STZ (Scenario C) will be simulated to explore the effect on tsunami generation.

Landward Transition Zone: At some distance landward of the locked zone the interface will be so hot that the interseismic slip rate will approach the plate convergence rate. During the earthquake, slip will extend through the locked zone into the transition zone some unknown distance. After the main shock, the remainder of the slip deficit will be made up by post-seismic creep in the transition zone (see summary by Savage and others, 1991).

Savage and others (1991) calculated vertical deformation for both a linear and non-linear variation of slip deficit in the landward transition zone. They found that the pattern of vertical deformation did not vary significantly; thus, following the procedure of Hyndman and Wang (1993; 1995) only a linear decrease in slip is assumed in the scenarios considered here (Figure C14).

Rupture Scenarios

The range of possibilities for various rupture widths and slip distributions are summarized in Table 1. The rest of the variables, as discussed in the text, are:

1. Rupture length of 1,050 km, (recurrence of 450 years)
2. Rupture length of 450 km (recurrence 225 years or coupling ratio of 0.5 for a recurrence of 450 years) rupturing:
    a. 44.8° N to southern Vancouver Island, or
    b. 44.8° N to Eureka, California

3. Coseismic slip
    a. With the strike-parallel component, or
    b. Without the strike-parallel component.
4. Models with or without the "spike" of uplift in the STZ.

Table 1. Maximum hazard scenarios, assuming a 1,050 km rupture length, but varying widths. Rupture scenarios are based on two lateral positions of the LZ and the three STZ coseismic slip distributions illustrated in Figure C14. All assume strain accumulation at 100 percent of the convergence rate over 450 years and a linear change in coseismic slip in the LTZ. The LZ and LTZ of Scenario 1 is narrower than Scenario 2 in Oregon and northern California. See Figure C13 for location of LZ and maximum STZ.

STZ (Slip Distribution)	LZ + LTZ **SCENARIO 1** (Central Oregon LZ = LTZ = 35 km based on Fleuck and others (in press) model)[2]	LZ + LTZ **SCENARIO 2** (Central Oregon LZ = LTZ =70 km based on best fit to paleoseismic data)
SCENARIO A (2-5 km width; linear change in slip deficit)	Model 1A	Model 2A
SCENARIO B (15-60 km width; linear change in slip deficit)	Model 1B	Model 2B
SCENARIO C (15-60 km width; 0 slip deficit over all but the landward 2-5 km)	Model 1C	Model 2C

Combining these variables with those of Table 1, gives a total of 72 scenarios. There are many more possibilities, including smaller slip based on smaller coupling ratios, shorter segment breaks, and local effects from landslides, asperities, and faulting, but these will not be explored.

The purpose of this study is to put limits on the tsunami hazard by examining reasonable rupture scenarios. This purpose may be served without running all possibilities. Only a few of the these 72 dislocation models will adequately illustrate most of the hazard from regional coseismic plate deformation. As previously mentioned, exploring the effect of the "spike" of anomalous uplift in the STZ is beyond the scope of this study, but it is likely to be small (about 3 percent amplification of tsunami run-up) for the narrow STZ case, Scenario A

[2]All models utilize the 350° C and 450° C isotherms of Fleuck (1996) which are very similar to those of Hyndman and Wang (1995).

(Priest, 1995). Subtracting the strike-parallel component of slip from areas of oblique convergence only lowers the vertical deformation in Oregon and northern California by about 13 percent (<0.5 m of vertical deformation at fault dips of 8-12°), so this is not a major effect and will be ignored in this study. This eliminates factors 3 and 4 above.

Assuming a 450 km segment reduces the total slip by about half (225 year recurrence or coupling ratio of 0.5 for a 450 year recurrence) relative to a 1,050 km rupture. Combining this decrease in slip with scenarios of Table 1 that are likely to generate the largest and smallest tsunami run-up will explore most of the variation for moderate hazard scenarios.

As explained below, largest and smallest tsunamis are likely to be generated by Scenarios 1A (narrow LZ and STZ's) and 2C (wide LZ and STZ's), respectively (Table 1). Combining the north and south segment breaks for Scenarios 1A and 2C yields an additional four scenarios (Table 2). Table 3 summarizes the main features potential earthquake magnitudes of all of the scenarios.

Table 2. Moderate hazard scenarios, assuming segmented ruptures. Scenarios are created by using a 225 year recurrence (or coupling ratio of 0.5 for 450 years recurrence) and the slip distribution and vectors of Scenarios 1A and 2C (Table 1). Ruptures extend 450 km north and south of 44.8° N lat.

Slip Distribution (Table 1)	**North Segment**	**South Segment**
Model 1A (narrow STZ; narrow LZ)	1An	1As
Model 2C (wide STZ; wide LZ)	2Cn	2Cs

Table 3. Earthquake magnitude parameters for each scenario. Calculations of moment magnitude assume rigidity = 4×10^{11} dyne/cm^2.

Scenario	Rupture Length (km)	Locked Width (km)	Locked Width in Partially Locked zones (km)	Weighted Mean Locked Width (km)	Slip (m)	(M_w)
1A	1,050	35-105	20-58	78	15-20	9.1
1B	1,050	14-43	33-88	64	15-20	9.0
1C	1,050	14-43	20-58	51	15-20	9.0
2A	1,050	60-105	38-58	107	15-20	9.2
2B	1,050	29-50	48-88	92	15-20	9.2
2C	1,050	29-50	38-58	79	15-20	9.1
1An	450	45-105	53-58	103	7-10	8.7
1As	450	39-45	22-25	60	7	8.5
2Cn	450	29-43	38-58	80	7-10	8.7
2Cs	450	43-50	38	77	7	8.6

Note that these magnitudes are upper limits, since they assume, as does the elastic model, that slip in the STZ is entirely from stick-slip behavior, rather than rupture penetration into relatively weak rock with high fluid pressures, as is likely the case.

RESULTS

Figures C16-C25 show map views of vertical deformation for all of the fault dislocation models. Note the complex pattern of deformation where the subduction zone changes trend from north-south to northwest. The trend of the locked zone of Scenario 1 turns sharply toward the southwest in southern Washington in order to reach the extremely narrow inferred width in northern Oregon (Figures C11b and C13). The trough of subsidence in this southwest trending part of the locked zone is shallower for Scenario 1 than for Scenario 2 (compare Figures C16 and C19); but the most striking difference in the scenarios is the extremely narrow width of the locked zone and attendant uplift for Scenario 1, especially when slip in the STZ is removed (Figures C13 and C18). Subtracting the STZ from the locked zone of Scenario 2 produces a narrow zone of uplift only in the northernmost part of the margin (Figures C13 and C21).

Figure C26 illustrates that, all other factors constant, variations of slip at the STZ (STZ) produce no differences in position or magnitude of subsidence at distances greater than 90 km from the subduction zone. The onshore paleoseismic and geodetic data therefore offer no constraints on the offshore deformation in the STZ.

Figure C23 illustrates that, for a given STZ slip scenario, Scenarios 1 and 2 have very similar vertical deformation, whereas the segmentation models produce about half as much. Figures C27-C29 demonstrate that paleoseismic data is more consistent with the larger slip of the 1,050 km ruptures relative to the 450 km ruptures.

Utilizing the pattern of paleoseismic deformation from the last, best documented subsidence event in 1700 AD and generalized data from previous events, Figures C30-C38 show that the correlation to the paleoseismic data from the Columbia River to the Coquille River in southern Oregon is better for Scenario 2 than Scenario 1, although still far from perfect. Estuaries south of the Columbia River do not reach far enough inland to record paleoseismic data for the entire width of the projected subsidence for Model 2, so definitive discrimination between Models 1 and 2 or between 1,050 versus 450 km ruptures cannot be made. However, As illustrated in Figure C12, and in more detail in Figure C30 (Columbia River), Figure C33 (Yaquina Bay), Figure C34 (Siuslaw River), and Figure C35 (Umpqua River) there is generally less paleosubsidence at the coast than inland; exactly the opposite of Scenario 1.

The paleoseismic data appears to indicate that past Cascadia ruptures may have been somewhat wider and of differing slip distribution from Scenario 2. The wavelength of the Scenario 2 deformation appears to be somewhat broader than the paleoseismic signal (Figure C30) and the trough of subsidence may not be far enough east between the Columbia and Umpqua Rivers (Figures C30-C36). Future modeling could refine the fit in this area utilizing slightly wider locked and landward transition zones. The fit of the paleoseismic data at Coos Bay (Figure C37) is better for Scenario 2 than 1, but the scatter is such that the fit is not definitive. At the Coquille River, the closest profile to the deformation front, the locked zone for Scenario 2 should be somewhat narrower to achieve a better fit to the paleoseismic data.

There is insufficient paleoseismic data south of the Coquille River to make meaningful comparisons (Peterson and others, 1997). As explained above, Holocene faults and folds occur on the coast from Coos Bay south so the signal from regional plate flexure in the paleoseismic data may be contaminated by movement on local structures in this area (e.g. Clarke and Carver, 1992; Madin and others, 1995). Although less common, local faults occur in some areas further north as well (e.g. Goldfinger and others, 1992b) and may locally contaminate the regional signal.

PROBABLE TSUNAMI RUN-UP FROM THE 1,050 KM RUPTURE

As illustrated by the tsunami simulations of Priest (1995) and theoretical work of Tadepalli and Synolakis (1994), an offshore trough of coseismic subsidence leads to higher run-up than an onshore trough. Scenario 1 should thus generate higher run-up than Scenario 2 in Oregon and northernmost California, other factors being equal. Likewise, as the uplift in the STZ decreases from Scenarios A to C (Figure C26); tsunami run-up should decrease as well for most parts of the subduction zone. This observation applies, even though the "spike" of anomalous uplift in Scenario C is somewhat higher than that of the other cases (Figure C26). The short wave length wave created by this "spike" will effectively split into seaward and landward-directed components, reducing its effect, provided the location is far enough offshore for the splitting to occur. Combining these observations, the largest overall run-up should occur for Scenario 1A; the least should be Scenario 2C.

LOCAL EFFECTS ON RUN-UP FROM SCENARIO C

The "spike" of uplift generated by the elastic deformation model for Model C (Figure C27) is only about 40-50 km from shore in the vicinity of Cape Blanco (Figures C18 and C25). Geist and Yoshioka (1996) found that narrow spikes of uplift like these can significantly amplify tsunami run-up when sufficiently close to shore. They explored this phenomenon to illustrate the effects of a near shore fault (their Fault E case). Scenario C may therefore illustrate how such a fault would affect the southern coast, where the shoreline lies relatively

close to local faults within the deformation front. Given the 8-12° dip of the megathrust, maximum uplift should be on the order of 1.5 m for the 450 km ruptures with 7-10 m slip and 3.0 m for 1,050 km ruptures with 15-20 m slip. The "spikes" of uplift for the corresponding ruptures in Scenario C are on the order of 3 and 6 m, respectively (Figures C18, C21-C23, and C27). This extra 1.5 and 3 m of "spike" uplift is similar to what would be generated by a local seaward vergent fault with 100 percent of this slip and a dip of 20°, or less slip and higher dip. The "spike" would lie above such a fault, where the fault cuts the sea floor. The "spike" thus emulates partitioning of the megathrust slip to a local fault near the shelf-slope break.

PROBABLE TSUNAMI RUN-UP FROM THE 450 KM RUPTURES

In near-source areas the initially arriving tsunami wave is mostly controlled by the shape of coseismic deformation (Tadepalli and Synolakis, 1994), so the initial wave for all of the moderate-hazard (450 km) scenarios will resemble the equivalent waves from the 1,050 km ruptures. However the decreased slip in these scenarios will cause a nearly proportional decrease in run-up at the coast (Geist and Yoshioka, 1996).

The other major differences from the 1,050 km scenarios are the oblique wave fronts generated at the ends of the north and south segments (Figures C18-C21; Geist and Yoshioka, 1996) and the smaller extent of the coast affected by the largest tsunamis. These features will produce time histories quite different from the 1,050 km scenarios, as oblique wave fronts refract and reflect up and down the coast.

POTENTIAL ERRORS

Types of Bottom Deformation Not Simulated: The ten fault dislocation scenarios do a reasonable of job exploring large scale variation in regional flexure of the North American plate, but all suffer from over simplification. In particular, none of them consider partitioning of the slip into individual faults and folds of the accretionary wedge, and none consider the important role of asperities. Asperities can cause some parts of the fault plane to accumulate and release far more slip deficit than others.

The 1964 Alaskan earthquake illustrates the importance of asperities and secondary faults. The earthquake produced surface deformation is consistent with 20-30 m of slip in a few central areas of the locked zone, decreasing to 1-6 m in adjacent areas along strike (Holdahl and Sauber, 1994). Significant slip was partitioned into a local thrust fault, causing dip slip of up to 8 m over a length as much as 142 km (Plafker, 1972). Since this fault dips 52°-85°, much of the slip was expressed as vertical displacement. Coastal areas landward of local structures and asperities like these could possibly receive much larger

tsunamis than other areas. Goldfinger (1994) postulates that such asperities may be at Nehalem Bank (off shore of the Columbia River), Heceta Bank (offshore of Newport-Waldport-Florence), and Coquille Bank (offshore of Bandon). However, in a test of slip partitioning to a large secondary fault in northern California margin, Satake (1994) found that the local fault had little effect on the overall pattern of tsunami wave forms for a Cascadia event similar to Model 2Cs.

Submarine landslides and turbidity currents associated with a great earthquake can also generate tsunamis. Landslides on the order of tens of kilometers wide have been mapped on the continental slope (e.g. Goldfinger and others, 1992b). None of the scenarios address this type of bottom deformation.

If the above factors occur together, then the dislocation model could seriously underestimate the hazard. For example, a major asperity should generate greatly amplified shaking, which could enhance the chance of a major submarine landslide. Heceta Bank offshore of Florence, a possible location of an asperity (Goldfinger, 1994), is also the locality of one of one of the largest mapped landslides on the continental slope (see the map of Goldfinger and others, 1992b). Likewise, some of the steepest parts of the continental slope occur in northern California seaward of major thrust faults shown by Clarke and Carver (1992) to partition significant amounts of slip.

"Spikes" of Uplift: All of the models produce sharp "spikes" of uplift at the seaward tip of ruptures. These "spikes" are artifacts of the assumption of perfect elastic behavior on buried ruptures, so they may be viewed in large part as model errors, since the actual ruptures will not likely terminate abruptly and deform the accretionary wedge elastically. The effect is to amplify ground deformation and tsunamis, the tsunami amplification increasing as the "spikes" get higher and closer to shore (e.g. Priest, 1995; Geist and Yoshioka, 1996). Priest (1995) determined that the amplification of run-up from these "spikes" located near the deformation front is on the order of 3 percent. Models 1C, 2C, 2Cn and 2Cs produce the largest of these "spikes" at the nearest shore positions. Amplification of tsunami run-up will presumably be more than 3 percent for these models, particularly where they are near-shore in southern Oregon.

Narrowing of the Locked Zone south of Cape Blanco: If the youthful age of the subducted oceanic plate south of the Blanco Fracture Zone causes a narrowing of the locked zone, then the trough of maximum coseismic subsidence could be offshore in this area. All other things being equal, this offshore trough would produce a leading depression wave which would increase run-up above the values for Scenario 2 (Tadepalli and Synolakis, 1994). This situation may be approximately simulated by Scenario 1 for this area, but the effect of abrupt changes in the locked zone width is not simulated by either Scenario 1 or 2.

These abrupt changes may produce complex coseismic deformation and tsunamis.

Potential Error from the Ratio of Seismic to Aseismic Slip: The ratio of seismic slip to total slip (convergence) was assumed to be 1.0. If, as in many other subduction zones, the ratio is lower than 1.0, then all of the dislocation models overestimate slip. Reducing the slip would, to a first approximation, produce almost a proportional reduction of tsunami run-up elevation, because the coast is so close to the tsunami source (Geist and Yoshioka, 1996).

The amount of slip chosen for the 1,050 km rupture does produce the >1.5 m of maximum coseismic subsidence estimated from paleoseismic data in southern Washington and the Columbia River. Since the scenario was constrained to match this data, approximately the same seismic slip would have been chosen for this scenario in the northern margin, regardless of assumed coupling ratio. There is no paleoseismic estimate of maximum coseismic subsidence south of the Columbia River, because appropriate tidally controlled marsh sites do not penetrate far enough landward to cover the projected location of the subsidence trough. A smaller amount of seismic slip could thus be accommodated in the central and southern margin without violating the paleoseismic data.

Bernard and others (1995) estimated that the coupling ratio is probably about 0.5 for a scenario Gorda Plate rupture. However, even using a slip of 8 m, which approximates a seismic:total slip ratio of 1.0 for their scenario earthquake, the resulting modeled tsunamis were similar to some historic teletsunamis. They discarded this scenario in favor of a model that generated larger tsunamis from a block uplift of 10 m. They argued that this technique took into account the possible occurrence of asperities and submarine landslides in modern analogues to the Cascadia subduction zone. Although the dislocation model used here is different from that used by Bernard and others (1995), it may be that all of the models in Table 2 that assume 7-10 m slip will also produce unrealistically small tsunamis. Likewise, the models with larger slip (Table 1) may still not emulate worst case scenarios, so an additional source similar to that of Bernard and others (1995) may be necessary to fully explore the potential hazard.

Utilizing a wide locked zone, analogous to that of Scenario 2, Priest (1995) found that a slip of about 10.5 m produced the minimum run-up needed to explain the distribution of tsunami deposits at Siletz Bay (Peterson and others, 1995; Priest and others, 1995). Using approximately the same slip with a narrow locked zone (analogous to Scenario 1) produced a leading depression wave with run-up high enough to be at about the upper limit of the run-up estimated from paleotsunami evidence at Siletz Bay. The minimum slip for realistic run-up (i.e. greater than teletsunamis and consistent with paleotsunami run-up) is thus a function of the width of the rupture, being greater for Scenario 2 and smaller for Scenario 1. The model used in the

Bernard and others (1995) study discussed above approximates the wide locked zone of Scenario 2, so this may be the reason that their model produced anomalously low run-up for their model slip.

The minimum slip of 10.5 m inferred in the Siletz Bay study (Priest, 1995) approximates the segmentation cases used here (7-10 m slip; Table 3). The segmentation cases thus emulate a coupling ratio on the order of 0.5 for 1,050 km ruptures (15-20 m total plate convergence slip).

Shorter Segment Ruptures: Arguments have been made by others (e.g. McCaffrey and Goldfinger, 1995; Geomatrix, 1995) for shorter segment ruptures than explored here. Such ruptures would produce much smaller slip and tsunamis. While quite possible from a theoretical point of view, as shown by the studies of Bernard and others (1995), these ruptures would probably produce tsunamis so similar in amplitude to maximum teletsunamis that they would not be useful for hazard planning. Tsunamis of this size are better addressed through modeling teletsunamis that strike far more frequently than Cascadia events..

Other Uncertainties: The amount of vertical deformation, the principal issue for tsunami generation, is most affected by the above factors and the assumed width of the rupture. The range of possibilities for width are well covered by the 10 models. Uncertainties in dip on the megathrust can be no more than a few degrees and, at the low dips of this subduction zone, the effect on vertical deformation is minimal.

Summary of Error Analysis: The most important sources of error for tsunami generation are the amount of slip and width of the rupture. Uncertainty in the coupling ratio is the most important error in estimation of slip. A variation from an effective ratio of 1.0 to 0.5 is covered by the scenarios. South of the Columbia River the scenarios simulate locked and landward transition zone widths of 35 to 70 km, covering most of the uncertainty in this key source of error. The scenarios cover all possibilities for slip in the STZ from near zero slip to slip throughout most of the 15-60 km width.

Landslides, secondary faulting, and possible narrowing of the locked zone near Cape Blanco were not simulated but may amplify sea floor deformation in local areas. All of the models produce sharp "spikes" of uplift at the seaward tip of ruptures. "Spikes" located near the deformation front probably amplify tsunami run-up only about 3 percent. Scenarios 1C, 2C, 2Cn and 2Cs produce the largest of these "spikes" at the nearest shore positions where amplification of run-up will probably exceed 3 percent.

CONCLUSIONS

Based on an analysis of paleoseismic data coupled with empirical studies of great subduction zone earthquakes, the most likely fault ruptures on the

Cascadia subduction zone probably encompass 45 percent or more of the Juan de Fuca-Gorda Plate interface with the North American plate. If some ruptures are segmented, a likely segment boundary lies between Siletz and Yaquina Bays near 44.8° N. Fault dislocation scenarios explored three ruptures lengths: one extending 1,050 km from British Columbia to northern California, one extending 450 km north of 44.8° N to Vancouver Island, and one extending 450 km south of 44.8° N to Eureka, California. Given a constant ratio of length to slip, the segment ruptures have about half the slip of the 1,050 km rupture. Within the uncertainties of the data, width of the locked zone south of the Columbia River can be as little as 35-40 km, according to interpretations of geophysical data, or as much as 70-80 km; according to interpretations of paleoseismic data, so two locked zone widths were also simulated.

Coseismic slip was assumed to decrease down dip from the locked zone in an approximately linear fashion, controlled by a similar linear increase in temperature. This landward transition zone was simulated by a zone of decreasing slip about the same width as the maximum potential width of the locked zone.

Sediment accreted to the outer 15-60 km of the upper plate may rupture with the upper plate nearly to the deformation front, or coseismic slip may near zero in the seaward transition zone. Dislocation scenarios explored both extremes and an intermediate case where slip varies linearly across this zone. None of the resulting dislocation scenarios differed significantly with respect to onshore deformation, so onshore geodetic and paleoseismic data offer no constraints on coseismic slip in the seaward transition zone.

A total of 10 dislocation scenarios describe most of the variation relevant to tsunami generation. The models show complex deformation patterns where the subduction zone changes trend from north-south to northwest. Some of these patterns were not apparent in earlier dislocation models, because this complex geometry could not be simulated by 1-D transects or 2-D rectangular models.

Errors in estimated slip scale almost linearly to errors in tsunami run-up in near-source areas. The ratio of seismic to total slip (coupling ratio) is the most important source of error in the slip estimates. Ratios of 0.2-1.0 are possible. Use here of a coupling ratio of 1.0 probably overestimates the hazard somewhat, particularly in the central and southern part of the margin. The segmentation scenarios with about 7-10 m of slip may be viewed as simulating a coupling ratio of 0.5 over the average recurrence of 450 years (15-20 m of plate convergence).

The 7-10 m of slip derived from the segmentation scenarios approximates the minimum needed to produce run-up estimated from Cascadia paleotsunami data at Siletz. Smaller slips, although theoretically possible, would produce

run-up approximating teletsunamis, adding little to the Cascadia hazard analysis.

Anomalous "spikes" of coseismic uplift occur at the up dip end of all modeled ruptures, because of the assumption of perfect elastic behavior on buried faults. These "spikes" will create short wavelength tsunamis that will amplify run-up more as "spikes" get higher and closer to shore. Amplification is only about 3 percent for "spikes" located near the deformation front. Models assuming little coseismic slip in a wide seaward transition zone produce "spikes" well landward of the deformation front and will probably produce larger amplification of tsunami run-up. The "spikes" may simulate the effect of narrow zones of uplift on secondary faults ramping upward from the megathrust at dips of 20° or more. Future studies should systematically explore the effect of these "spikes" on tsunami run-up.

Complications from asperities on the plate interface, secondary faults, landslides, and changes in rupture width across the subducted Blanco Fracture Zone are beyond the scope of this study, but could amplify scenario tsunamis in local areas. Future studies should evaluate these factors. The investigation of asperities summarized in Appendix B is a good beginning and demonstrates the importance of these factors.

The chosen scenarios thus cover a logical range of possible hazard from regional plate flexure on the Cascadia subduction zone, but do not take into account all factors that could amplify tsunamis. Once numerical simulations of tsunamis have been performed, the derived run-up should be evaluated in the light of available estimates of paleotsunami run-up in such areas as Siletz Bay (Priest and others, 1995; Peterson and others, 1995), Bradley Lake (Nelson and others, 1996), and Willapa Bay (Satake and others, 1994).

ACKNOWLEDGMENTS

Hiroo Kanamori of the California Institute of Technology, Thomas S. Yelin and Samuel H. Clarke of the U.S. Geological Survey, and Robert S. Crosson of the University of Washington gave generously of their time in discussions of possible fault slip and magnitude for subduction zone earthquakes. Chris Goldfinger of Oregon State University contributed the estimated width of the seaward transition zone and provided valuable criticism of the paper. The project was supported by grants from the Oregon Department of Justice and the U.S. Geological Survey's National Earthquake Hazard Reduction Program award number 1434-HQ096-6R-02712.

REFERENCES CITED

Acharya, H., 1992, Comparison of seismicity parameters in different subduction zones and its implications for the Cascadia subduction zone: Journal of Geophysical research v. 97, no. B6, p. 8831-8842.

Ando, M., 1975, Source mechanisms and tectonic significance of historic earthquakes along the Nankai trough, Japan: Tectonophysics, v. 27, p. 119-140.

Atwater, B.F., 1992, Geologic evidence for great Holocene earthquakes along the outer coast of Washington State: Journal of Geophysical Research, v. 97, p. 1901-1919.

Atwater, B. F., 1996, Checklist for down sizing the greatest Cascadia earthquakes [abstract]: Geological Society of America Abstracts with Programs, v. 28, no. 5, p. 44-45.

Atwater, B. F., 1996, Coastal evidence for great earthquake in western Washington, *in* Rogers, A.M., Kockleman, W.J., Priest, G.R., and Walsh, T.J., eds., Assessing and reducing earthquake hazards in the Pacific Northwest: U.S. Geological Survey Professional Paper 1560, p. 77-90.

Atwater, B. F., and Hemphill-Haley, E., 1996, Preliminary estimates of recurrence intervals for great earthquakes of the past 3500 year at northeastern Willapa Bay, Washington: U.S. Geological Survey Open-File Report 96-001, 87 p.

Atwater, B.F., Nelson, A.R., Clague, J.J., Carver, G.A., Yamaguchi, D.K., Bobrowsky, P.T., Bourgeois, J., Darienzo, M.E., Grant, W.C., Hemphill-Haley, E., Kelsey, H.M., Jacoby, G.C., Nishenko, S.P., Palmer, S.P., Peterson, C.D., and Reinhart, M.A., 1995, Summary of coastal geologic evidence for past great earthquakes at the Cascadia subduction zone: Earthquake Spectra, v. 11, no. 1, p. 1-18.

Barnard, W.D., 1978, The Washington continent slope: Quaternary tectonics and sedimentation: Marine Geology, v. 27, p. 79-114.

Bernard, E., Mader, C., Curtis, G., and Satake, K., 1994, Tsunami inundation model study of Eureaka and Crescent City, California: NOAA Technical Memorandum ERL PMEL-103, 80 p.

Berryman, K.R., Ota, Y., and Hull, A.G., 1989, Holocene paleoseismicity in the fold and thrust belt of the Hikurangi subduction zone, eastern North Island, New Zealand: Tectonophysics, v. 163, p. 185-195.

Briggs, G.G., 1994, Coastal crossing of the elastic strain zero-isobase, Cascadia margin, south central Oregon coast: Portland, Oregon, Portland State University masters thesis, Figure 19, p. 176, 251 p.

Briggs, G., and Peterson, C.D., 1992, Neotectonics of the south-central Oregon coast as recorded by late Holocene paleosubsidence of marsh systems: Geological Society of Americal Abstracts with Programs, v. 24, p. 9-10.

Briggs, G., and Peterson, C.D., 1992, Neotectonics of the central Cascadia margin as recorded in south-central Oregon coastal deposits: Final Report to the National Earthquake Hazards Program of the U.S. Geological Survey, 77 p.

Byrne, D.E., Davis, D.M., and Sykes, L.R., Loci and maximum size of thrust earthquakes and the mechanics of the shallow region of subduction zones: Tectonics, v. 7, no. 4, p. 833-857.

Clague, J. and Bobrowsky, P.T., 1994, Evidence for a large earthquake and tsunami 100-400 years ago on western Vancouver Island, British Columbia: Quaternary Research, v. 41, p. 176-184.

Clarke, S.H., Jr., 1992, Geology of the Eel River Basin and adjacent region: implications for Late Cenozoic tectonics of the southern Cascadia subduction zone and Mendocino triple junction: American Association of Petroleum Geologists Bulletin, v. 76, no. 2, p. 199-224.

Clarke, S.H., Jr., and Carver, G.A., 1992, Late Holocene tectonics and paleoseismicity, southern Cascadia subduction zone: Science, v. 255, p. 188-192.

Cochrane, G.R., Lewis, B.T.R., and McClain, K.J., 1988, Structure and subduction processes along the Oregon-Washington margin: PAGEOPH, v. 128, nos. 3/4, p. 767-800.

Darienzo, M.E., and Peterson, C.D., 1990, Episodic tectonic subsidence of Late Holocene salt marshes, northern Oregon, central Cascadia margin: Tectonics, v. 9, p. 1-22.

Darienzo, M.E., and Peterson, C.D., and Clough, C., 1994, Stratigraphic evidence for great subduction-zone earthquakes at four estuaries in northern Oregon, U.S.A.: Journal of Coastal Research, v. 10, no. 4, p. 850-876.

Darienzo, M.E., and Peterson, C.D., 1995, Magnitude and frequency of subduction zone earthquakes along the northern Oregon coast in the past 3,000 years: Oregon Geology, v. 57, no. 1, p. 3-12.

Davies, G.F., and Brune, J.N., 1971, Regional and global fault slip rates from seismicity: Nature, v.229, p. 101-107.

DeMets, C., Gordon, R.G., Argus, D.F., and Stein, S., 1990, Current plate motions: Geophysical Journal International, v. 101, p. 425-478.

Dragert, H., Hyndman, R.D., Rogers, G.C., and Wang, K., 1994, Current deformations and the width of the seismogenic zone of the northern Cascadia subduction thrust: Journal of Geophysical Research, v. 99, p. 653-668.

Fleuck, P., 1996, 3-D dislocation model for great earthquakes of the Cascadia subduction zone: Zurich, Switzerland, Swiss Federal Institute of Technology Diploma Thesis, completed at University of Victoria, Victoria, B.C., Canada, 105 p.

Flueck, P., Hyndman, R.D., and Wang, K., in press, 3-D dislocation model for great earthquakes of the Cascadia subduction zone, Journal of Geophysical Research.

Geist, E., and Yoshioka, S., 1996, Source parameters controlling the generation and propagation of potential local tsunamis along the Cascadia margin: Natural Hazards, v. 13, p. 151-177.

Geomatrix Consultants, 1995, 2.0, Seismic source characterization, *in* Geomatrix Consultants, Seismic design mapping, State of Oregon: Final Report prepared for Oregon Department of Transportation, Project No. 2442, p. 2-1 to 2-153.

Goldfinger, C., 1994, Active deformation of the Cascadia forearc: implications for great earthquake potential in Oregon and Washington: Corvallis, Oreg., Oregon State University Ph.D. thesis, 202 p.

Goldfinger, C., Kulm, L. D., Yeats, R.S., Applegate, B., MacKay, M.E., and Cochrane, G.R., 1996, Active strike-slip faulting and folding of the Cascadia subduction-zone plate boundary and forearc in central and northern Oregon, *in* Rogers, A.M., Walsh, T.J., Kockelman, W.J., and Priest, G.R., eds., Assessing earthquake hazards and reducing risk in the Pacific Northwest: U.S. Geological Survey Professional Paper 1560, p.223-256.

Goldfinger, C., Kulm, L. D., Yeats, R.S., Applegate, B., MacKay, M.E., and Moore, G.F., 1992a, Transverse structural trends along the Oregon convergent margin: Geology, v. 20, p. 141-144.

Goldfinger, C., Kulm, L. D., Yeats, R.S., Mitchell, C., Weldon, R.E., III, Peterson, C.D., Darienzo, M.E., Grant, W., and Priest, G., 1992b, Neotectonic map of the Oregon continental margin and adjacent abyssal plain: Oregon Department of Geology and Mineral Industries Open-File Report O-92-4, 17 p.

Goldfinger, C., Kulm, L. D., Yeats, R.S., 1993, Oblique convergence and active strike-slip faults of the Cascadia subduction zone: Oregon margin

[abstract]: EOS, Transactions of the American Geophysical Union, v. 74, no. 43, p. 200.

Goldfinger, C., Kulm, L. D., Yeats, R.S., 1994, An estimate of maximum earthquake magnitude on the Cascadia subduction zone: Geological Society of America Abstracts with Programs, v. 26, no. 7, p. A-525.

Goldfinger, C., Kulm, L. D., Yeats, R.S., Applegate, B., MacKay, M.E., and Cochrane, G.R.,1996a, Active strike-slip faulting and folding of the Cascadia plate boundary and forearc in central and northern Oregon, *in* Rogers, A.M., Kockleman, W.J., Priest, G.R., and Walsh, T.J., eds., Assessing and reducing earthquake hazards in the Pacific Northwest: U.S. Geological Survey Professional Paper 1560, p. 223-256.

Goldfinger, C., McNeill, L.C., Kulm, L. D., and Yeats, R.S., 1996b, Width of the seismogenic plate boundary in Cascadia: structural indicators of strong and weak coupling [abs.]: Geological Society of America Abstracts with Programs, v. 28, no. 5, p. 69.

Heaton, T.H., and Hartzell, S.H., 1986, Source characteristics of hypothetical subduction zone earthquakes in the northwestern United States: Bulletin of the Seismological Society of America, v. 76, p. 675-708.

Heaton, T.H., and Kanamori, 1984, Seismic potential associated with subduction in the northwestern United States: Bulletin of the Seismological Society of America, v. 74, no. 3, p. 933-941.

Holdahl, S.R., and Sauber, J., 1994, Coseismic slip in the 1964 Prince William Sound Earthquake: a new geodetic inversion: PAGEOPH, v. 142, no. 1, p. 55-82.

Huang, and Turcotte, 1990: Nature, v. 348, p. 234-236.

Hyndman, R.D., and Wang, K., 1993, Thermal constraints on the zone of a major thrust earthquake failure: the Cascadia subduction zone: Journal of Geophysical research, v. 98, no. b2, p. 2039-2060.

Hyndman, R.D., and Wang, K., 1995, The rupture zone of Cascadia great earthquakes from current deformation and the thermal regime: Journal of Geophysical Research, v. 100, no. B11, p. 22,133-22,154.

Hyndman, R.D., Wang, K., Yuan, T., and Spence, G.D., 1993, Tectonic sediment thickening, fluid expulsion, and the thermal regime of subduction zone accretionary prisms: The Cascadia margin off Vancouver Island: Journal of Geophysical Research, v. 98, p. 21,865-21,876.

Hyndman, R.D., Yorath, C.J., Clowes, R.M., and Davis, E.E., 1990, The northern Cascadia subduction zone at Vancouver Island: Seismic

structure and tectonic history: Canadian Journal of Earth Science, v. 27, p. 313-329.

Kelsey, H.M., 1990, Late Quaternary deformation of marine terraces on the Cascadia subduction zone near Cape Blanco, Oregon: Tectonics, v. 9, p. 983-1014.

Kanamori, H., 1977, Seismic and aseismic slip along subduction zones and their tectonic implications, *in* Talwani, M,., and Pittman, W.C., eds., Island arcs, deep sea trenches and back-arc basins: Maurice Ewing series, American Geophysical Union, v. 1, p. 163-174.

Kanamori, H., and Astiz, L., 1985, The 1983 Akita-Oki earthquake (M_w = 7.8) and its implications for systematics of subduction earthquakes: Earthquake Prediction Research, v. 3, p. 305-317.

Madin, I.P., and Hemphill-Haley, 1996, Late Quaternary faulting in the South Slough area, Coos County, Oregon: Geological Society of America Abstracts with Programs, v. 28, no. 5, p. 87.

Madin, I.P., McInelly, G.W., and Kelsey, H.M., 1995, Geologic map of the Charleston Quadrangle, Coos County, Oregon: Oregon Department of Geology and Mineral Industries, GMS 94, 1:24,000 scale.

McCaffrey, R., and Goldfinger, C., 1995, Forearc deformation and great subduction earthquakes: implications for Cascadia offshore earthquake potential: Science v. 267, p. 856-859.

McKay, M.E., Moore, G.F., Cochrane, G.R., Moore, J.C., and Kulm, L.D., 1992, Landward vergence and oblique structural trends in the Oregon margin accretionary prism: implications and effect on fluid flow: Earth and Planetary Science Letters, v. 109, p. 477-491.

Mitchell, C.E., Vincent, P., Weldon, R.J., III, and Richards, M.A., 1994, Present-day vertical deformation of the Cascadia margin, Pacific Northwest, U.S.A.: Journal of Geophysical Research, v. 9, p. 12,257-12,277.

Nelson, A.R., 1992, Discordant ^{14}C ages from buried tidal-marsh soils in the Cascadia Subduction Zone, southern Oregon coast: Quaternary Research, v. 38, p. 74-90.

Nelson, A. R., Atwater, B. F., Bobrowsky, P. T., Bradley, L., Clague, J. J., Carver, G. A., Darienzo, M. E., Grant, W. C., Krueger, H. W., Sparkes, R., Stafford, T. W., Jr., and Stuiver, M., 1995, Radiocarbon evidence for extensive plate-boundary rupture about 300 years ago at the Cascadia subduction zone: Nature, v. 378, no. 23, p. 371-374.

Nelson, A.R., Kelsey, H.M., Hemphill-Haley, E., and Witter, R.C., 1996, A 7500-yr lake record of Cascadia tsunamis in southern coastal Oregon:

Geological Society of America Abstracts with Programs, v. 28, no. 5, p. 95.

Nelson, A.R., and Personius, S.F., 1996, Great earthquake potential in Oregon and Washington – an overview of recent coastal geologic studies and their bearing on segmentation of Holocene ruptures, central Cascadia subduction zone, *in* Rogers, A.M., Kockleman, W.J., Priest, G.R., and Walsh, T.J., eds., Assessing and reducing earthquake hazards in the Pacific Northwest: U.S. Geological Survey Professional Paper 1560, p. 91-114.

Okada, Y., 1985, Surface deformation due to shear and tensile faults in a half-space: Bulletin of the Seismological Society of America, v. 75, no. 4, p. 1135-1154.

Pacheco, J.F., Sykes, L.R., and Scholz, C.H., 1993, Nature of seismic coupling along simple plate boundaries of the subduction type: Journal of Geophysical Research, v. 98, p. 14,133-14,159.

Pacific Geoscience Centre, Earth Physics Branch, 1978, Juan de Fuca Plate map: relief: Ottawa, Canada, Surveys and Mapping Branch, Canadian Department of Mines and Resources, 1:2,000,000 scale.

Pacific Geoscience Centre, Earth Physics Branc, 1978, Juan de Fuca Plate map: relief: Ottawa, Canada, Surveys and Mapping Branch, Department of Energy, Mines and Resources, 1:2,000,000 scale.

Peterson, C. D., Barnett, E.T., Briggs, G.G., Carver, G.A., Clague, J.J., and Darienzo, M.E., 1997, Estimates of coastal subsidence from great earthquakes in the Cascadia subduction zone, Vancouver, Island, B.C., Washington, Oregon, and northernmost California: Oregon Department of Geology and Mineral Industries Open-File Report O-97-5, 44 p.

Peterson, C.D., and Darienzo, M.E., 1992, Discrimination of climatic, oceanic, and tectonic mechanisms of cyclic marsh burial from Alsea Bay, Oregon, U.S.A.: U.S. Geological Survey Open-File Report 91-441-C, 53 p.

Peterson, C.D., and Darienzo, M.E., 1996, Discrimination of climatic, oceanic, and tectonic mechanisms of cyclic marsh burial, Alsea Bay, Oregon, *in* Rogers, A.M., Kockleman, W.J., Priest, G.R., and Walsh, T.J., eds., Assessing and reducing earthquake hazards in the Pacific Northwest: U.S. Geological Survey Professional Paper 1560, p. 115-146.Peterson, C.D., and Priest, G.R., 1995, Preliminary reconnaissance of Cascadia paleotsunami deposits in Yaquina Bay, Oregon: Oregon Geology, v. 57, p. 33-40.

Peterson, C.D., Darienzo, M.E., Doyle, D.D., and Barnett, E.,1995, Evidence for coseismic subsidence and tsunami inundation during the past 3000

years at Siletz Bay, Oregon, in, Priest, G.R., ed., Explanation of mapping methods and use of the tsunami hazard map of the Siletz Bay area, Lincoln County, Oregon: Oregon Department of Geology and Mineral Industries Open-File Report O-96-5, p. 45-69.

Peterson, C.P., Kulm, L.D., and Gray, J.J., 1986, Geologic map of he ocean floor off Oregon and the adjacent continental margin: Oregon Department of Geology and Mineral Industries, GMS-42, 1:500,000 scale map, 4 p. text.

Plafker, G., 1972, Alaskan earthquake of 1964 and Chilean Earthquake of 1960: implications for arc tectonics: Journal of Geophysical Research, v. 77, p. 901-925.

Plafker, G., 1978, Uplift history and earthquake recurrence as deduced from marine terraces on Middleton Island, Alaska, *in* Proceeding of Conference VI, methodology for identifying seismic gaps and soon-to-break gaps: U.S. Geological Survey Open-File Report 78-943, p. 687-72.

Plafker, G., 1988, Tectonic deformation related to great subduction zone earthquakes [unpublished abstract]: *in* Holocene subduction in the Northwest: Quaternary Research Center Spring Symposium, May 6-8, 1988.

Priest, G. R., 1995, Explanation of mapping methods and use of the tsunami hazard maps of the Oregon coast: Oregon Department of Geology and Mineral Industries Open-File Report O-95-67, 95 p.

Priest, G.R., Baptista, A., Qi, M., Peterson, C.D., and Darienzo, M.E., 1995, Simplified explanation of the tsunami hazard map of the Siletz Bay area, Lincoln County, Oregon *in* Priest, G.R., ed., Explanation of mapping methods and use of the tsunami hazard map of the Siletz Bay area, Lincoln County, Oregon: Oregon Department of Geology and Mineral Industries Open-File Report O-96-5, p. 1-20.

Priest, G.R., Saul, I., and Diebenow, J., 1994, Explanation of chronic geologic hazard maps and erosion rate database, coastal Lincoln County, Oregon, Salmon River to Seal Rocks: Oregon Department of Geology and Mineral Industries Open-File Report O-94-11, 46 p.

Riddihough, R.P., 1984, Recent movements of the Juan de Fuca plate system: Journal of Geophysical Research, v. 89, p. 6980-6994.

Rogers, G.C., 1988, An assessment of the megathrust earthquake potential of the Cascadia subduction zone: Canadian Journal of Earth Science, v. 25, p. 844-852.

Romanowicz, B., and Rundle, J. B., 1993, On scaling relations for large earthquakes: Bulletin of the Seismological Society of America, v. 83, no. 4, p. 1294-1297.

Satake, K., 1994, Appendix G: Earthquake scenario study with regional tsunami model *in* Bernard, E.N., Mader, C., Curtis, G., and Satake, K., Tsunami inundation model study of Eureka and Crescent City, California: National Oceanographic and Atmospheric Administration Memorandum ERL PMEL-103, p. 43-65.

Satake, K., Shemazaki, K., Yoshinobu, T., and Ueda, K., 1996, Time and size of a giant earthquake in Cascadia inferred from Japanese tsunami records of January 1700, 1996, Nature, v. 379, no. 6562, p. 246-249.

Satake, K., Reinhart, M.A., and Bourgeois, J., 1994, Comparison of computed tsunamis with analysis of tsunami deposits for the 300-year-old Cascadia event, SW Washington: Geological Society of America Abstracts with Programs, v. 26, no. 7, p. A-523.

Savage, J.C., Lisowski, M., and Prescott, W.H., 1991, Strain accumulation in western Washington: Journal of Geophysical Research, v. 96, p. 14,493-14,507.

Savage, J.C., 1983, A dislocation model of strain accumulation and release at a subduction zone: Journal of Geophysical Research, v. 88, p. 4984-4996.

Scholz, C. H., 1982, Scaling laws for large earthquakes: consequences for physical models: Bulletin of the Seismological Society of America, v. 72, no. 1, p. 1-14.

Scholz, C. H., 1994, A reappraisal of large earthquake scaling: Bulletin of the Seismological Society of America, v. 84, no. 1, p. 215-218.

Seely, D.R., 1977, The significance of landward vergence and oblique structural trends on trench inner slopes, *in* Talwani, M., and Pitman, W.C., eds, Island arcs, deep sea trenches, and back-arc basins: American Geophysical Union, Washington, D.C., p. 187-198.

Shannon, I., 1996, Quaternary Science Reviews, v. 15, p. 1-37.

Tadepalli, S., and Synolakis, C.E., 1994, The run-up of N-waves on sloping beaches: Proceedings of the Royale Society of London, v. A445, p. 99-112.

Wang, K., 1995, Coupling of tectonic loading and earthquake fault slips at subduction zones: PAGEOPH, v. 145, Nos. 3 and 4, p. 537-559.

Wang, K., Dragert, H., and Melosh, H.J., 1994, Finite element study of uplift and strain across Vancouver Island: Canadian Journal of Earth Science, v. 31, p. 1510-1522.

Ward, S.N., and Barrientos, S.E., 1988, Earthquake fault shape and slip pattern from inversion of geodetic data, *in* Jacobson, M.L., and Rodriguez, T.R., National Earthquake Hazards Reduction Program, Summary of Technical Reports, Volume 25: U.S. Geological Survey Open-File Report 88-16, p. 456-465.

Weaver, C.S., and Shedlock, K. M., 1989, Potential subduction, probable intraplate, and known crustal earthquake source areas in the Cascadia subduction zone, *in* Hays, W.W., ed., Proceedings of the 3rd Annual Workshop on Earthquake Hazards in the Puget Sound, Portland area: U.S. Geological Survey Open-File Report 89-465, p. 11-26.

Whitmore, P. M., 1993, Expected tsunami amplitudes and currents along the North American coast for Cascadia subduction zone earthquakes: Natural Hazards, v. 8, p. 59-73.

Whitmore, P. M., 1994, Expected tsunami amplitudes off the Tillamook County, Oregon, coast following a major Cascadia subduction zone earthquake: Oregon Geology, v. 56, no. 3, p. 62-64.

FIGURE CAPTIONS

Figure C1. Plate tectonic map of the Cascadia subduction zone fault system illustrating the location of the surface trace of the fault at the deformation front. The subduction zone is bounded by the Nootka and Mendocino transform faults and dips 8-12° toward the east. Figure taken from Fleuck (1996).

Figure C2. Schematic illustration of the zones of slip in a subduction zone. As water-saturated sediments at the deformation become progressively lithified, the fault behaves with more and more stick-slip behavior until it is fully locked at the base of the seaward transition zone (STZ). In the landward transition zone (LTZ), the fault movement changes from stick slip to stable sliding behavior as the temperature rises.

Figure C3. Sensitivity of surface deformation to burial of a rupture 1000 km long and 50 km wide with 10 m of pure dip slip thrust motion. Horizontal (U) and vertical deformation are illustrated. Note how deformation decreases with burial. The anomalous "spike" of uplift at the up dip end disappears, when the rupture reaches the surface (Figure taken from Fleuck, 1996; see text for explanation).

Figure C4. Sensitivity of surface deformation to rupture width on a fault 1000 km long with a slip of 10 m and dip of 12 degrees. Numbers are widths in kilometers. Note how the trough of subsidence migrates landward with increasing width but maintains the same depth.

Figure C5. Sensitivity of surface deformation to addition of a landward (down dip) transition zone. The fault is 1000 km long with dip of 12 degrees and 10 m of pure dip slip thrust motion. The locked and transition zones are 50 km wide. Slip decreases linearly from 10 m to zero in the transition zone. Coseismic deformation from fully locked buried ruptures with widths of 50, 75, and 100 km are shown for comparison. Note how the same total slip in the 50 + 50 rupture produces about half as much subsidence as the fully locked 75 km rupture.

Figure C6. Numerical grid for the dislocation models.

Figure C7. Typical vertical separation of ecological zones in coastal wetlands. Coseismic subsidence of various magnitudes will cause juxtaposition of these zones in vertical cores as shown, depending on what lateral position is sampled in the wetland. For example, a core taken in an area that is generally at a deep tidal channel will show only tidal channel sediments, unless coseismic uplift of unusual amount were to occur. On the other hand, a core taken in a lateral position generally occupied by the high marsh zone will record coseismic subsidence as buried peat layers in sharp contact with overlying intertidal mud or mud with colonizing marsh plants, depending on the degree of subsidence. Continuous sea level rise without coseismic subsidence would be recorded as continuous peat layers in this same high marsh setting.

Figure C8. Diagram of fossil-lithologic categories of paleotidal level and corresponding amounts of paleosubsidence (0±0.5, 1±0.5, and 2±0.5 m) based on category transitions.

Figure C9. Strike and dip of the subduction zone. Structure contours are in kilometers referenced to sea level. Figure taken from Fleuck (1996).

Figure C10. Schematic illustration of the way that the numerical model propagates the megathrust to the surface through the surficial sediments covering the oceanic plate at the deformation front.

Figure C11a. Illustration of the uncertainty in the location of the isotherms governing width of the locked and landward transition zones. The two lines shown are the best fit by Hyndman and Wang (1995) to available thermal and geodetic data. Figure is from Hyndman and Wang (1995).

Figure C11b. Locked and landward transition zones of Fleuck and others (1996). This model is a best fit to available geophysical data and is very similar to the model in Figure C11a.

Figure C12. Pattern of paleosubsidence in south central Oregon from Briggs (1994). The open circles indicate areas with continuous peat development indicative of near zero paleosubsidence. Dots indicate core sites with abrupt vertical changes in peat development characteristic of episodic paleosubsidence. The pattern of increasing subsidence inland is opposite that predicted by the narrow ruptures illustrated in Figures C11a and C11b.

Figure C13. Maximum potential width of the seaward transition zone (STZ) and possible locations of the down dip end of the locked zone (LZ). Line 1 is the same as in Figure C11b. Line 2 is a possible location which matches patterns of coseismic subsidence inferred from paleoseismic data. Note how line 2 maintains a nearly constant distance from the deformation front (west side of the STZ).

Figure C14. Schematic illustration of the coseismic slip distributions for STZ scenarios considered here. Scenario A assumes a maximum penetration of the coseismic rupture into the STZ, Scenario B a linear transition of slip across the STZ, and Scenario C little penetration of the rupture into the STZ.

Figure C15. Schematic illustration of interseismic and coseismic deformation for various scenarios considered here. Note that the fault dislocation model for Scenario A will have an extremely narrow "spike" of uplift at the up dip tip of the fault, owing to elastic response of the model and the model assumption of a rupture terminating a few kilometers landward of the deformation front (Figure C14).

Figures C16-C18. Figures illustrate the vertical surface deformation from fault rupture Scenario 1 with three different slip distributions in the STZ (Figure C14; Table 1). The dark band of deformation on the right is subsidence; that on the left is uplift. The white band down the center is near zero deformation at the locus of the zero isobase. Note that the zero isobase is well offshore south of the Columbia River; compare to Figure C12.

Figures C19-C21. Figures illustrate the vertical surface deformation from fault rupture Scenario 2 with three different slip distributions in the STZ (Figure C14; Table 1). The dark band of deformation on the right is subsidence; that on the left is uplift. The white band down the center is near zero deformation at the locus of the zero isobase. Note that the zero isobase is close to shore south of the Columbia River and onshore south of Florence; compare to Figure C12.

Figures C22-C25. Vertical deformation for segmented fault ruptures on the Cascadia subduction zone (Table 2). The dark band of deformation on the right is subsidence; that on the left is uplift. The white band down the center is near zero deformation at the locus of the zero isobase. Note that the vertical deformation is about half that of the Scenario 1 and 2 ruptures (Figures C16-C21).

Figure C26. Cross section of vertical surface deformation from models with the STZ's of Figure C14 but all other parameters held constant. Note how the onshore deformation offers no constraints on vertical deformation in the STZ. Cross section trends east-west at the latitude of the Columbia River.

Figure C27. Cross section at the Columbia River of vertical surface deformation from models with constant STZ but variable width of the LZ and variable slip. Model 1C and 2Cn have the same STZ, LZ, and LTZ but Model 2Cn has about half the slip, leading to about half as much deformation. Model 1C has a narrower LZ and LTZ than Model 2C, leading to a seaward displacement of the subsidence trough. Note the better match of Model 2C to paleoseismic data for the 1700 AD event.

Figure C28. Cross section of vertical surface deformation showing the similarity of Models 1A and 2A at the latitude of Grays Harbor. Note the better fit of these models to the paleoseismic data relative to the segmentation model, Model 2Cn.

Figure C29. Cross section of vertical surface deformation showing the similarity of Models 1A and 2A at the latitude of Willapa Bay. Note the better fit of these models to the paleoseismic data relative to the segmentation model, Model 2Cn.

Figures C30-C38. Cross sections of vertical surface deformation showing the lateral offset of Scenarios 1 and 2, illustrated by Models 1A and 2A, at the latitude of estuaries with significant paleoseismic data. Note the better fit of Model 2A to the paleoseismic data, especially the pattern of increasing subsidence inland noted in Figure C12. Note also that Model 2A would fit the data somewhat better from the Columbia River to the Umpqua River, if the trough of subsidence were shifted eastward by about 13 km, so model subduction zone ruptures could be wider than 140 km in these areas.

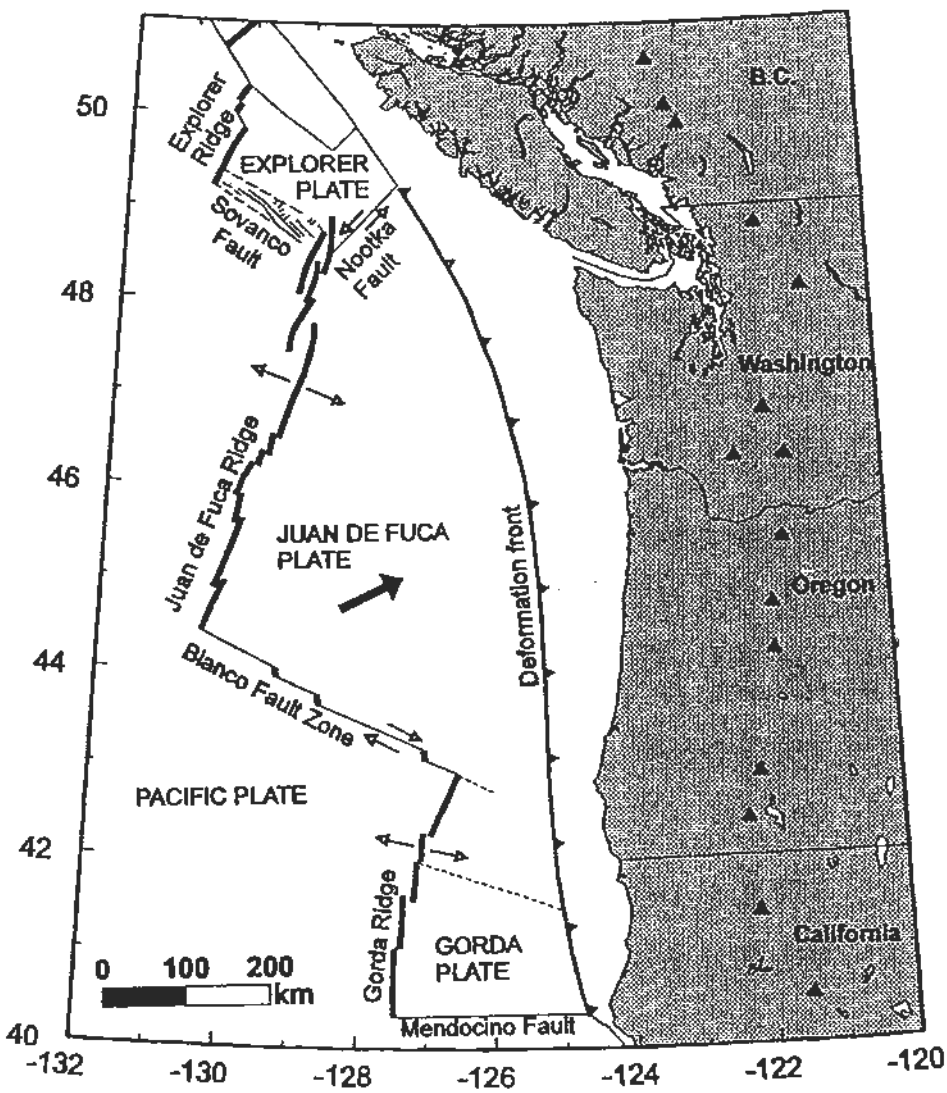

Figure C1. Plate tectonic map of the Cascadia subduction zone fault system illustrating the location of the surface trace of the fault at the deformation front. The subduction zone is bounded by the Nootka and Mendocino transform faults and dips 8-12° toward the east. Figure taken from Fleuck (1996).

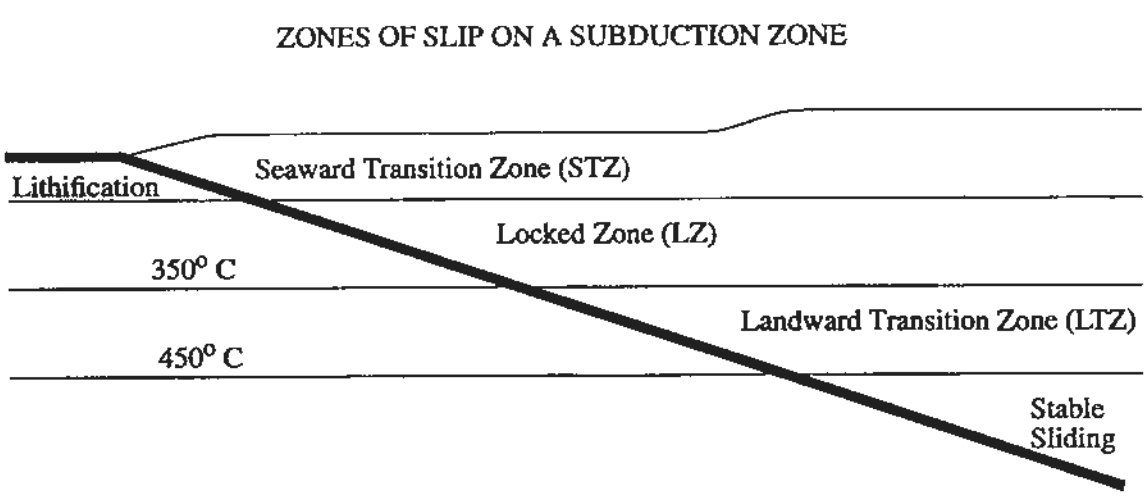

Figure C2. Schematic illustration of the zones of slip in a subduction zone. As water-saturated sediments at the deformation become progressively lithified, the fault behaves with more and more stick-slip behavior until it is fully locked at the base of the seaward transition zone (STZ). In the landward transition zone (LTZ), the fault movement changes from stick slip to stable sliding behavior as the temperature rises.

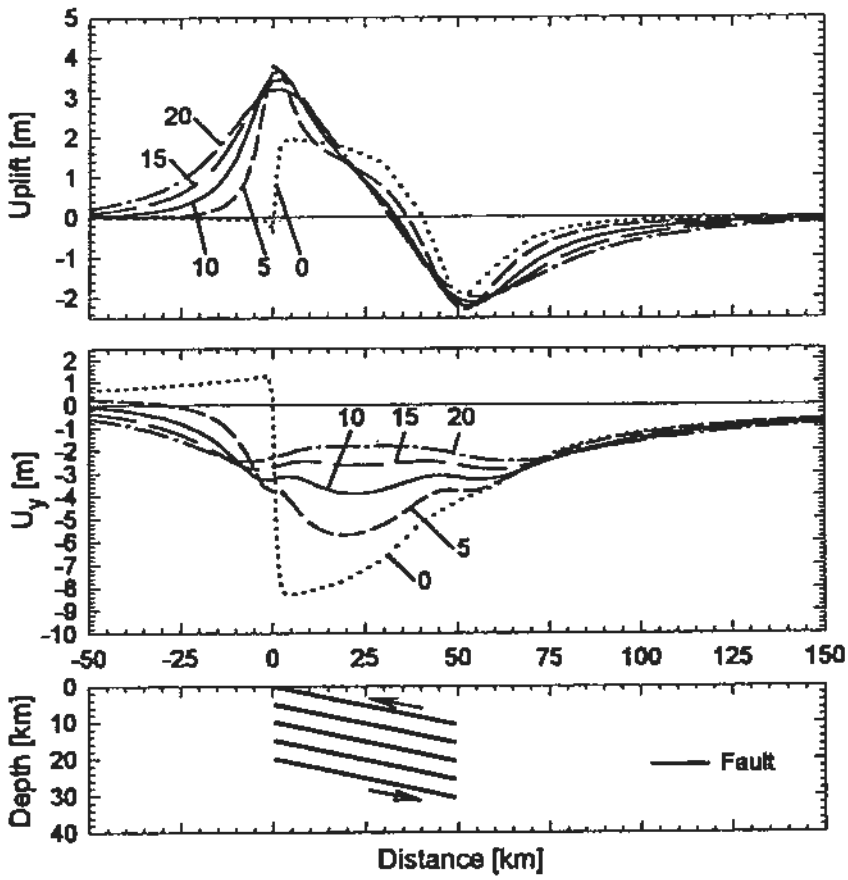

Figure C3. Sensitivity of surface deformation to burial of a rupture 1000 km long and 50 km wide with 10 m of pure dip slip thrust motion. Horizontal (U) and vertical deformation are illustrated. Note how deformation decreases with burial. The anomalous "spike" of uplift at the up dip end disappears, when the rupture reaches the surface (Figure taken from Fleuck, 1996; see text for explanation).

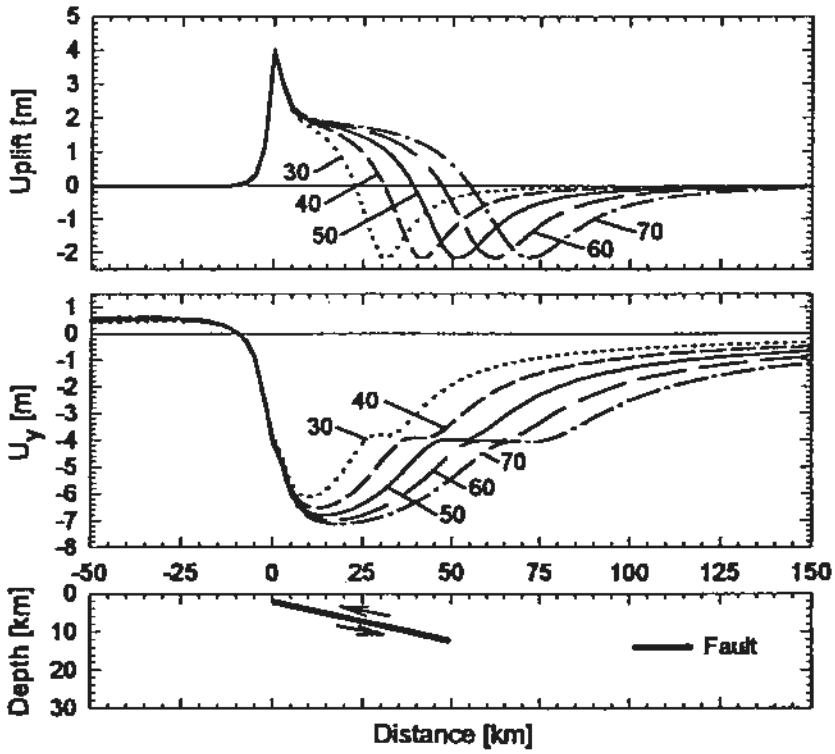

Figure C4. Sensitivity of surface deformation to rupture width on a fault 1000 km long with a slip of 10 m and dip of 12 degrees. Numbers are widths in kilometers. Note how the trough of subsidence migrates landward with increasing width but maintains the same depth.

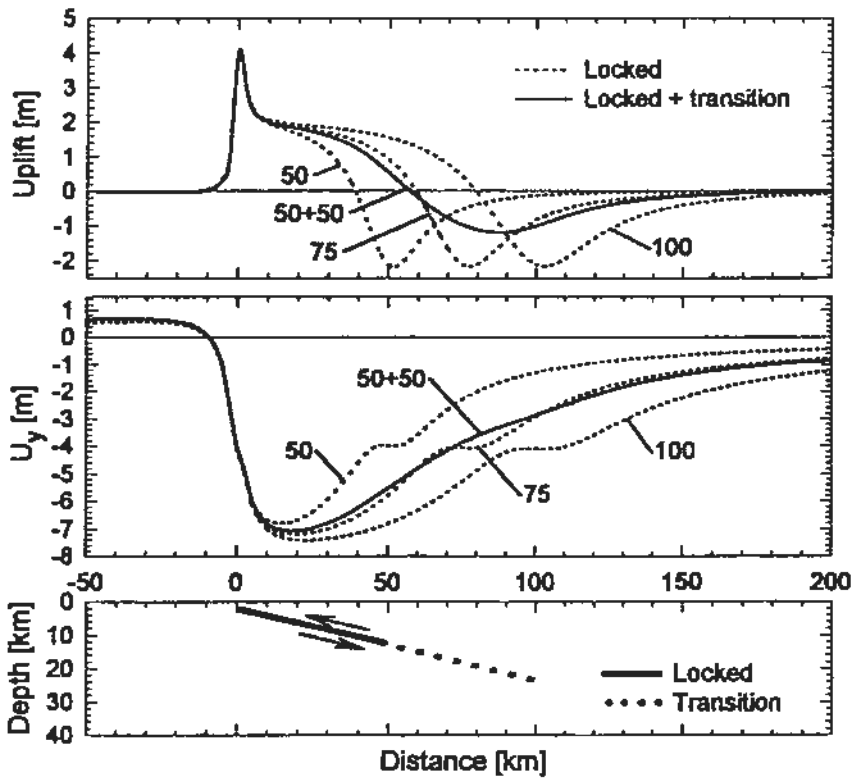

Figure C5. Sensitivity of surface deformation to addition of a landward (down dip) transition zone. The fault is 1000 km long with dip of 12 degrees and 10 m of pure dip slip thrust motion. The locked and transition zones are 50 km wide. Slip decreases linearly from 10 m to zero in the transition zone. Coseismic deformation from fully locked buried ruptures with widths of 50, 75, and 100 km are shown for comparison. Note how the same total slip in the 50 + 50 rupture produces about half as much subsidence as the fully locked 75 km rupture.

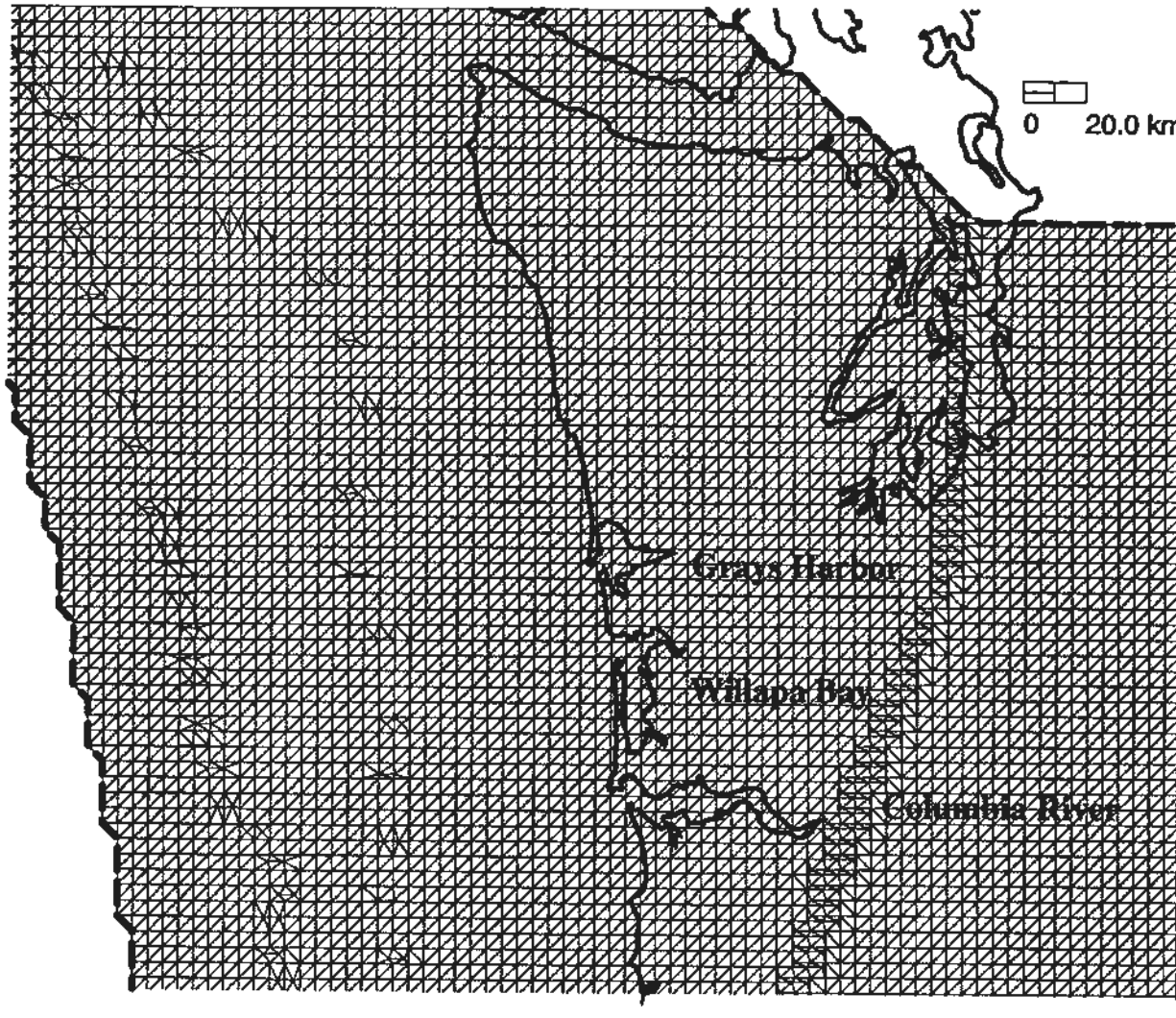

Figure C6. Numerical grid for the dislocation models.

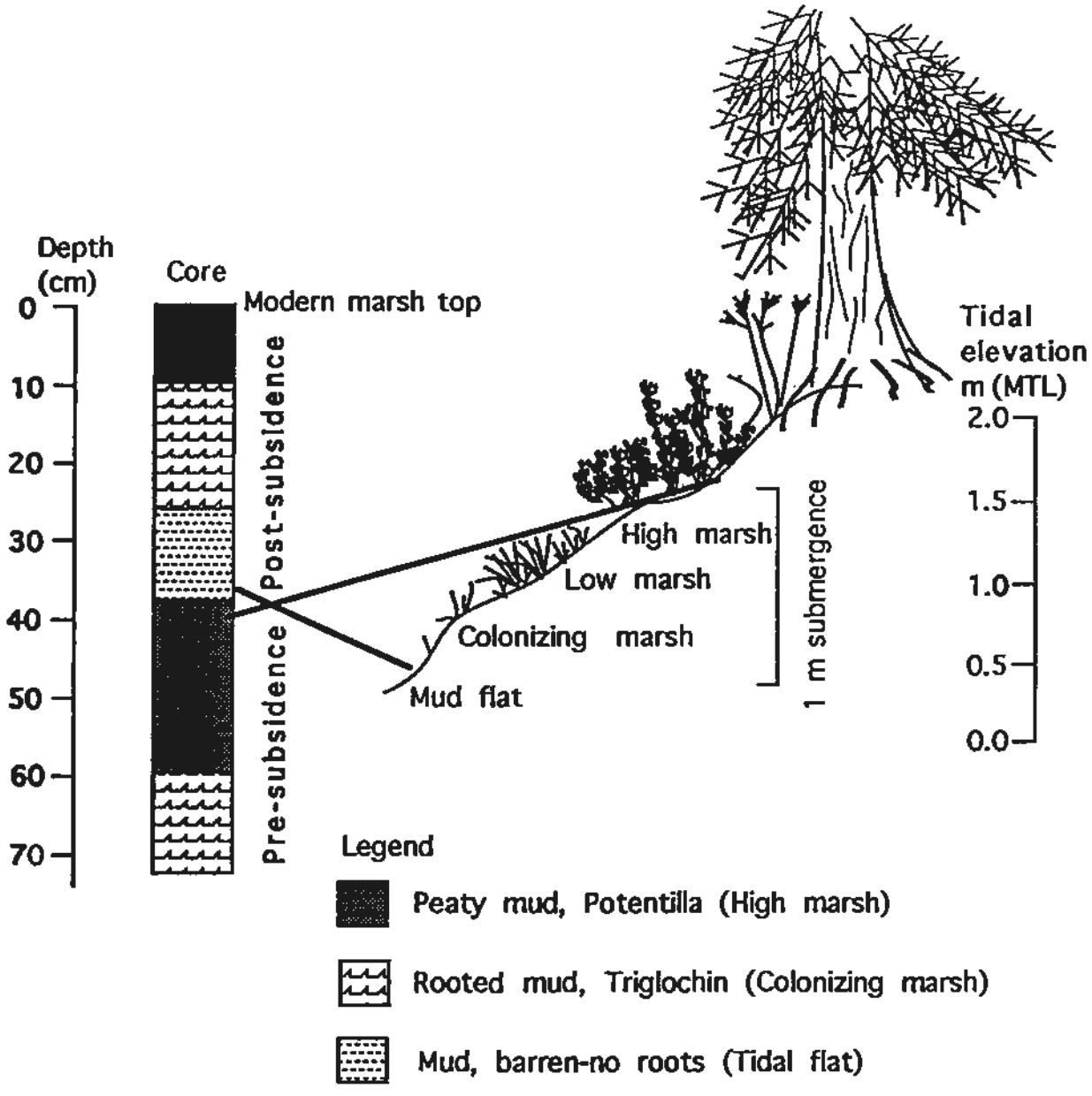

Figure C7. Typical vertical separation of ecological zones in coastal wetlands. Coseismic subsidence of various magnitudes will cause juxtaposition of these zones in vertical cores as shown, depending on what lateral position is sampled in the wetland. For example, a core taken in an area that is generally at a deep tidal channel will show only tidal channel sediments, unless coseismic uplift of unusual amount were to occur. On the other hand, a core taken in a lateral position generally occupied by the high marsh zone will record coseismic subsidence as buried peat layers in sharp contact with overlying intertidal mud or mud with colonizing marsh plants, depending on the degree of subsidence. Continuous sea level rise without coseismic subsidence would be recorded as continuous peat layers in this same high marsh setting.

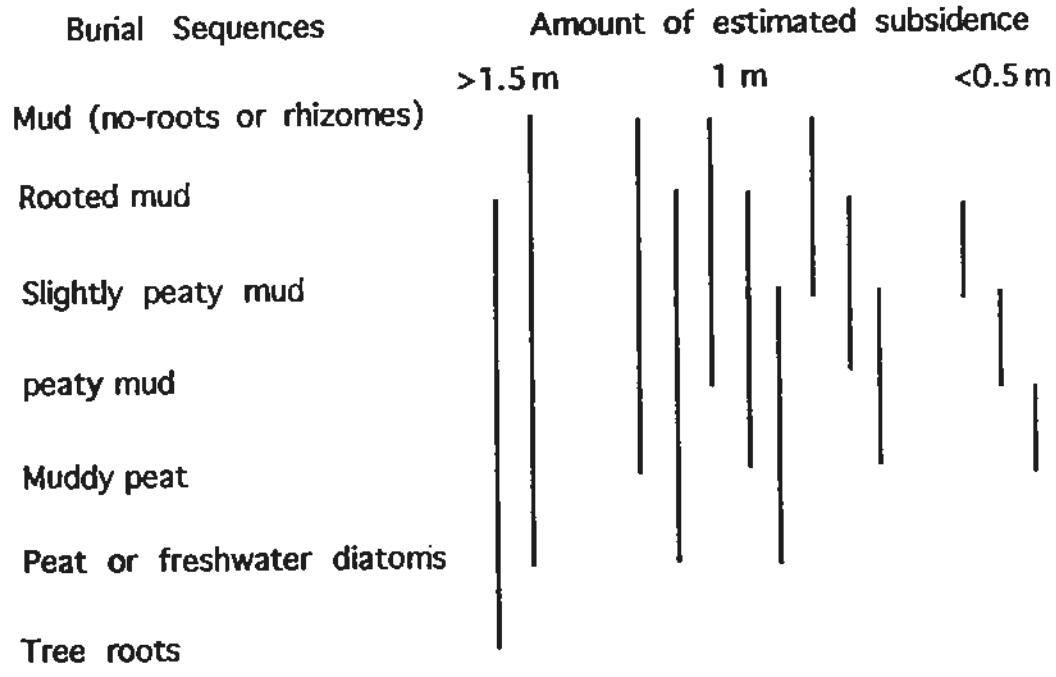

Figure C8. Diagram of fossil-lithologic categories of paleotidal level and corresponding amounts of paleosubsidence (0±0.5, 1±0.5, and 2±0.5 m) based on category transitions.

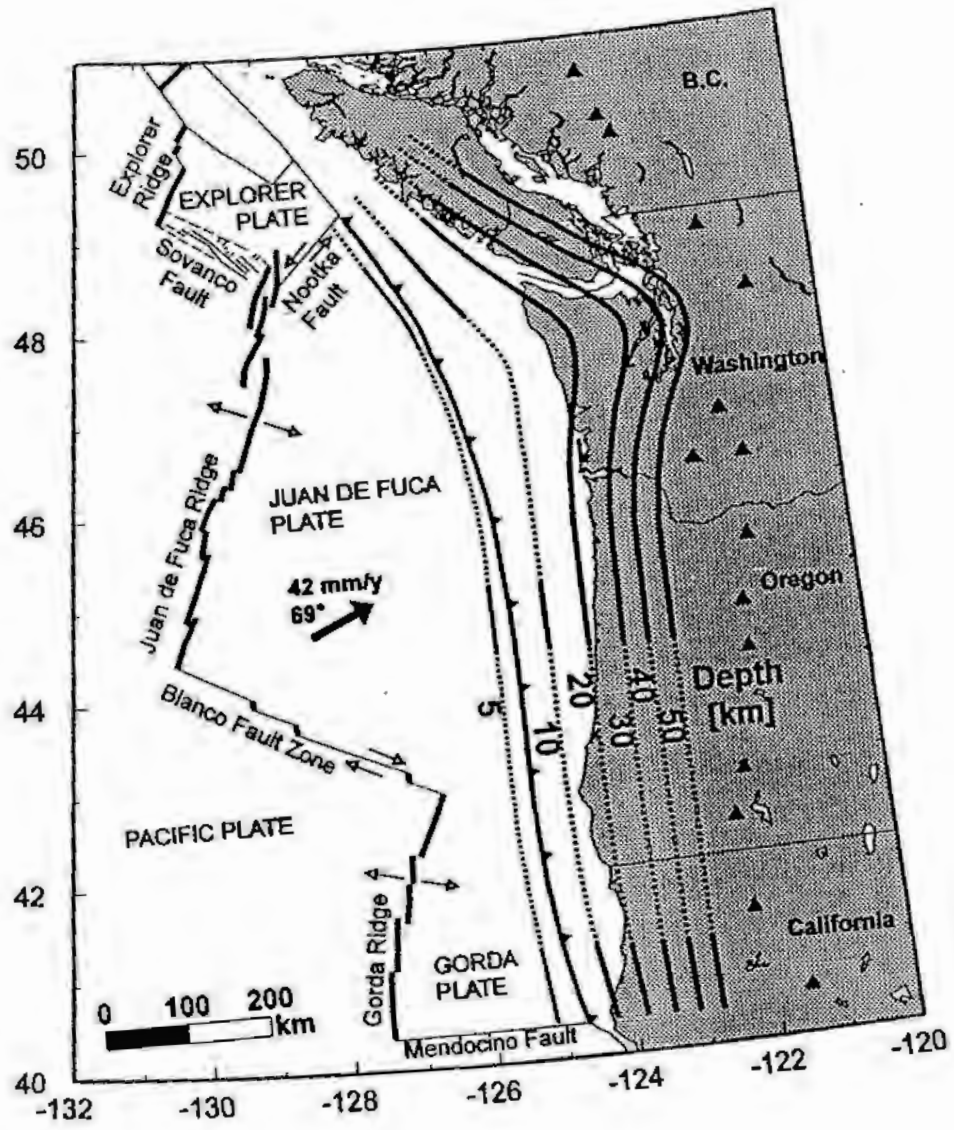

Figure C9. Strike and dip of the subduction zone. Structure contours are in kilometers referenced to sea level. Figure taken from Fleuck (1996).

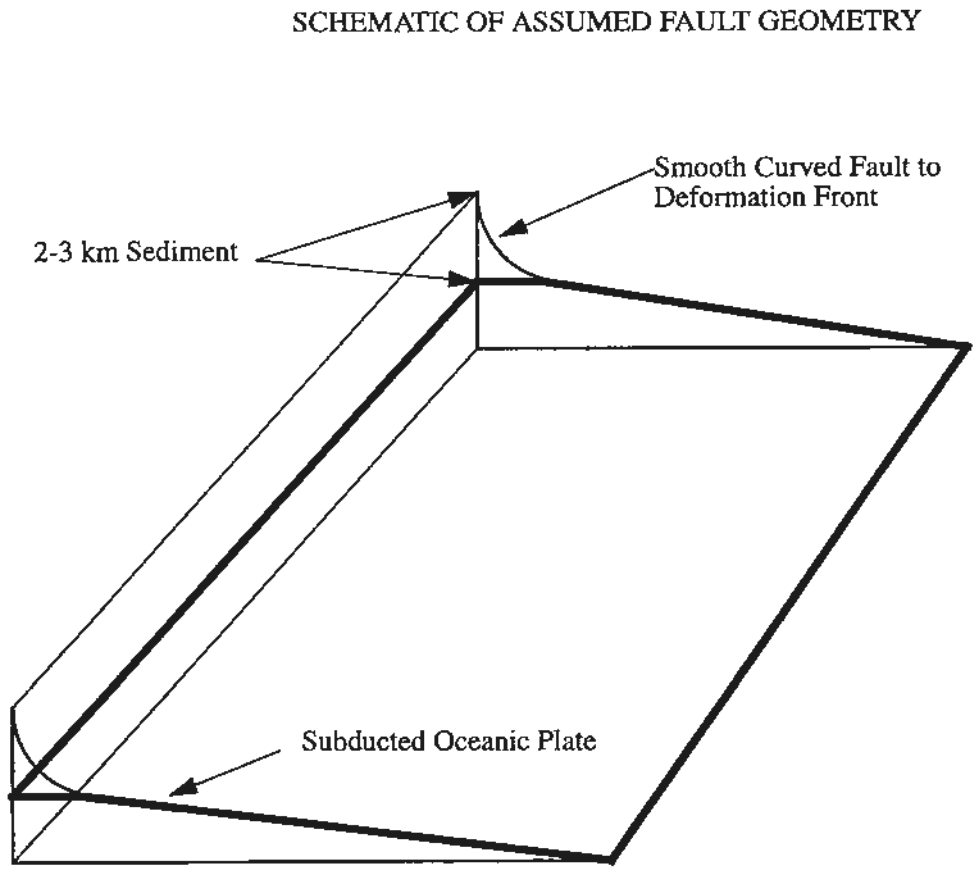

Figure C10. Schematic illustration of the way that the numerical model propagates the megathrust to the surface through the surficial sediments covering the oceanic plate at the deformation front.

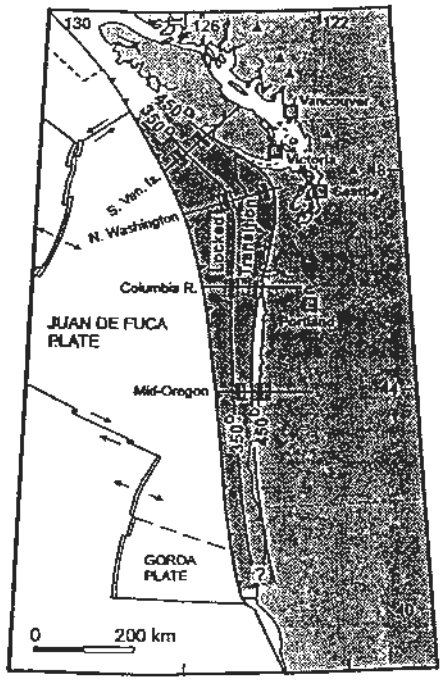

Fig. C11a

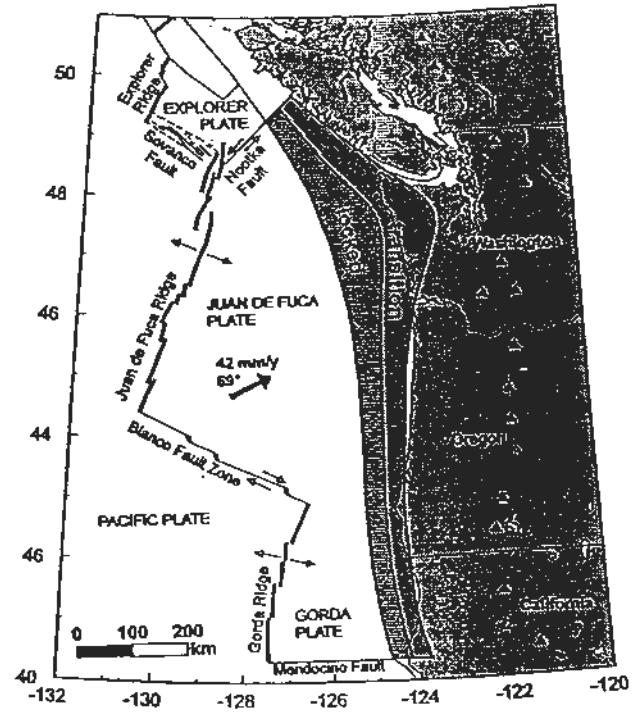

Fig. C11b

Figure C11a. Illustration of the uncertainty in the location of the isotherms governing width of the locked and landward transition zones. The two lines shown are the best fit by Hyndman and Wang (1995) to available thermal and geodetic data. Figure is from Hyndman and Wang (1995).

Figure C11b. Locked and landward transition zones of Fleuck and others (1996). This model is a best fit to available geophysical data and is very similar to the model in Figure C11a.

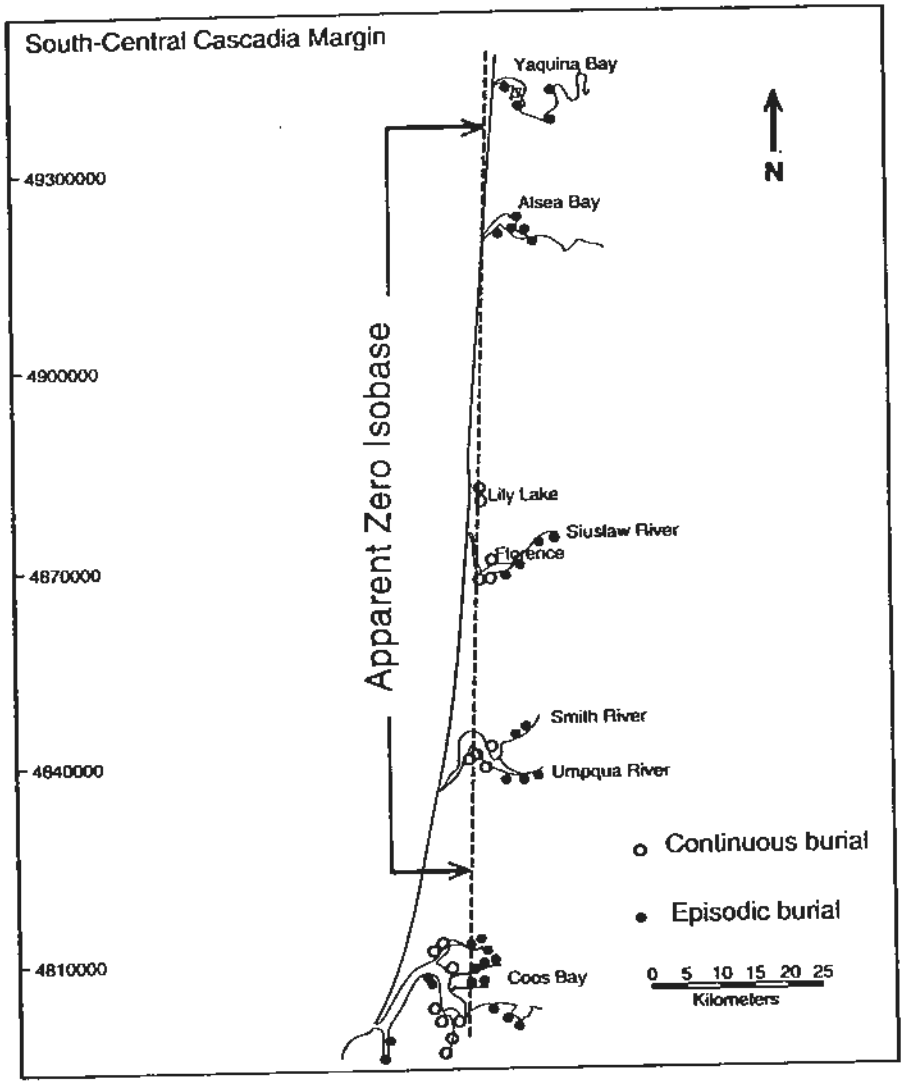

Figure C12. Pattern of paleosubsidence in south central Oregon from Briggs (1994). The open circles indicate areas with continuous peat development indicative of near zero paleosubsidence. Dots indicate core sites with abrupt vertical changes in peat development characteristic of episodic paleosubsidence. The pattern of increasing subsidence inland is opposite that predicted by the narrow ruptures illustrated in Figures C11a and C11b.

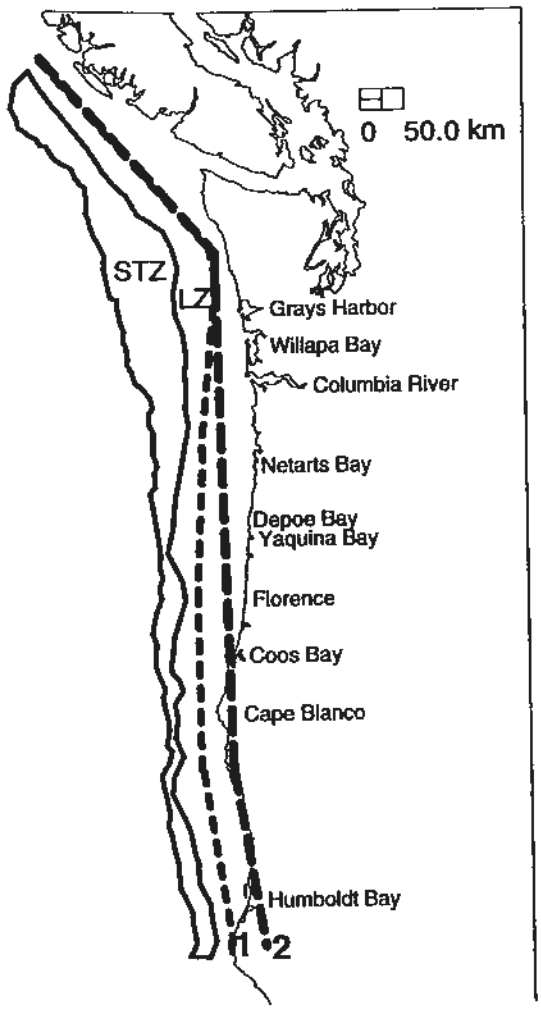

Figure C13. Maximum potential width of the seaward transition zone (STZ) and possible locations of the down dip end of the locked zone (LZ). Line 1 is the same as in Figure C11b. Line 2 is a possible location which matches patterns of coseismic subsidence inferred from paleoseismic data. Note how line 2 maintains a nearly constant distance from the deformation front (west side of the STZ).

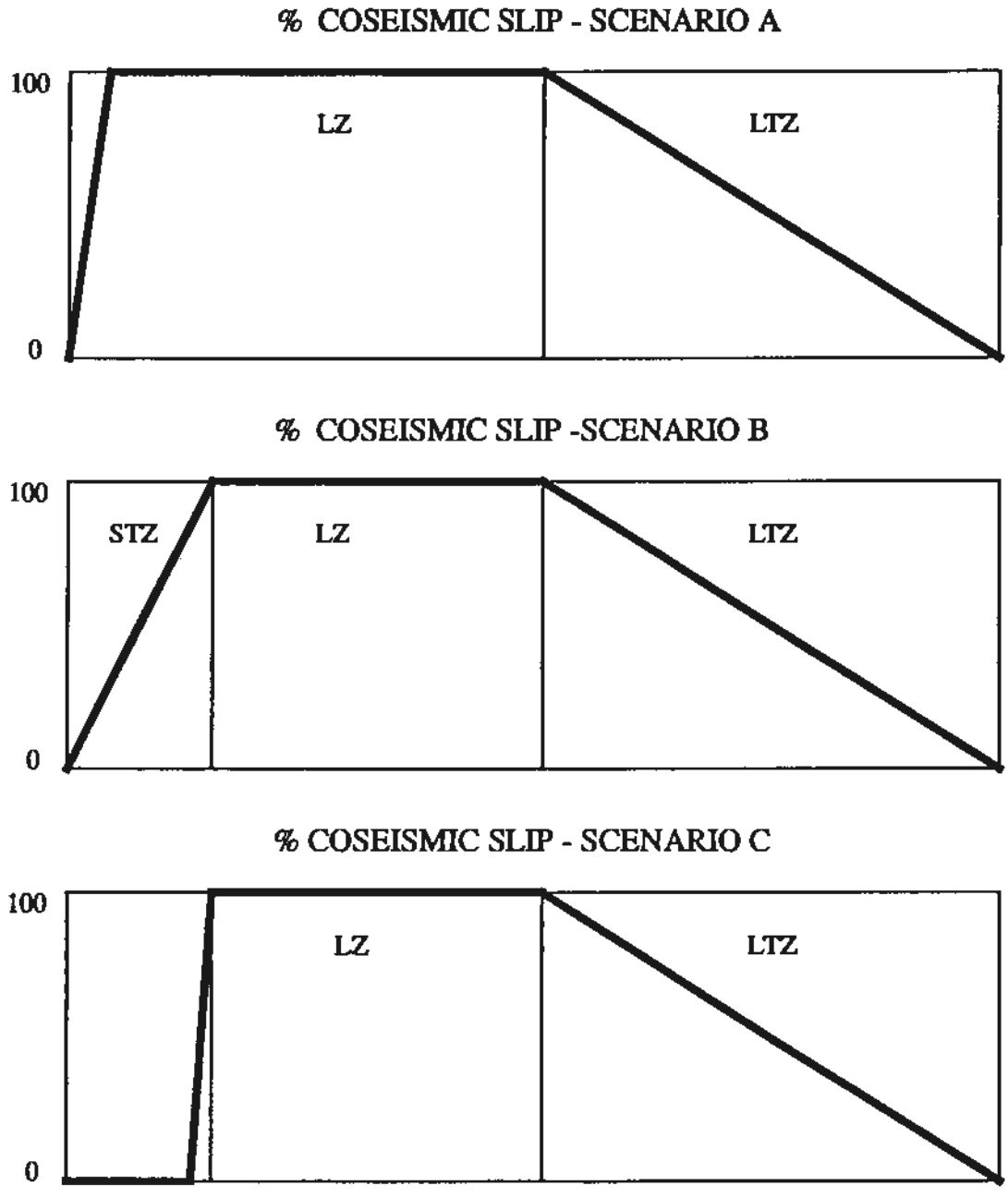

Figure C14. Schematic illustration of the coseismic slip distributions for STZ scenarios considered here. Scenario A assumes a maximum penetration of the coseismic rupture into the STZ, Scenario B a linear transition of slip across the STZ, and Scenario C little penetration of the rupture into the STZ.

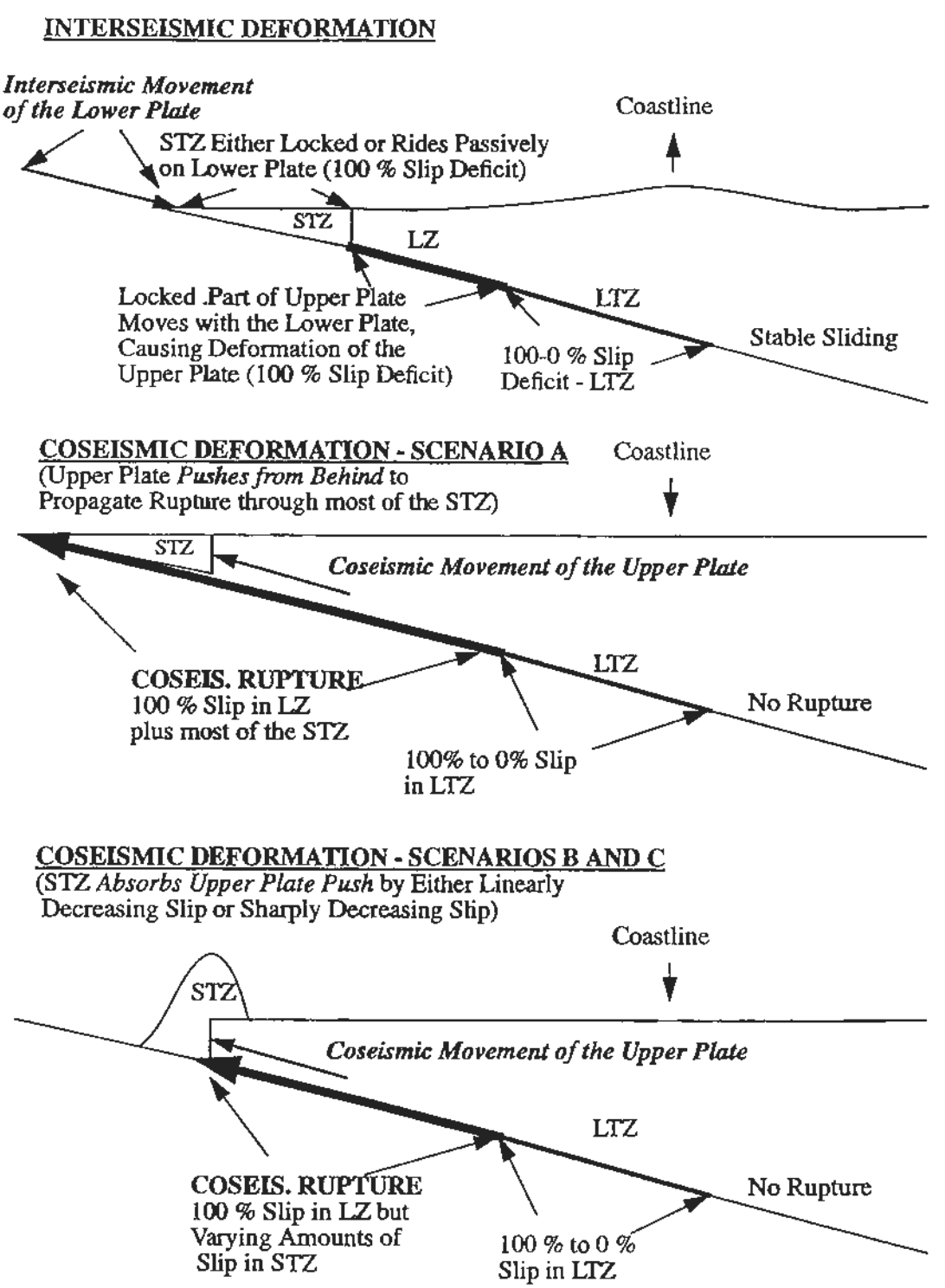

Figure C15. Schematic illustration of interseismic and coseismic deformation for various scenarios considered here. Note that the fault dislocation model for Scenario A will have an extremely narrow "spike" of uplift at the up dip tip of the fault, owing to elastic response of the model and the model assumption of a rupture terminating a few kilometers landward of the deformation front (Figure C14).

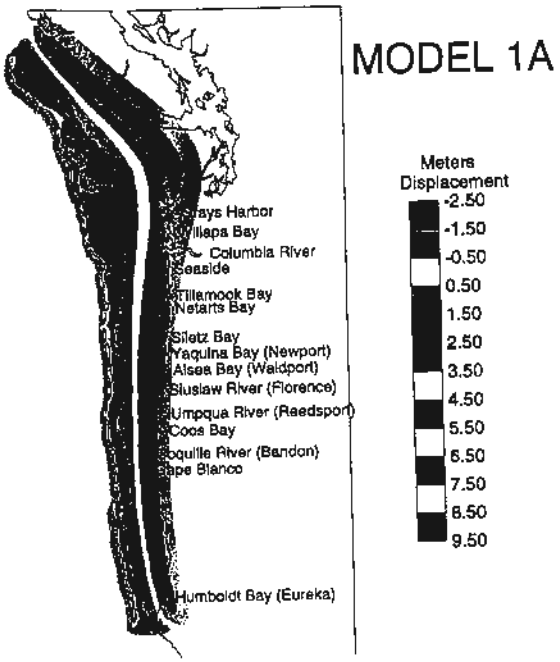

Fig. C16

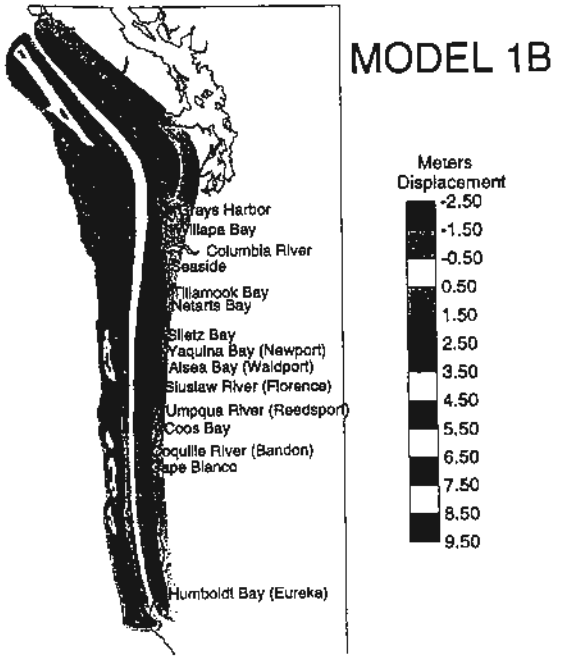

Fig. C17

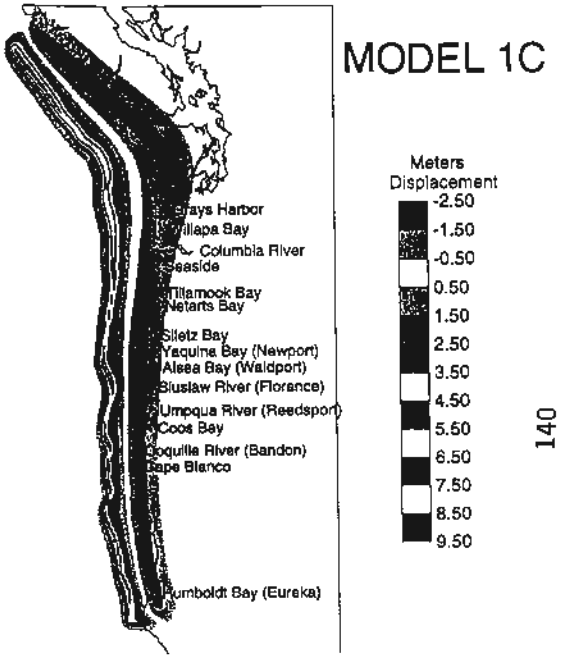

Fig. C18

Figures C16-C18. Figures illustrate the vertical surface deformation from fault rupture Scenario 1 with three different slip distributions in the STZ (Figure C14; Table 1). The dark band of deformation on the right is subsidence; that on the left is uplift. The white band down the center is near zero deformation at the locus of the zero isobase. Note that the zero isobase is well offshore south of the Columbia River; compare to Figure C12.

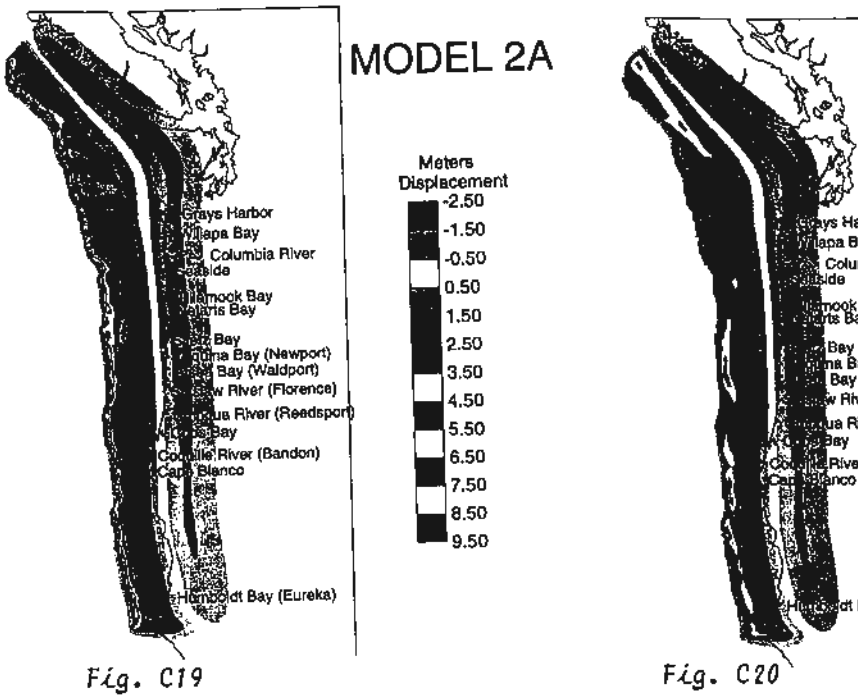

Fig. C19

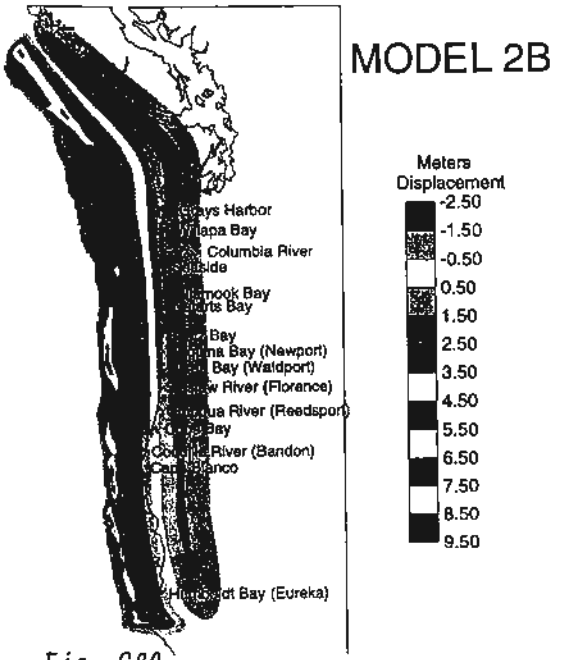

Fig. C20

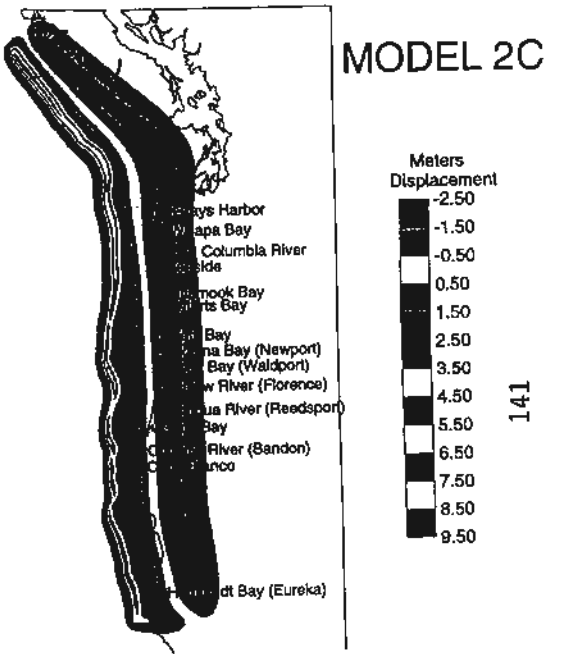

Fig. C21

Figures C19-C21. Figures illustrate the vertical surface deformation from fault rupture Scenario 2 with three different slip distributions in the STZ (Figure C14; Table 1). The dark band of deformation on the right is subsidence; that on the left is uplift. The white band down the center is near zero deformation at the locus of the zero isobase. Note that the zero isobase is close to shore south of the Columbia River and onshore south of Florence; compare to Figure C12.

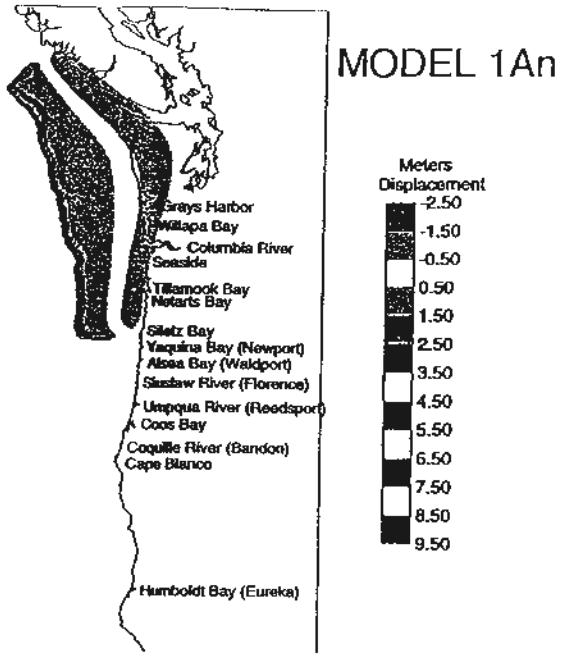

Fig. C22

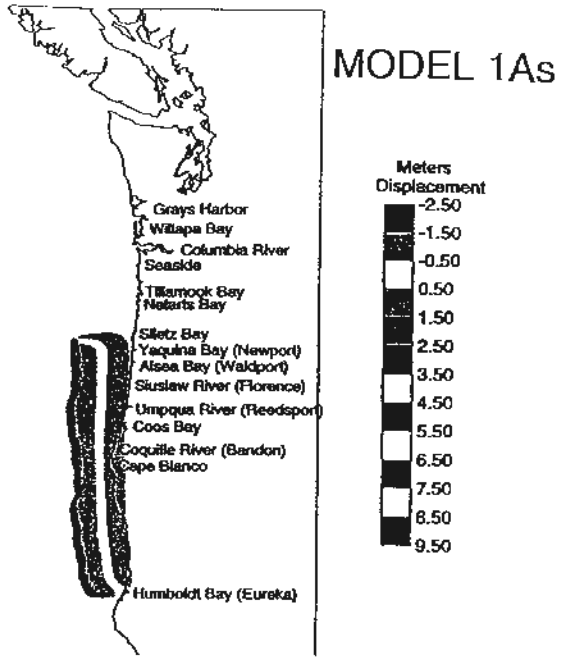

Fig. C23

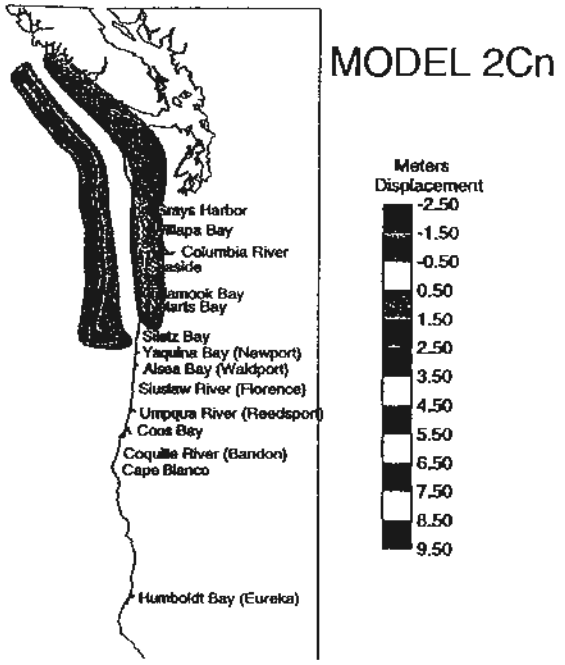

Fig. C24

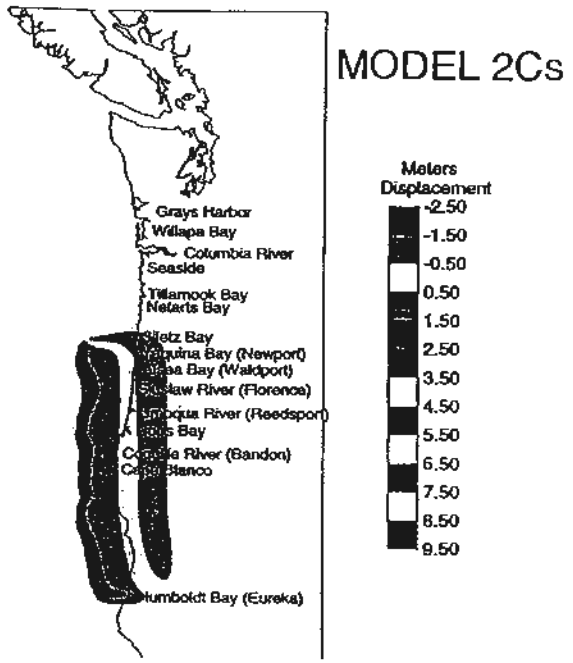

Fig. C25

Figures C22-C25. Vertical deformation for segmented fault ruptures on the Cascadia subduction zone (Table 2). The dark band of deformation on the right is subsidence; that on the left is uplift. The white band down the center is near zero deformation at the locus of the zero isobase. Note that the vertical deformation is about half that of the Scenario 1 and 2 ruptures (Figures C16-C21).

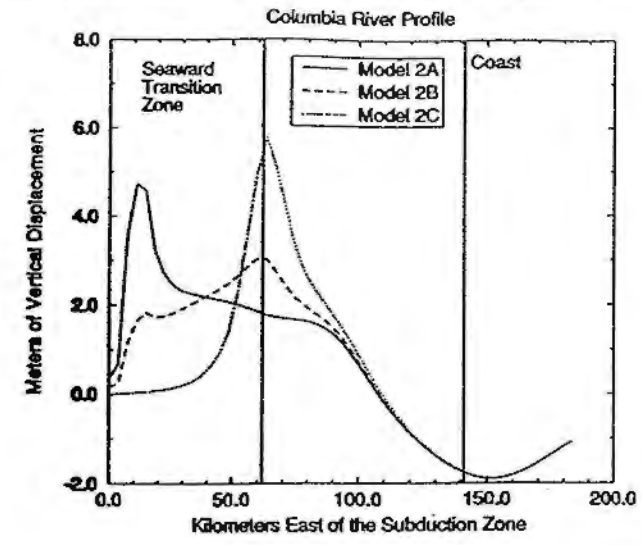

Fig. C26

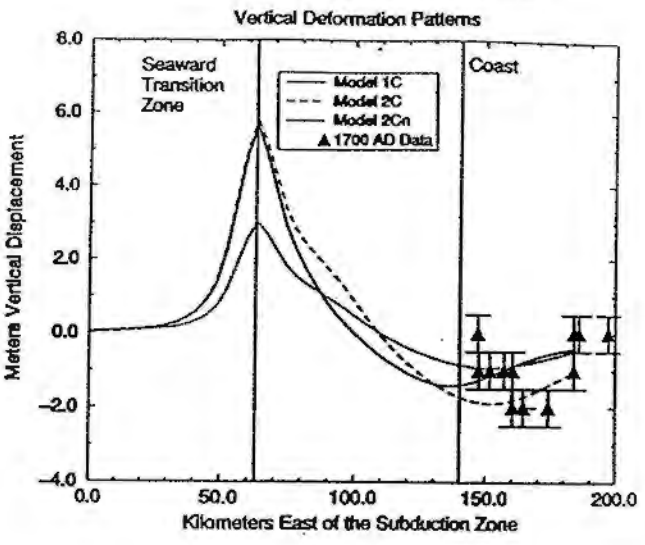

Fig. C27

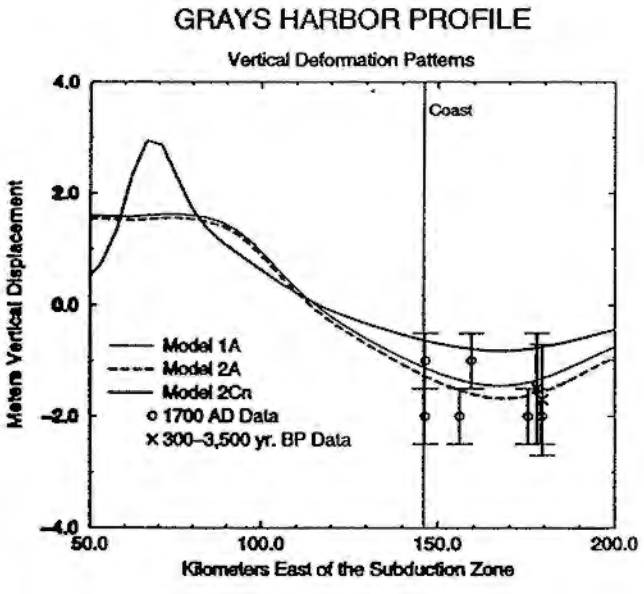

Fig. C28

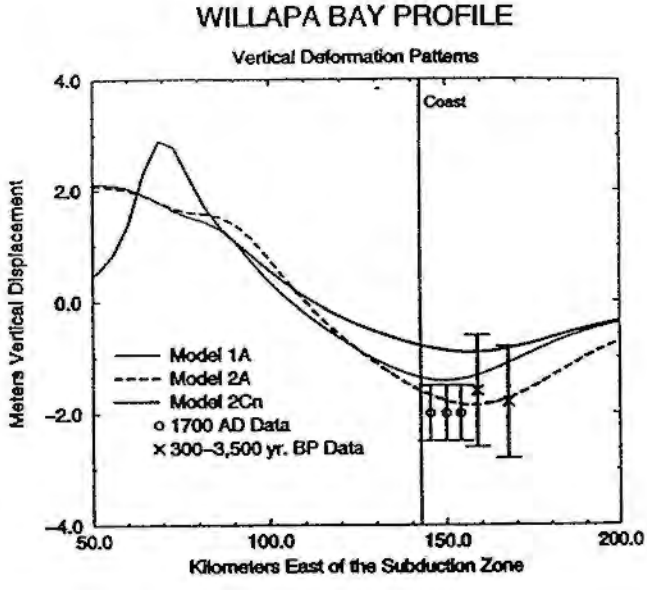

Fig. C29

Figure C26. Cross section of vertical surface deformation from models with the STZ's of Figure C14 but all other parameters held constant. Note how the onshore deformation offers no constraints on verticol deformation in the STZ. Cross section trends east-west at the latitude of the Columbia River.

Figure C27. Cross section at the Columbia River of vertical surface deformation from models with constant STZ but variable width of the LZ and variable slip. Model 1C and 2Cn have the same STZ, LZ, and LTZ but Model 2Cn has about half the slip, leading to about half as much deformation. Model 1C has a narrower LZ and LTZ than Model 2C, leading to a seaward displacement of the subsidence trough. Note the better match of Model 2C to paleoseismic data for the 1700 AD event.

Figure C28. Cross section of vertical surface deformation showing the similarity of Models 1A and 2A at the latitude of Grays Harbor. Note the better fit of these models to the paleoseismic data relative to the segmentation model, Model 2Cn.

Figure C29. Cross section of vertical surface deformation showing the similarity of Models 1A and 2A at the latitude of Willapa Bay. Note the better fit of these models to the paleoseismic data relative to the segmentation model, Model 2Cn.

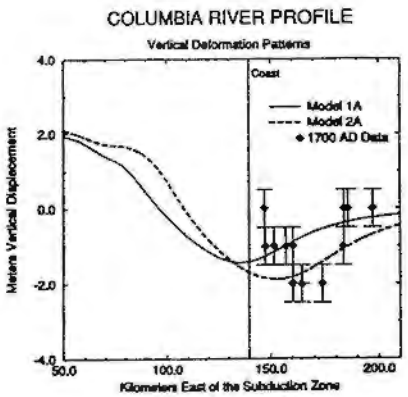

Fig. C30

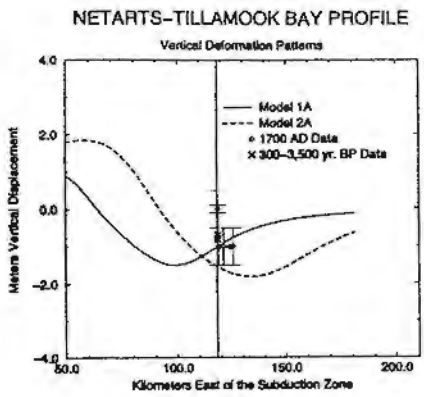

Fig. C31

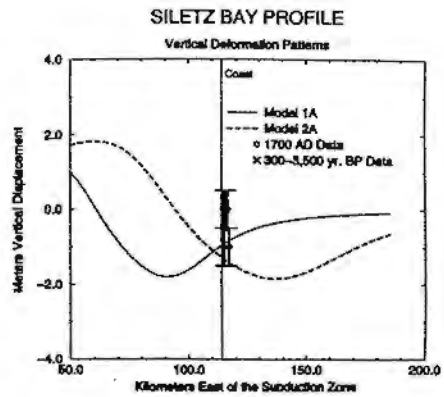

Fig. C32

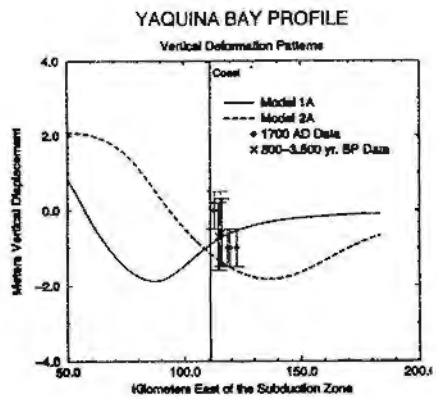

Fig. C33

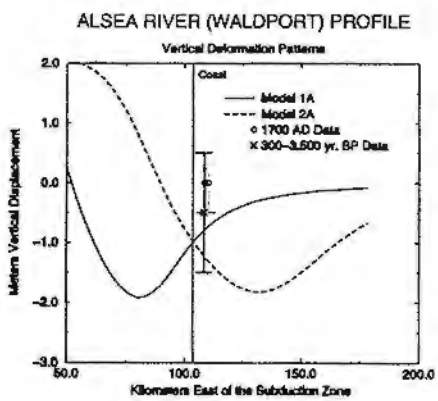

Fig. C34

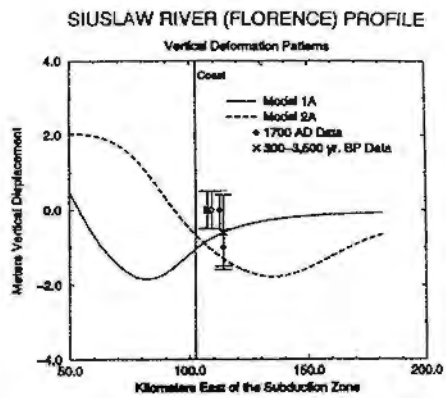

Fig. C35

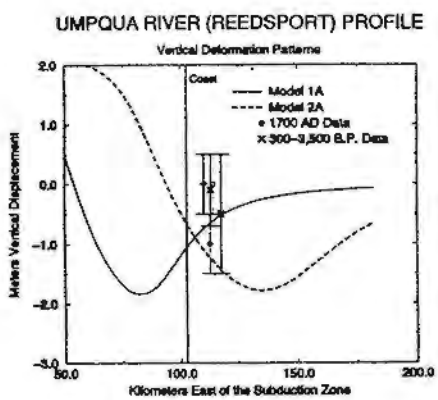

Fig. C36

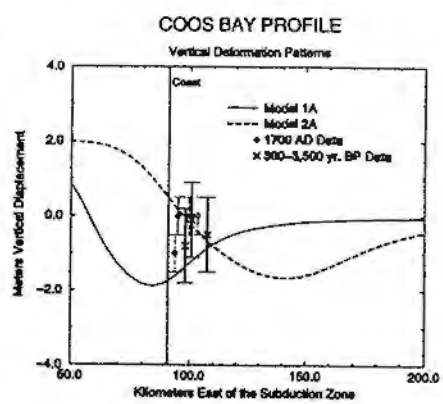

Fig. C37

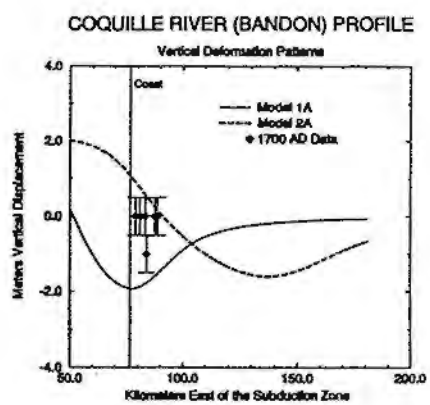

Fig. C38

Figures C30-C38. Cross sections of vertical surface deformation showing the lateral offset of Scenarios 1 and 2, illustrated by Models 1A and 2A, at the latitude of estuaries with significant paleoseismic data. Note the better fit of Model 2A to the paleoseismic data, especially the pattern of increasing subsidence inland noted in Figure C12. Note also that Model 2A would fit the data somewhat better from the Columbia River to the Umpqua River, if the trough of subsidence were shifted eastward by about 13 km, so model subduction zone ruptures could be wider than 140 km in these areas.